

Physics, MOVPE growth, and investigation of *m*-plane GaN films and InGaN/GaN quantum wells on γ -LiAlO₂ substrates

Von der Fakultät für Elektrotechnik und Informationstechnik
der Rheinisch-Westfälischen Technischen Hochschule Aachen
zur Erlangung des akademischen Grades eines Doktors
der Ingenieurwissenschaften genehmigte Dissertation

vorgelegt von

Diplom-Ingenieur

Christof Mauder

aus Würzburg

Berichter: apl. Prof. Dr.-Ing. M. Heuken

Univ.-Prof. Dr. rer. nat. W. Mokwa

Tag der mündlichen Prüfung: 20.12.2011

Diese Dissertation ist auf den Internetseiten der Hochschulbibliothek online verfügbar.

Contents

1	Introduction	4
2	Basic properties of group III nitride semiconductors	8
2.1	Material properties and crystal structure	8
2.2	Polarization effects in group III nitrides	10
2.2.1	Strain and stress in the group III nitride system	10
2.2.2	Polarization in nitride-based heterostructures	12
3	Theoretical aspects in nonpolar GaN epitaxy	17
3.1	Anisotropy of crystal and defect structure	17
3.1.1	Anisotropic strain and defects	17
3.1.2	Crystal growth anisotropy	22
3.2	Effect of crystal anisotropy on electronic band structure	22
4	Substrates for nonpolar GaN epitaxy	26
4.1	Free-standing nonpolar GaN substrates	26
4.2	Foreign substrate materials for nonpolar GaN epitaxy	27
4.3	Properties of (100) γ -lithium aluminium oxide (LiAlO ₂)	30
5	Tools and methods for epitaxy and characterization	34
6	Study on pretreatment of the LiAlO₂ surface and its effect on GaN epitaxy	38
6.1	Stability of LiAlO ₂ in MOVPE growth environment	38
6.2	Study of nitridation-induced surface modification	40
6.3	Impact of nitridation on subsequent GaN epitaxy	45
7	Anisotropic crystal properties of <i>m</i>-plane GaN films on LiAlO₂	49
7.1	Three-step growth technique for thick GaN film deposition	49
7.2	Surface features of <i>m</i> -plane GaN films on LiAlO ₂	51
7.2.1	Morphology of optimized GaN films	51
7.2.2	Effect of V/III ratio on surface morphology	54

7.3	Structural properties of <i>m</i> -plane GaN films on LiAlO ₂	55
7.3.1	Defect and strain characterization by XRD.....	55
7.3.2	TEM investigation of crystal microstructure.....	61
7.3.3	Defects revealed by Electron Channelling Contrast Imaging (ECCI)	64
7.4	Optical properties of <i>m</i> -plane GaN films on LiAlO ₂	65
7.4.1	Polarization-resolved luminescence characteristics	66
7.4.2	Study of high-excitation luminescence and free carrier dynamics.....	69
7.5	Doping and electrical characterization of <i>m</i> -plane GaN on LiAlO ₂	73
8	Impurities in <i>m</i>-plane GaN films on LiAlO₂.....	76
8.1	Identification and quantification of impurity atoms.....	76
8.2	Mechanisms of impurity incorporation during MOVPE of <i>m</i> -plane GaN on LiAlO ₂	78
9	Growth and characterization of <i>m</i>-plane InGaN/GaN multiple quantum well heterostructures	83
9.1	Morphological and structural properties of <i>m</i> -plane InGaN/GaN quantum well structures.....	83
9.2	Optical characterization of InGaN/GaN MQW on LiAlO ₂	90
9.2.1	RT photoluminescence characteristics	90
9.2.2	Temperature-resolved photoluminescence.....	93
9.2.3	Determination of polarized emission and absorption behaviour.....	95
9.3	Demonstration of <i>m</i> -plane InGaN/GaN-based LED	98
10	Summary and conclusion.....	105
	List of figures.....	109
	List of tables	113
	List of abbreviations.....	114
	References.....	118
	Acknowledgements	128
	List of publications	130
	Curriculum vitae.....	133

1 Introduction

The first observation of current-induced light emission from SiC by H. J. Round in 1907 and the explanation of this effect more than fifty years later have been the basis for a steadily increasing and still ongoing research effort on light emitting diodes (LED) [1]. The main drive for the development of these novel light sources is the prospect of replacing established light bulbs by emitters with higher efficiency. In addition to that, their unique compactness and good colour control has also inspired people to use LED as tailor-made light source for applications in for instance traffic, entertainment, biological sensing and medicine. Due to their mostly direct bandgaps, compound semiconductors are the materials of choice for efficient light emitters. The early work on gallium arsenide (GaAs), silicon carbide (SiC), the group II-VI semiconductors, and gallium phosphide (GaP) was followed by the advent of the nitrides, first established by the pioneering research of Akasaki and Nakamura in 1989 and 1991, respectively [2, 3]. Gallium nitride (GaN) as a wide-bandgap semiconductor and its ternary alloys with indium (InGaN) and aluminium (AlGaN) opened up the way for the design of efficient light sources in the green, blue and ultraviolet (UV) spectral range. Figure 1.1 illustrates the bandgap of group III nitrides and their ternary alloys and gives a correlation to the wavelength spectrum in the visible range. It is interesting to note that GaN films, which are typically grown on foreign substrates as sapphire (Al_2O_3), silicon (Si) or SiC, exhibit giant densities of threading dislocations (TD) ranging from 10^8 cm^{-2} to 10^{12} cm^{-2} [4]. Although dislocations have a negative impact on GaN-based light-emitting devices, their sensitivity to such high levels of defect densities is, unlike for other III-V compounds, much lower [5, 6]. This reason is the crucial benefit of group III nitrides in optoelectronic devices compared to other semiconductor families. After years of intense worldwide research, InGaN-based LED and also LASER diodes (LD) nowadays have reached a considerable level of maturity. As one example, phosphor-aided white LED with luminous efficacy values of up to 230 lm/W at 350 mA driving current have recently been reported [7]. Another tremendous achievement is the demonstration of

continuous-wave green LD with 50 mW maximum output power operating at a wavelength of 524 nm [8].

However, there are many challenges remaining, especially when it comes to applications requiring high brightness or perfect colour stability. Both issues are related to intrinsic crystal properties of the nitrides itself, namely the built-in spontaneous and piezoelectric polarization fields [9, 10]. These fields are active in the c -axis direction of the GaN crystal, which is also the common growth orientation. As a consequence, embedded quantum wells (QW) are also subject to this electric field, which hampers both recombination efficiency and wavelength stability with driving current [11]. Moreover, a reduction of quantum efficiency at high output powers is always observed for InGaN-based LED [12]. The origin of this so-called “droop”-phenomenon is yet under discussion, but credible reports state that polarization fields within the multiple quantum well (MQW) stack are at least partly responsible for the effect [13].

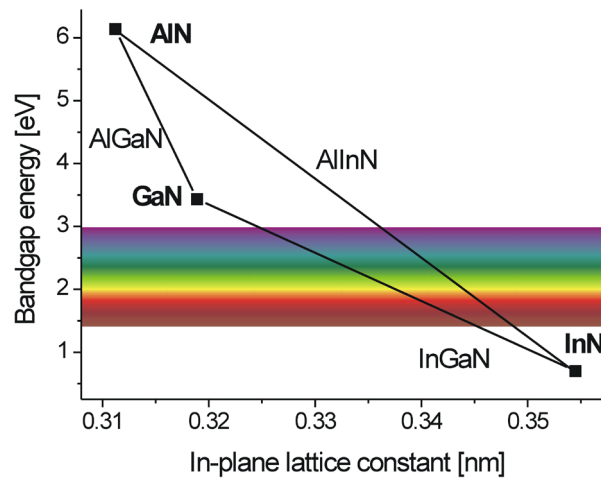


Figure 1.1: Bandgap energy versus in-plane lattice constant for AlN, GaN and InN and their ternary alloys (no bowing assumed). The energy range of the visible spectrum is schematically depicted.

Thus, it is obvious that by eliminating the negative effects of polarization, a great improvement or even the development of new device concepts of nitride-based light

emitters can be expected. A very promising way to reach this is to change the growth orientation of the GaN crystal from the polar (0001) c -plane to a nonpolar plane as the $(1\bar{1}00)$ m -plane or $(11\bar{2}0)$ a -plane. In this way, the electric fields are oriented perpendicular to the growth direction and thus cannot affect vertical carrier transport and recombination in QW and barriers of LED devices. Waltereit et al. were the first to demonstrate the successful growth of GaN in the nonpolar m -plane orientation [14]. As a prerequisite for achieving nonpolar growth, one has to provide a suitable substrate with good lattice matching to the nonpolar crystal plane. Among the various alternatives for m -plane GaN deposition, a very interesting one is LiAlO_2 since it features a low substrate-lattice mismatch and can be produced with large size at reasonable effort and cost [15, 16]. Both molecular beam epitaxy (MBE) [17] and metal organic vapour phase epitaxy (MOVPE) [18] have been used to demonstrate the growth of m -plane GaN films on this substrate. The subsequent deposition of InGaN-based QW heterostructures showed clear evidence for the absence of out-of-plane polarization fields [19, 20]. However, a systematic study on the growth of GaN-based heterostructures on LiAlO_2 taking into account the formation of strain and defects and their impact on morphology, optical and electrical properties was not presented so far and is the topic of this work.

As mentioned before, the elimination of polarization-induced effects is the goal for improving the quantum efficiency of devices. Chapter 2 will therefore give a basic introduction into the origin and effects of polarization in group III nitrides. To this end, some information about the wurtzite crystal structure is also provided. Because of the reduced symmetry of the m -plane GaN crystal structure, new anisotropic effects can be observed. Chapter 3 will briefly explain the underlying physics related to the anisotropy. For the heteroepitaxy of thin films, the substrate material affects virtually all physical properties of the deposited layer. Thus, a good knowledge of its crystal properties is required. In this study, LiAlO_2 is used for the deposition of m -plane GaN films by MOVPE. The most important characteristics of this substrate as well as its advantages and disadvantages for the growth of m -plane GaN are presented in chapter 4. For comparison, other possible substrate materials for nonpolar GaN epitaxy like m -plane SiC, r -plane sapphire or nowadays available m -plane GaN bulk crystals are also described. After reviewing experimental details on the epitaxy and characterization techniques used in this work in section 5, some experimental results

on the thermal and chemical stability of the LiAlO_2 substrates are discussed in chapter 6. It is presented how a substrate pretreatment can reduce the substrate sensitivity and improve the growth of GaN. A detailed investigation of the anisotropic morphology, defect structure, strain, electrical and optical properties of *m*-plane GaN layers is described in chapter 7. This is followed by section 8, which deals with the problem of undesired background doping in *m*-plane GaN. In chapter 9, the growth and characterization of InGaN/GaN MQW is addressed, including the demonstration of an *m*-plane InGaN/GaN-based LED on LiAlO_2 . The final chapter 10 summarizes this work.

2 Basic properties of group III nitride semiconductors

This chapter provides some basic information on crystallographic structure and material parameters of the group III nitrides, followed by a description of the spontaneous and piezoelectric polarization fields and their effects on QW heterostructures.

2.1 Material properties and crystal structure

Group III nitride semiconductors exhibit unique properties which distinguish them from other classical semiconductor types as Si and GaAs. Their characteristics include good thermal, mechanical, and chemical stability, which are mostly related to the strong bonding between the metal and nitrogen (N) atom. Some selected material parameters at room temperature (RT) are given in Table 2.1.

Table 2.1: Selected group III nitride material parameters at $T = 300$ K.

	Unit	Ref.	GaN	AlN	InN
Lattice parameter a / c	nm	[21]	0.3189 / 0.5185	0.3112 / 0.4982	0.3545 / 0.5703
Density ρ	g/cm ³	[22]	6.07	3.29	6.81
Melting point	K	[22]	2791	3487	2146
Bandgap energy E_g	eV	[21]	3.44	6.14	0.7
Thermal expansion coefficient $\alpha (a / c)$	K ⁻¹	[23, 24]	$3.43 \cdot 10^{-6} /$ $3.34 \cdot 10^{-6}$	$4.35 \cdot 10^{-6} /$ $3.48 \cdot 10^{-6}$	$3.83 \cdot 10^{-6} /$ $2.75 \cdot 10^{-6}$
Spontaneous polarization P_{sp}	C/m ²	[25]	-0.034	-0.090	-0.042

The values are valid for the thermodynamically stable crystal structure of group III nitrides, which is the wurtzite phase. Two lattice parameters, namely the in-plane lattice parameter a and the out-of-plane parameter c are used to describe this hexagonal crystal. The group III nitrides are compound semiconductors and can be described by two hexagonal close-packed sub-lattices for both metal and N atoms, which are shifted by each other in c -direction by $5/8$ unit cell lengths c . In Figure 2.1 a), a schematic drawing of the crystal structure of GaN is exemplarily given.

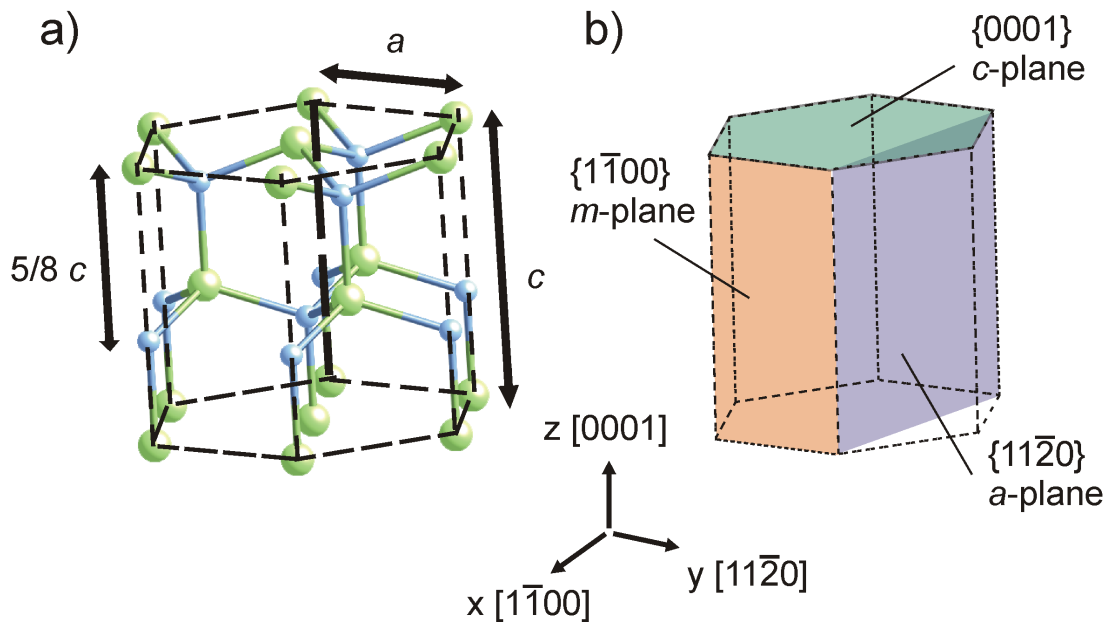


Figure 2.1: Crystal structure of GaN in a ball-and-stick model. Ga and N atoms are displayed as big green and small blue spheres, respectively.

One can easily see that the crystal structure does not exhibit any inversion symmetry. Thus, two essentially different orientations can be assigned. The $[0001]$ direction is commonly defined as the orientation in which the unit cell is terminated by gallium (Ga) atoms. This direction (exhibiting the Ga-face) is also the typically used orientation for group III nitride epitaxy since it is readily achieved for the nucleation of GaN and AlN on sapphire and Si substrates using standard MOVPE growth conditions. In the hexagonal system, three different important planes are distinguished and visualized in Figure 2.1 b). The family of basal planes are known as $\{0001\}$ c -plane, while the prismatic planes are denoted as $\{1\bar{1}00\}$ m -plane. Another kind of plane, which is

perpendicular to both the m -plane and the c -plane, is sometimes described as 2nd order prismatic plane and labelled as $\{11\bar{2}0\}$ a -plane. This work focuses on the epitaxy of m -plane-oriented films. Both the m -plane and the a -plane take a special role because each of them contains an equal number of Ga and N atoms. As a result, layers and heterostructures grown with this orientation do not suffer from the effects of the inbuilt polarization fields. The next section gives a short introduction into the issue of polarization fields and shows their effect on the properties of heterostructures.

2.2 Polarization effects in group III nitrides

The different electronegativities of the metal and N atoms in the group III nitrides and a lack of inversion symmetry in the crystal structure causes a displacement of charges along the c -axis, which is the principal origin of spontaneous and piezoelectric polarization for group III nitrides. While spontaneous polarization is an inherent property of the material itself and only depends on the polarity and composition of the crystal, the piezoelectric polarization is related to both polarity, composition, and applied stress. Since during heteroepitaxy of mismatched material systems, stress is naturally present, the total polarization in group III nitrides is the sum of the spontaneous and piezoelectric component. To estimate the quantity of the polarization fields, one has to consider the stress and strain in the layers first.

2.2.1 Strain and stress in the group III nitride system

In solid state physics, the term strain denotes the dilation or shrinking of a crystal lattice. This deformation is caused by an applied directional pressure named as stress. Group III nitride layers are mostly grown on lattice-mismatched foreign substrates or are stacked as multi-layer heterojunctions. Stress and strain is therefore virtually always present and has to be taken into account. In a general but linear case, stress σ and strain ε are described by tensors, which comprise normal parts (e.g. σ_{xx} , σ_{yy} , σ_{zz}) and shear parts (e.g. σ_{yz} , σ_{xz} , σ_{xy}). The stress tensor elements σ_{ij} are connected with the strain tensor elements ε_{ij} via the elastic constants C_{ij} and Hooke's law. In the wurtzite crystal structure, this law is expressed by equation (2.1) [26].

$$\begin{pmatrix} \sigma_{xx} \\ \sigma_{yy} \\ \sigma_{zz} \\ \sigma_{yz} \\ \sigma_{xz} \\ \sigma_{xy} \end{pmatrix} = \begin{pmatrix} C_{11} & C_{12} & C_{13} & 0 & 0 & 0 \\ C_{12} & C_{11} & C_{13} & 0 & 0 & 0 \\ C_{13} & C_{13} & C_{33} & 0 & 0 & 0 \\ 0 & 0 & 0 & C_{44} & 0 & 0 \\ 0 & 0 & 0 & 0 & C_{44} & 0 \\ 0 & 0 & 0 & 0 & 0 & C_{66} \end{pmatrix} \cdot \begin{pmatrix} \varepsilon_{xx} \\ \varepsilon_{yy} \\ \varepsilon_{zz} \\ \varepsilon_{yz} \\ \varepsilon_{xz} \\ \varepsilon_{xy} \end{pmatrix} \quad (2.1)$$

A single element of the strain tensor ε_{ij} is calculated by the change of the respective lattice parameter a_i from its equilibrium value as a result of stress applied in j -direction. If one assumes fully pseudomorphic growth of a thin film on a substrate (or a different layer acting as a virtual substrate), equation (2.2) is used for the calculation of the in-plane strain components $\varepsilon_{||}$. Herein, a_{layer} and a_{sub} denote the in-plane lattice constants of the deposited film and the underlying substrate, respectively. In an general case, the in-plane lattice constants may be different for the two perpendicular crystal axes. Thus, the calculated in-plane strain may become anisotropic.

$$\varepsilon_{||} = \frac{a_{sub} - a_{layer}}{a_{layer}} \quad (2.2)$$

If one only considers growth on the family of $\{0001\}$, $\{1\bar{1}00\}$, and $\{11\bar{2}0\}$ planes, equation (2.1) can be further simplified because shear components become zero in this case. Moreover, for growth along the $[0001]$ or z -axis direction (c -plane), the in-plane strain is expected to be isotropic. These components can therefore be replaced by $\sigma_{||} = \sigma_{xx} = \sigma_{yy}$ and $\sigma_{\perp} = \sigma_{zz}$, which denote the in-plane and out-of-plane stress, respectively. Thus, equation (2.1) may be rewritten as follows:

$$\begin{pmatrix} \sigma_{||} \\ \sigma_{\perp} \end{pmatrix} = \begin{pmatrix} C_{11} + C_{12} & C_{13} \\ 2 \cdot C_{11} & C_{33} \end{pmatrix} \cdot \begin{pmatrix} \varepsilon_{||} \\ \varepsilon_{\perp} \end{pmatrix} \quad (2.3)$$

The out-of-plane stress component σ_{\perp} is zero because any thin film is free to deform in growth direction. As a consequence, equation (2.3) yields a condition for the strain components, which is given in equation (2.4).

$$\frac{\varepsilon_{\perp}}{\varepsilon_{\parallel}} = -2 \cdot \frac{C_{13}}{C_{33}} \quad (2.4)$$

If the deposition is performed on a nonpolar plane, such as the $(1\bar{1}00)$ m -plane, which is perpendicular to the y -axis in our case, the in-plane strain becomes anisotropic. One can still derive a relation between both in-plane strain values ε_{xx} , ε_{zz} and the out-of-plane strain ε_{yy} :

$$\varepsilon_{yy} = -\frac{C_{12} \cdot \varepsilon_{xx} + C_{13} \cdot \varepsilon_{zz}}{C_{11}} \quad (2.5)$$

The values for the elastic constants, which are required for the calculation of the strain quantities, are given in Table 2.2.

Table 2.2: Elastic constants for GaN, AlN and InN.

		Unit	GaN	AlN	InN
Elastic constants	C_{11}	GPa	390	396	223
[21]	C_{12}	GPa	145	137	115
	C_{13}	GPa	106	108	92
	C_{33}	GPa	398	373	224

2.2.2 Polarization in nitride-based heterostructures

With knowledge of the strain state in the crystal, one can determine both polarization quantities for group III nitride binary semiconductors. Considering the nonlinear

dependency of polarization on strain, equations (2.6- 2.9) were found to give good results for the piezoelectric component P_{pz} for c -plane-oriented films [27].

$$\begin{aligned}
 P_{pz}^{AlN} &= -1.808 \text{ C/m}^2 \cdot \varepsilon_{\parallel} + 5.624 \text{ C/m}^2 \cdot \varepsilon_{\parallel}^2 \quad \text{for } \varepsilon < 0 \\
 P_{pz}^{AlN} &= -1.808 \text{ C/m}^2 \cdot \varepsilon_{\parallel} - 7.888 \text{ C/m}^2 \cdot \varepsilon_{\parallel}^2 \quad \text{for } \varepsilon > 0 \\
 P_{pz}^{GaN} &= -0.918 \text{ C/m}^2 \cdot \varepsilon_{\parallel} + 9.541 \text{ C/m}^2 \cdot \varepsilon_{\parallel}^2 \\
 P_{pz}^{InN} &= -1.373 \text{ C/m}^2 \cdot \varepsilon_{\parallel} + 7.559 \text{ C/m}^2 \cdot \varepsilon_{\parallel}^2
 \end{aligned} \tag{2.6-2.9}$$

One should keep in mind that both piezoelectric and spontaneous polarization in [0001] direction is also present for layers with different orientations like $[11\bar{2}0]$ or $[1\bar{1}00]$. However, the polarization field only has an in-plane component here. In this case, no effects on the vertically stacked device can occur. For that reason, the detailed calculation is omitted here.

To obtain the total polarization value for a binary compound, one has to add the spontaneous polarization P_{sp} , which is a material constant for the group III nitrides and found in Table 2.1. For many practical applications, the polarization of ternary alloys is also of interest. A Vegard-like rule can be applied here. In case of spontaneous polarization, an additional bowing parameter is required [27]. Equations (2.10-2.14) provide all necessary formulas for the calculation of polarization values in ternary nitride alloys.

$$\begin{aligned}
 P_{pz}(A_x B_{1-x}) &= x \cdot P_{pz}(A) + (1-x) \cdot P_{pz}(B) \\
 P_{sp}(Al_x Ga_{1-x} N) &= x \cdot P_{sp}(AlN) + (1-x) \cdot P_{sp}(GaN) + 0.019 \text{ Cm}^{-2} \cdot x \cdot (1-x) \\
 P_{sp}(In_x Ga_{1-x} N) &= x \cdot P_{sp}(InN) + (1-x) \cdot P_{sp}(GaN) + 0.038 \text{ Cm}^{-2} \cdot x \cdot (1-x) \\
 P_{sp}(Al_x In_{1-x} N) &= x \cdot P_{sp}(AlN) + (1-x) \cdot P_{sp}(InN) + 0.071 \text{ Cm}^{-2} \cdot x \cdot (1-x)
 \end{aligned} \tag{2.10-2.14}$$

In the following, the effect of polarization on c -plane-oriented heterostructures is exemplarily demonstrated for a QW consisting of a GaN/In_xGa_{1-x}N/GaN layer stack. QW are typically grown with very low thickness, so a fully strained well can be assumed. Depending on the composition and using the equations above, one can

obtain values for both the total polarization fields and the resulting fixed interface charge density σ_{int} . The latter is determined from the difference between the single total polarization quantities of adjacent layers. The results are displayed in Figure 2.2. In this configuration, the GaN film is strain-free, so only spontaneous polarization is present in the barrier. The values in Table 2.1 already indicate that the difference between spontaneous polarization in GaN and $\text{In}_x\text{Ga}_{1-x}\text{N}$ is rather small. Thus, predominantly the piezoelectric polarization contributes to the total fixed interface charge. Depending on indium (In) concentration, values between $\sim 10^{12} \text{ cm}^{-2}$ and $\sim 10^{14} \text{ cm}^{-2}$ are obtained. It is easy to imagine that such high sheet charge density has a great impact on the physical properties of the QW.

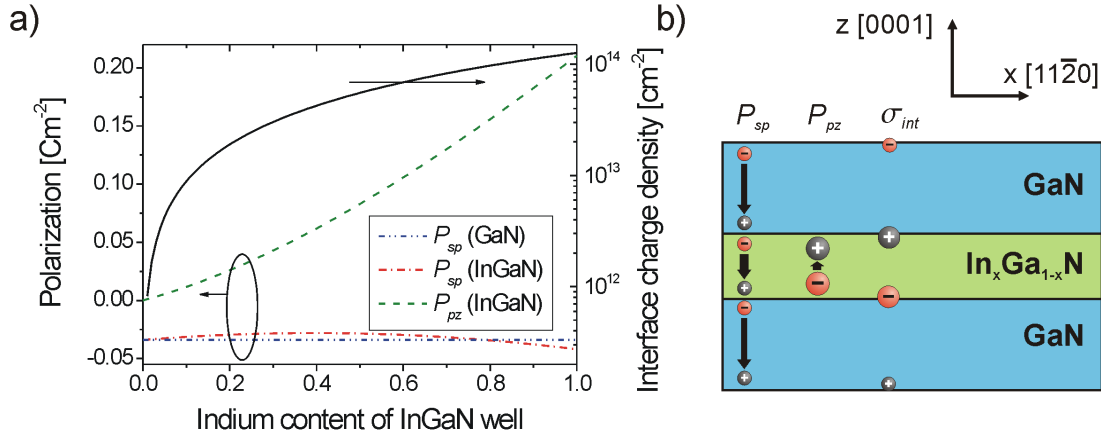


Figure 2.2: Calculated spontaneous and piezoelectric polarization and interface charge density in an $\text{In}_x\text{Ga}_{1-x}\text{N}/\text{GaN}$ QW for different In contents (a) and schematic representation of polarization-induced interface charges in the layer stack (b)

The fixed interface charges can physically be described by an electric displacement field D . This vector is related to the total polarization P , the electric field E , and the vacuum permittivity ϵ_0 via equation (2.15), which allows the calculation of E within the QW. The impact of E is easily visualized using the band diagram.

$$D = \epsilon_0 \cdot E + P \quad (2.15)$$

In Figure 2.3 a), a simulated band diagram for an InGaN/GaN QW is shown. The simulation was performed with a freeware software called ‘bandeng’ [28]. A GaN/In_{0.2}Ga_{0.8}N/GaN layer stack with well/barrier thicknesses of 3 nm and 15 nm and a background donor concentration of 10^{14} cm^{-3} was exemplarily assumed. The results illustrate the tilting of both the conduction (E_C) and valence (E_V) band energy due to the polarization fields. Together with the valence band offset between In_{0.2}Ga_{0.8}N and GaN, this tilt leads to the generation of a minimum in E_C near the upper In_{0.2}Ga_{0.8}N/GaN interface. According to Fermi statistics, this translates to an electron accumulation at the boundary. In a same way, E_V exhibits a maximum near the lower well/barrier interface, leading to a confinement of holes at this position. For optoelectronic devices, two effects arise from this: On the one hand, the different positions of electron and hole wave functions impede the recombination of carriers. Since a spatially direct transition is no longer possible, the probability of radiative recombination decreases, lowering the quantum efficiency of a device.

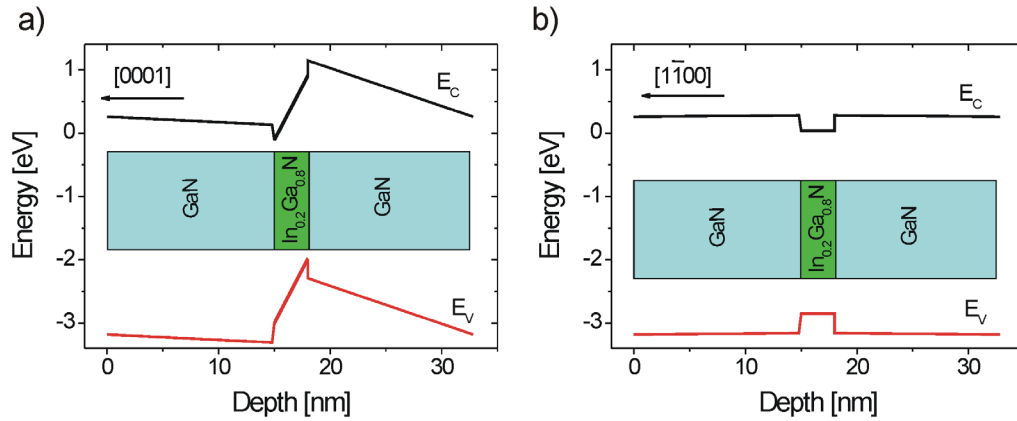


Figure 2.3: Simulated band diagram of a single In_{0.2}Ga_{0.8}N/GaN QW with (a) and without (b) polarization in growth direction. A low (10^{14} cm^{-3}) mobile electron density was assumed. Band offsets are caused by the fixed polarization charge σ .

On the other hand, one can see that the transition from the minimum of E_C to the maximum of E_V exhibits a lower energy compared to the In_{0.2}Ga_{0.8}N bandgap. Moreover, this energetic position may be changed during operation if the density of mobile charge carriers in the well is varied. Additional carriers screen the fixed

polarization charges and thereby lower D . The altered electric field corresponds to a different tilting of E_C and E_V and consequently to a changed effective bandgap. As a result, the emission wavelength of an LED is varied when different currents are applied. This phenomenon of decreased recombination efficiency and current-induced wavelength shift is named as quantum-confined Stark effect (QCSE) [11]. It can be avoided if a QW is grown along nonpolar directions like the $[1\bar{1}00]$ m -direction. In this case, the fields are not oriented along the heterostructure interface, so the polarization difference does not affect the band diagram [29]. The simulated result of an equally stacked $\text{In}_{0.2}\text{Ga}_{0.8}\text{N}/\text{GaN}$ QW without polarization along growth direction is shown in Figure 2.3 b). Flat band conditions are established in the QW here, so a good overlap of electron and hole wave functions is obtained. Thus, neither decreasing of quantum efficiency nor wavelength shift will appear in such a structure. More sophisticated simulations also indicate distinctly higher internal quantum efficiencies (IQE) for QW heterostructures grown along nonpolar directions compared to their c -plane counterparts [30]. However, this study also pointed out a strong influence of the defect density. This highlights the requirement of intense experimental research on nonpolar material fabrication and optimization.

The absence of the QCSE has also been proven experimentally for both a -plane and m -plane QW heterostructures [14, 31]. Moreover, recent demonstrations of devices based on m -plane films indicate the high potential of this approach. Amongst them, an LED emitting in the blue-violet region with an external quantum efficiency (EQE) of up to 45% has been presented [32]. Another promising result is the successful fabrication of an m -plane LD operating at 500 nm wavelength with a maximum optical output power of 15 mW at a threshold current density of only 3.1 kA/cm^2 [33]. However, these devices are produced on bulk GaN substrates, which are costly and limited in size and availability. If the deposition is performed on cheaper and widely available foreign substrates, extensive defect formation has been observed, which obviously causes a dramatic decrease of radiative recombination [34, 35]. Consequently, only limited device performance with LED EQE of 2.4% has up to now been achieved on such platforms [36]. Thus, further optimization of the heteroepitaxial growth process with nonpolar surface orientations has to be done. A basic understanding of the new effects arising in nonpolar GaN epitaxy is one prerequisite to achieve this goal.

3 Theoretical aspects in nonpolar GaN epitaxy

The unique feature of group III nitride crystals deposited on a nonpolar plane compared to the polar c -plane is the new orientation of the c -axis within the growth plane. This gives rise to an intrinsic anisotropy of nonpolar GaN films. One can categorize the semiconductor properties, which are affected by this anisotropy, as follows:

- Crystal and defect structure
- Electronic band structure
- Thermal characteristics
- Mechanical properties

For thin film deposition and the typical applications in electronic and optoelectronic devices, the first two properties are most important and discussed hereafter.

3.1 Anisotropy of crystal and defect structure

3.1.1 Anisotropic strain and defects

An obvious anisotropic quantity for any nonpolar layer is the lattice mismatch to the underlying substrate or thin film. The widely accepted formula for the mismatch m given in equation (3.1) can be calculated for the two orthogonal in-plane axes along $[0001]$ and $[11\bar{2}0]$.

$$m = \frac{a_{sub} - a_{lay}}{a_{lay}} \quad (3.1)$$

Herein, a_{sub} and a_{lay} refer to the in-plane lattice constants for the substrate and layer, respectively. Lattice mismatch is the origin of strain in the epitaxial film. If no

relaxation occurs, this mismatch directly translates into the respective in-plane strain values ε_{xx} , ε_{zz} , which are correlated with the out-of-plane strain ε_{yy} via equation (2.5).

Anisotropic strain itself can have an impact on optical and electrical properties since it changes the band structure, which will be discussed in section 3.2. From a crystallographic point of view, a rather important matter is the strain relaxation and defect formation. In analogy to *c*-plane GaN growth, strain is partly relieved by the introduction of misfit dislocations at the substrate-layer interface and the formation of line defects with screw- and edge-type components [37]. Line defects are characterized by their Burgers vector b and dislocation line vector l . The alignment of these vectors determines whether a screw-type ($b \parallel l$) or an edge-type ($b \perp l$) character is present. A detailed description of defect types in general can be found elsewhere [38]. For the identification of different defect types using diffraction techniques, the diffraction g vector is an important quantity. It is defined according to equation (3.2), wherein k_s and k_i are the wave vectors for the scattered and incident (electron or X-ray) beam. Defects are visible or in contrast if the scalar product of $g \cdot b$ yields an integer value.

$$g = k_s - k_i \quad (3.2)$$

These general aspects of defect types and visibility apply equally to both polar and nonpolar orientations. However, defect types with an anisotropic character are additionally present in nonpolar GaN layers. It is important to note that this defect anisotropy is not directly correlated to the anisotropy of strain caused by the different lattice mismatch values along both in-plane directions. Instead, the anisotropy is connected to the relaxation process, which occurs via a preferential slip plane. Slip generally occurs to minimize the energy of a dislocated crystal. Prominent slip systems in the wurtzite lattice are the families of *c*-planes, *m*-planes, and *a*-planes (compare Figure 2.1 b). Slip planes with larger Miller indices are observed more rarely due to energetic reasons, which are related to the packing density of crystal planes [38]. The {0001} *c*-planes are the closest-packed planes and are thus preferred for slip motion. A well known slip motion process is connected with the generation of basal plane stacking faults (BSF), which is the most common planar anisotropic defect in nonpolar GaN films. Considering an ($1\bar{1}00$) *m*-plane GaN layer, a perfect edge TD located in the (0001) basal plane with a Burgers vector b may split up into two Frank-Shockley-type partial dislocations with b_1 and b_2 and an angle of 60° in

between. The dissociation reaction is given in equation (3.3), which is taken from [39].

$$b = \frac{1}{3} \cdot [11\bar{2}0] = b_1 + b_2 = \frac{1}{3} \cdot [10\bar{1}0] + \frac{1}{3} \cdot [01\bar{1}0] \quad (3.3)$$

A stable situation is achieved by spatial separation of the two partial dislocations balancing the repulsive and attractive forces between them. The area in between these line defects withstands a planar defect, which is called I_2 -type BSF. Stacking faults in general are characterized by an interrupted sequence in the stacking of closely-packed planes in the crystal. A BSF is described by the plane, which the stacking fault is located in and a displacement vector R indicating the relative shift of atoms in the faulted crystal domain with respect to the regular lattice position. Figure 3.1 a) gives a schematic overview of this exemplary defect dissociation and slip process.

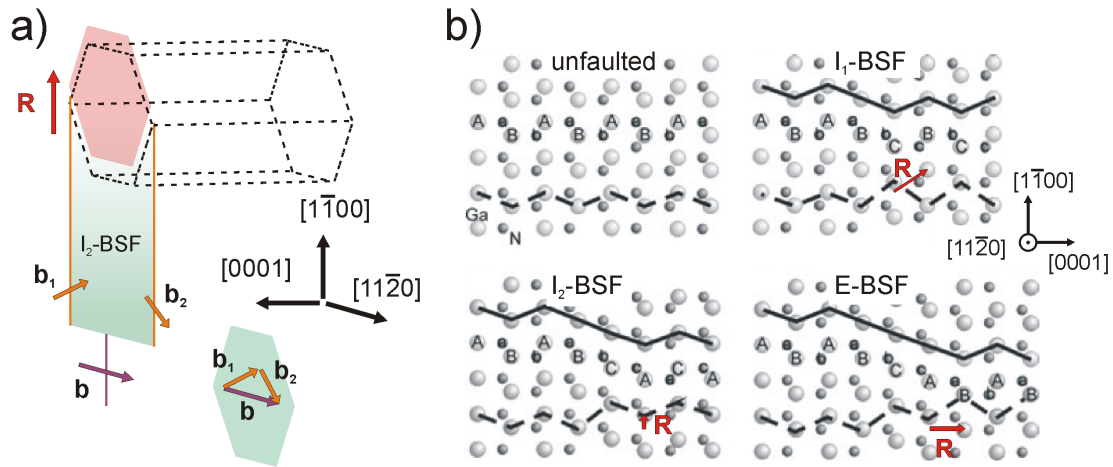


Figure 3.1: a) Schematic view of dissociation process of an edge-type dislocation into two partial dislocations leaving an I_2 -BSF in between, which shifts one basal plane by $R = 1/3[1\bar{1}00]$. b) Comparison of the unfaulted wurtzite lattice and the crystal structure with I_1 -, I_2 -, and E-type BSF (after [40]).

The stacking sequence of the (0001) basal plane in perfect wurtzite crystals is: “ABABABABA...”. The letters A and B denote sub-lattice structures consisting of atomic III-N bilayers. Four distortions of this sequence are known and named as BSF of type I_1 , I_2 , I_3 , and E [41]. The I_1 -type BSF is formed by the removal of one basal

plane (displacement of $1/2[0001]$) and an additional slip along $1/3[1\bar{1}00]$. For the I_2 -type BSF, only a slip along $1/3[1\bar{1}00]$ occurs. I_1 and I_2 stacking faults are usually surrounded by Frank ($b = 1/6[2\bar{2}03]$) and Frank-Shockley type ($b = 1/3[1\bar{1}00]$) partial dislocations, respectively. I_3 -BSF consist of two neighbouring BSF of I_2 -type. All intrinsic BSF are accompanied by different atomic positions of the crystal domains on both sides of the BSF. This is not the case for the extrinsic (E-type) BSF, which involves the insertion of an extra plane only without changing the further atomic stacking sequence. The E-type BSF is bound by a Frank partial dislocation. Table 3.1 summarizes all four BSF types with their stacking sequence and displacement vector R . The distortion of the wurtzite crystal structure for the I_1 -, I_2 -, and E-type BSF in comparison to the unfaulted lattice is additionally visualized in Figure 3.1 b).

The formation of stacking faults may also lead to strain relaxation. In this case, the displacement vector of the respective defect must have an out-of-plane component (with respect to the basal plane). This is for example not the case for the I_2 -BSF. Its generation has been proposed to be due to some growth error or substrate imperfection [42].

Table 3.1: Stacking and displacement vector of BSF types [41].

BSF type	Stacking sequence	Displacement vector R
Intrinsic I_1	ABABCBCBC	$1/6[2\bar{2}03]$
Intrinsic I_2	ABABCACAC	$1/3[1\bar{1}00]$
Intrinsic I_3	ABABCBABA	none
Extrinsic E	ABABCABAB	$1/2[0001]$

A common feature of all BSF is the special stacking sequence “ABC” which corresponds to the stacking of a face-centred cubic lattice. This thin cubic film is under high uniaxial compressive strain, which shifts the conduction band to form a potential well in the band diagram [43]. The conduction and valence band offsets of this type-II QW have been calculated to be 122 meV and -62 meV, respectively [44]. Although

only electrons are confined within the QW, holes are still attracted by the Coulomb force and form excitons, which may recombine at an energy of ~ 0.1 eV below the bandgap of GaN [44]. Such additional photoluminescence (PL) emission peak at 3.41 - 3.42 eV at 10 K was experimentally found for I_1 -type BSF in m -plane and a -plane GaN [45-48]. It is important to note that this emission quenches at RT indicating that nonradiative recombination paths may become dominant. Furthermore, the appearance of this emission peak is always accompanied by a lowered direct or excitonic interband transition. A direct correlation of decreased luminescence and BSF density using cathodoluminescence imaging highlights the negative impact of BSF [49, 50]. Although it is not clear whether the BSF itself or their delineating partial dislocations are acting as nonradiative recombination channels, the reduction of their density is a prerequisite for the fabrication of efficient nonpolar GaN-based optoelectronic devices.

Beside of stacking faults in the basal plane, all prismatic planes, which are either the $\{1\bar{1}00\}$ m -planes or $\{11\bar{2}0\}$ a -planes, may also exhibit a faulted stacking sequence. Prismatic stacking faults (PSF) in one of the six m -planes can be separated into two groups: Inversion domain boundaries (IDB) and stacking mismatch boundaries (SMB). The former denotes an inversion of the polarity across the boundary while the latter indicates a changed stacking sequence. The displacement vector for both defects is $1/2[0001]$. A detailed description can be found in the work of Northrup et al. [51]. The displacement vector for PSF on a 2nd order prismatic $(\bar{1}2\bar{1}0)$ a -plane has been identified by Drum et al. to be $1/2[10\bar{1}1]$ [52]. In nonpolar GaN films, PSF are typically observed in conjunction with I_1 -type BSF, terminating these basal defects on the prismatic plane [53, 54]. In this case, a stair-rod dislocation is present at the intersection of the I_1 -BSF and the PSF. All types of PSF are only rarely observed in c -plane GaN films. This is consistent with their large formation energy, which amounts to of 2.5 eV/nm², 10.5 eV/nm², and 7.2 eV/nm² for the 1st order IDB-type and SMB-type PSF and the 2nd order PSF, respectively [51, 55]. In contrast, BSF of type I_1 , I_2 , I_3 , and E are formed in GaN at much lower energies of 0.11 eV/nm², 0.27 eV/nm², 0.21 eV/nm², and 0.42 meV/nm², respectively [41]. Still, neither BSF are typically present in high-quality c -axis oriented films. As one reason, c -plane layers usually do not exhibit perfect TD lying in the basal plane. Thus, defect dissociation via slip motion is impossible.

3.1.2 Crystal growth anisotropy

Another impact of crystal anisotropy is connected to the epitaxial deposition process itself. To understand this, one needs to consider the surface diffusion of impinging species before final incorporation into the lattice takes place. In a simplified model, this process is temperature-controlled and can be described by an Arrhenius equation:

$$D_{\text{adatom}}(T) = D_{\text{adatom}}(T = 0 \text{ K}) \cdot \exp\left(-\frac{E_A}{k_B \cdot T}\right) \quad (3.4)$$

In equation (3.4), D_{adatom} denotes the lateral adatom diffusion coefficient on the crystal surface, k_B is known as Boltzmann constant, T is the temperature of the crystal, and E_A represents the energy barrier for species transport on the crystal surface. The latter value is very important since it is not only influenced by monatomic steps and kinks on the surface but also affected by the arrangement of atoms in the lattice itself. A generally anisotropic lateral potential distribution of the underlying substrate or film lattice will therefore have an effect on the adatom mobility. Calculations based on density-functional theory have shown that in case of m -plane GaN surfaces, one has to consider different activation energies E_A of 0.93 eV and 0.21 eV for the $[0001]$ and $[11\bar{2}0]$ direction, respectively [56]. This large difference may potentially impact the morphology and defect characteristics of the deposited film. On the other hand, one should keep in mind that other influences like surface preparation, substrate offcut, and defects like stacking faults can also alter the diffusion barriers.

3.2 Effect of crystal anisotropy on electronic band structure

With the unique c -axis of GaN lying in the growth plane of nonpolar films, basic electronic and optical properties become anisotropic as well. The underlying physics can be visualized in the electronic band structure, which is partially displayed for unstrained wurtzite GaN at 300 K in Figure 3.2 a). It shows three top valence bands (VB) at the centre point Γ of the Brillouin zone ($k = 0$): The heavy hole (HH), light hole (LH) and crystal field split-off hole (CH) band [57].

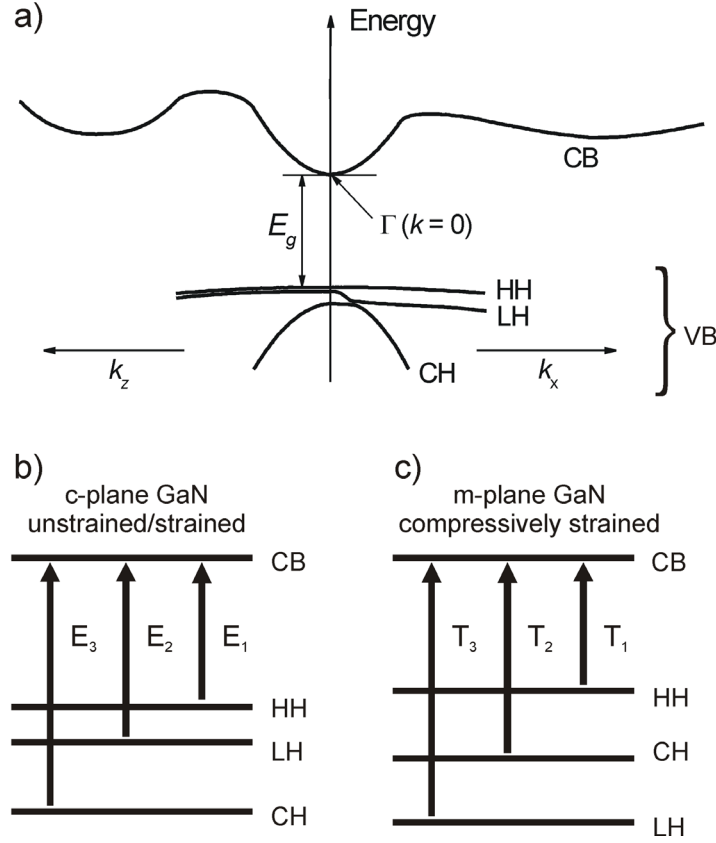


Figure 3.2: a) Illustration of the electronic band structure near the Brillouin zone centre point Γ for unstrained wurtzite GaN at 300 K (after [58]). Comparison of the energy levels at Γ for c-plane GaN (b) and m-plane GaN (c) under compressive strain.

Excitons with holes in one of the three VB are named as A , B , and C excitons and the transition energies from the three VB to the conduction band (CB) are called E_1 , E_2 and E_3 , respectively. If one defines X , Y , Z as directions for the $[11\bar{2}0]$ a -axis, the $[1\bar{1}00]$ m -axis and $[0001]$ c -axis (compare Figure 2.1), respectively, the hole wave functions in c -plane GaN are of type $|X \pm iY\rangle$ in case of the E_1 and E_2 transitions and of type $|Z\rangle$ for transition E_3 [57]. Due to the symmetry in the basal plane, this is valid for both unstrained and biaxially strained c -plane GaN. This means that no preferential polarization of emission (along X or Y) occurs.

When going to a nonpolar orientation of the layer like the (1 $\bar{1}$ 00) *m*-plane, two effects arise: On the one hand, the new alignment of the *c*-axis in the growth plane changes the hole wave functions, removing the equivalence of the HH and LH band so that in-plane polarization anisotropy is present even without external strain [59, 60]. On the other hand, the in-plane symmetry is broken. As a result, strain will change the energy levels of the valence subbands. Calculations show that for compressive strains $\varepsilon_{XX} \leq -0.2\%$, the LH band decreases in energy and is now located below the CH band, while the HH band is pushed to higher energy [61]. The situation at the Γ point for compressively strained *m*-plane GaN in comparison to strained or unstrained *c*-plane GaN is depicted in Figure 3.2 b) and c). It is common to introduce the new notations T_1 , T_2 , T_3 for the transition energies from the HH, CH, and LH band to the CB band, respectively. With the changed orientation and applied strain, the HH, CH and LH states now have a predominantly $|X\rangle$ -, $|Z\rangle$ - and $|Y\rangle$ -like character. One can thus expect polarization of emission for the T_1 and T_2 transitions along X ($\perp c$) and Z ($\parallel c$), which has also been proven experimentally [61-63]. The T_3 emission is polarized in growth direction and thus not detectable. The degree of polarization (*DoP*) of emitted light is defined by equation (3.5), which uses the maximum emission intensity components parallel and perpendicular to the *c*-axis $I_{\perp c}$ and $I_{\parallel c}$, respectively:

$$DoP = \frac{I_{\perp c} - I_{\parallel c}}{I_{\perp c} + I_{\parallel c}}. \quad (3.5)$$

Since the bending of the conduction and valence bands determines the mobility of carriers μ , an altered band structure can also give rise to an anisotropy of the electronic properties. Considering a simple scattering model, one finds that carrier mobility is inverse proportional to the effective mass according to equation (3.6) [64].

$$\mu = \frac{q}{m^*} \cdot t_{scat} \quad (3.6)$$

Herein, q denotes the elementary charge, m^* is the effective carrier mass, and t_{scat} is defined as the mean time between two scattering events. For the determination of the effective mass parameters, both the altered orientation with respect to the surface as well as the strain state have to be considered. Theoretical studies have been carried out to determine the electron and hole masses along the three crystal directions

without consideration of strain. It was found that the conduction band exhibits almost no anisotropy [57, 65]. Thus, a fixed effective electron mass of $0.20 \cdot m_0$ can be assumed (m_0 being the free electron mass) [21]. In contrast, each of the three effective hole masses are direction-dependent [57]. This anisotropy can also be qualitatively recognized from the different curvatures of the valence subbands in k_x and k_z direction displayed in Figure 3.2 a). A lower curvature corresponds to a larger effective mass. The calculated values for unstrained conditions are given in Table 3.2.

Table 3.2: Hole effective masses for heavy-, light-, and crystal field split-off band along the directions parallel and perpendicular to the c -axis [57].

		HH	LH	CH
\parallel	c -axis	$1.10 \cdot m_0$	$1.10 \cdot m_0$	$0.15 \cdot m_0$
\perp	c -axis	$1.65 \cdot m_0$	$0.15 \cdot m_0$	$1.10 \cdot m_0$

As a consequence of these considerations, a slightly higher hole mobility parallel to the GaN c -axis direction can be expected for unstrained m -plane GaN films. If strain cannot be neglected any more, one has to recalculate these numbers. Again, additional anisotropy is only introduced for the hole masses, since the conduction band is insensitive to strain. The influence of strain on the valence bands was studied by Fu et al. [66], who found that in case of GaN with nonpolar surfaces, the hole masses are altered with a generally anisotropic character for both isotropic and anisotropic strain. A practical aspect of this situation is related to the design of electronic devices with a preferred hole or bipolar transport direction like photodetectors or transistors. If carrier transport occurs on a nonpolar surface, the current path should usually be adapted to the direction of higher hole mobility.

4 Substrates for nonpolar GaN epitaxy

The present study deals with the deposition of *m*-plane GaN films, focussing on new physical effects arising in nonpolar heterostructures. As discussed in the previous section, the substrate has a major impact on the *m*-plane or *a*-plane layer properties. In analogy to *c*-plane heteroepitaxy, large mismatch values should be avoided since the generated TD are most probably the origin of hampered device performance, although the exact role of the different defect types is still under discussion [4, 6, 67, 68]. This chapter reviews some substrate materials suitable as platform for nonpolar GaN epitaxy. With the recent development of bulk GaN growth techniques, nonpolar GaN has also become available as potential substrate and is described at first. This is followed by a comparison of other common substrate materials. The properties, advantages and drawbacks of the substrate used in this work, γ -LiAlO₂, will be discussed in detail in the third subsection.

4.1 Free-standing nonpolar GaN substrates

Since the (anisotropic) lattice mismatch is the driving force for defect generation in the deposited layer, the best, i.e. strain-free, solution would be to use the same material for both substrate and deposited film. However, standard crystal production techniques as the Czochralski or Bridgman method are not suitable for GaN boule fabrication because of the high melting temperature and vapour pressure of GaN [69].

Other technologies have been developed to fabricate free-standing GaN boules. Among these vapour-phase-based techniques are Hydride Vapour Phase Epitaxy (HVPE) [70], Ammonothermal growth [71], and the Na-flux method [72]. Bulk crystals, which are produced with (0001) orientation, can be diced in the (11 $\bar{2}$ 0) or (1 $\bar{1}$ 00) plane and used as a platform for *a*-plane or *m*-plane GaN homoepitaxy, respectively. Since both length and diameter of the fabricated *c*-axis-oriented GaN boules are yet very limited, the approach is hampered by the small size of the resulting free-standing substrates. Currently, the largest reported wafer dimension for

m-plane GaN substrates produced by the Ammonothermal method is $22 \cdot 11 \text{ mm}^2$ [73]. Although impurity incorporation remains a serious problem for all three techniques [74-76], the crystal properties of the GaN substrates are excellent and have opened up the way for performance records in nonpolar LED and LD fabrication [32, 33].

Another way to achieve free-standing nonpolar GaN wafers is to separate a thick nonpolar GaN film from the foreign substrate on which it was grown. HVPE has been used for the growth of *m*-plane GaN on LiAlO_2 , which may spontaneously delaminate after cool-down [77]. By this way, bulk *m*-plane GaN wafers with 50 mm diameter can be produced. Yet, these wafers exhibit large defect densities and a low surface quality. Recently, the basic idea has been transferred to the epitaxy of thick *m*-plane GaN films on the chemically more stable *m*-plane sapphire substrate [78]. The spontaneous separation was achieved by the deposition of an aluminium carbide buffer layer and led to substrate diameters of up to 45 mm. However, the film quality is still inferior to material diced from *c*-axis-oriented boules.

A common drawback for all free-standing *m*-plane GaN substrates is their relatively high cost. Although it is very likely that one of these technologies will be available at larger size and slightly reduced price, cost issues will probably still prevent the introduction in standard LED fabrication processes.

4.2 Foreign substrate materials for nonpolar GaN epitaxy

By far the largest amount of GaN deposition processes is carried out via heteroepitaxy on foreign substrates. Reasons for this are the better availability and lower cost compared to free-standing GaN wafers because virtually all materials in use for GaN heteroepitaxy are produced by the Czochralski pulling method or some related technique suitable for mass production. Beside of these economical aspects, two other advantages favour epitaxy on foreign substrates. One of them is the difference in refractive index between deposited film and substrate, which allows for optical *in situ* monitoring of growth rate and morphology. Another feature is the possibility of applying substrate lift-off techniques or using materials with lower thermal resistivity compared to GaN in order to improve the heat transfer in optoelectronic devices. On

the other hand, the most serious drawback for both polar and nonpolar heteroepitaxy is the substrate-lattice mismatch. Any misfit between substrate and deposited film is known to result in TD in *c*-plane GaN layers [37, 79]. Although no direct correlation of misfit and TD density has been demonstrated for nonpolar epitaxy, the general trend of higher defect density with larger substrate-lattice mismatch probably holds also for nonpolar films. As described in chapter 3, BSF are likely to form in nonpolar group III nitride films and are therefore the most dominant defects [54]. A complete physical model regarding their generation and impact on the electronic and optical semiconductor properties is not available at present. It is still obvious that their density should be minimized. Reduced substrate-lattice mismatch is assumed to be helpful for achieving this goal. Beside of the in-plane lattice constant, thermal properties are also of interest when choosing a substrate. Thermal expansion coefficients have to be considered since MOVPE is a high-temperature process, so the in-plane mismatch at elevated temperatures will be altered. Large differences can also cause wafer bowing or even cracking during the cooling down of the specimen. Table 4.1 summarizes some important properties of some common substrate materials for nonpolar GaN epitaxy. For the sake of completeness, freestanding *m*-plane GaN is also listed here. Since the epitaxy of GaN with a nonpolar surface comes with a two-fold in-plane symmetry only, both lattice mismatch and thermal expansion coefficient are anisotropic. The values in Table 4.1 are given for both in-plane directions of the deposited *m*-plane or *a*-plane GaN film. A further characteristic of foreign substrates is that no 1:1 coincidence of the *m*-plane GaN unit cell with the substrate unit cell may occur. In this case, the altered coincidence in the respective direction is indicated in Table 4.1. For instance, a serial arrangement of three GaN unit cells along the *c*-axis direction matches the *c* lattice constant of the *r*-plane sapphire and *m*-plane 6H-SiC substrate. γ -LiAlO₂ exhibits a tetragonal structure with its *c* lattice constant accommodating twice the *a* lattice constant of *m*-plane GaN. The calculated mismatch values represent the residual mismatch taking into account this special atomic arrangement.

Table 4.1: Properties of substrates for nonpolar GaN epitaxy at $T = 300$ K. All values refer to the orientation with respect to the GaN c -axis.

	structure	in-plane lattice constants [nm]		mismatch to a -/ m -plane GaN [%]		thermal expansion coefficient [10^{-6} K $^{-1}$]	
		\perp c	\parallel c	\perp c	\parallel c	\perp c	\parallel c
m -plane GaN [23]	wurtzite	0.3189	0.5185	-	-	3.43	3.34
r -plane Al ₂ O ₃ [22, 80]	hexagonal	0.4759	1.5384 (1 : 3)	-13.8	-1.1	7.3	10.6
m -plane Al ₂ O ₃ [22]	hexagonal	1.2991 (1 : 4)	0.476	1.8	-8.2	7.3	8.5
m -plane 6H-SiC [81]	wurtzite	0.3073	1.512 (1 : 3)	-3.6	-2.8	3.4	3.3
(100) γ -LiAlO ₂ [15, 82]	tetragonal	0.6268 (1 : 2)	0.5169	-0.3	-1.7	14.9	6.5

Considering the lattice mismatch of the listed materials, r -plane and m -plane Al₂O₃ appear to be less suitable for high-quality film epitaxy. However, since the growth of Al₂O₃ ingots is already a mature technology, both substrates can be fabricated at relatively low cost and are readily available. For GaN growth on m -plane Al₂O₃, both (1 $\bar{1}$ 00) m -plane as well as (11 $\bar{2}$ 2) semipolar oriented GaN nucleation may occur, which puts some constraints on the optimization of deposition processes on this sapphire orientation [83]. Thus, many studies focussed on the growth of a -plane GaN on r -plane Al₂O₃. To overcome the disadvantage of large lattice mismatch, a multi-step deposition process with fine adjustment of growth temperature, pressure and V/III ratios is typically applied [84-86]. Although elaborated deposition schemes can lead to clearly reduced defect densities [87], the typical BSF densities still range in the order of 10^5 cm $^{-1}$ and hinder improved device performance. For achieving higher

film quality, more sophisticated epitaxial lateral overgrowth (ELOG) techniques have to be applied [88, 89].

Similar statements can generally be made for the deposition of *m*-plane GaN thin films on the much more expensive *m*-plane 6H-SiC or 4H-SiC substrate. In this case, the lower substrate-lattice and thermal mismatch facilitates the production of high-quality films, and impressive results regarding p- and n-type doped films have been achieved. Among those are very high hole concentrations of up to $7 \cdot 10^{18} \text{ cm}^{-3}$ and electron mobilities peaking at $500 \text{ cm}^2/\text{Vs}$ [90]. Still, even sophisticated buffer layer designs are not able to reduce the BSF densities below a level of 10^5 cm^{-1} [91]. The large number of BSF is also a likely reason for the typical surface morphology of heteroepitaxially grown *m*-plane GaN films with formation of “slate-like” features elongated along the $[11\bar{2}0]$ direction [45, 92, 93]. The usage of ELOG or sidewall ELOG can help to reduce the BSF density and has also been found to be a prerequisite to achieve smooth surfaces with monoatomic steps in the wing region of the overgrown films [45, 92, 93]. However, the increased processing effort will obviously put a constraint on the cost advantage of both the *m*-plane SiC and *r*-plane sapphire substrates.

This work is focused on the epitaxy of LiAlO_2 substrates, which possess the lowest mismatch to *m*-plane GaN. To understand the motivation and results of the described experiments, the properties of a LiAlO_2 wafer will be discussed in advance.

4.3 Properties of (100) γ -lithium aluminium oxide (LiAlO_2)

LiAlO_2 can crystallize in three structures, which differ by the coordination of the metal ions and are known as the α -, β -, and γ -phase [94]. The substrates used in this study are made of the thermodynamically stable γ -phase. This tetragonal crystal structure is characterized by a tetrahedral arrangement of the lithium (Li) and aluminium (Al) atoms [95]. Having one 4-fold and two 2-fold symmetry axes, it can be classified as space group $P4_12_12$ [15]. The lattice constants and thermal expansion coefficients of γ - LiAlO_2 are given in Table 4.1. It becomes apparent that the low mismatch to *m*-plane GaN of -1.7% and -0.3% along $[0001]_{\text{GaN}}/[010]_{\text{LiAlO}_2}$ and $[11\bar{2}0]_{\text{GaN}}/[001]_{\text{LiAlO}_2}$, respectively, is a unique advantage of this material. The (100)

LiAlO_2 surface exhibits also an almost hexagonal symmetry, so good lattice matching is even possible for GaN crystals oriented towards the c -axis. The situation is illustrated in Figure 4.1. The substrate-lattice mismatch for c -plane GaN amounts to -1.7% and -6.4% for the $[001]$ and $[010]$ direction of LiAlO_2 , respectively. Indeed, several early reports on the growth of GaN on LiAlO_2 resulted in c -axis oriented material [96-98]. It has been speculated that the crystal orientation may depend on the deposition technique, i.e. growth by MBE resulting in m -plane films and growth by MOVPE leading to c -plane orientation [97]. However, in a majority of later reports using MOVPE, only the nucleation of m -plane crystals was observed [18, 99]. Moreover, phase mixture was also observed in MBE-grown specimens [100, 101]. It appears plausible that obtaining the energetically favourable nonpolar orientation is only a matter of process optimization. One should also be aware that the special atomic arrangement of the LiAlO_2 crystal enables the nucleation of m -plane GaN not only to take place on the rectangular (Li, Al)-sub-lattice (m -plane 1) but also on the very similar sub-lattice formed by the four oxygen (O) atoms (m -plane 2) (compare Figure 4.1).

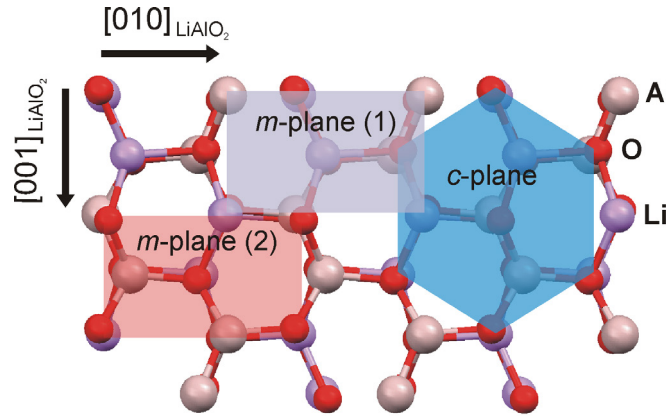


Figure 4.1: Arrangement of the GaN unit cells on the LiAlO_2 substrate visualized using a ball-and-stick model. The red, violet and blue shaded areas indicate possible nucleation sites for $(1\bar{1}00)$ m -plane and (0001) c -plane GaN.

The latter arrangement is not fully rectangular and differs in the atomic spacing along $[001]$, which is 0.343 nm compared to of 0.313 nm for the (Li, Al) sub-lattice. The nucleation of neighbouring GaN islands on different sites has been blamed to be

responsible for coalescence problems [102]. However, from an energetic point of view, this situation is not very likely to occur on an ideal LiAlO_2 substrate surface because the mismatch along [001] for island nucleation on the O sub-lattice is as large as 7.6%.

Another special property of LiAlO_2 is its hygroscopic character [103]. Several groups found that prolonged immersion in water greatly increases the roughness of LiAlO_2 substrates [100, 104]. In these experiments, a different etchability of the (100) and ($\bar{1}$ 00) oriented wafers was also found. Lin et al. studied the reaction of ceramic LiAlO_2 with water in detail [105]. They stated that the reaction product with water is a loose layer of $\text{AlO}(\text{OH})$ on the LiAlO_2 surface with Li^+ and OH^- ions being solved in water. In addition, a coating with LiAlO_5 was found to enhance the stability of the LiAlO_2 ceramic [105]. One can assume that similar mechanisms are valid for single-crystalline LiAlO_2 . The sensitivity to water requires special water-free wafer fabrication techniques making polishing a delicate task [106]. Another practical aspect is the need for storage of the polished wafers in a water-free atmosphere since air moisture has been found sufficient to degrade the substrate surface quality [100]. Beside of issues in substrate cleaning and storage, the etchability facilitates substrate removal after device processing or substrate patterning before epitaxy.

Since thin-film deposition is a high-temperature process, thermal stability is an important issue. The melting point of $\gamma\text{-LiAlO}_2$ is known to be $\sim 1700^\circ\text{C}$, which is high enough for MOVPE growth [107]. Thermodynamic calculations show that outgassing of LiO_2 may occur at $\sim 1400^\circ\text{C}$ and above [108]. At lower temperatures, no experimental evidence for significant releasing of species has been found [100]. However, Xu et al. demonstrated that etching of the substrate takes place in an atmosphere made up of hydrogen (H_2) and ammonia (NH_3) at temperatures above 1070°C [109]. It has further been reported that H_2 can easily diffuse inside the LiAlO_2 wafer [110]. One may therefore suspect that the presence of H_2 at high temperatures is causing substrate damaging. This probably explains why most groups tried to avoid the exposure to H_2 in the initial growth stage. [18, 97, 99]. Since H_2 is also available through the cracking of NH_3 , the temperature was usually restricted to 900°C to minimize potential damage by the released H_2 gas. However, a good understanding of the physical and chemical fundamentals regarding substrate stability during MOVPE growth is still lacking.

An important benefit of using γ -LiAlO₂ as a substrate is the potential for its mass production by the standard Czochralski growth method. This was first achieved by Cockayne and Lent in 1981 [107]. For wafers cut in the (100) direction as required for *m*-plane GaN epitaxy, the total dislocation density is typically in the order of 10^4 cm^{-2} , which is a sufficiently low number for group III nitride deposition [109]. One problem described is the appearance of a large number of inclusions within the crystal ingot [107]. These voids have recently been identified as small grains consisting of LiAl₅O₈, which is the Li-poor phase of LiAlO₂ [111]. Further defects like grain boundaries due to polarity inversion or thermal stress during boule growth have also been reported [16, 111]. While it is obvious that the LiAlO₂ fabrication technology is far from being mature and further improvements are required, a direct correlation of these defects to their impact on the epitaxy of GaN thin films was not performed up to now. The only studied connection is the one regarding substrate surface morphology and defects [42, 102]. It has been shown that surface steps on the LiAlO₂ substrate result in a stacking disorder of the deposited GaN film, which is released by slip accompanied by the generation of an I₂-type BSF [102]. Thus, any kind of surface distortion of the substrate is likely to increase the overall defect density. As a consequence, one can conclude that polishing, substrate pretreatment as well as the initial nucleation phase are key parameters for successful *m*-plane GaN epitaxy on LiAlO₂.

5 Tools and methods for epitaxy and characterization

This chapter shortly describes the methods used for sample fabrication and characterization in this work. Since a large number of measurement tools was used, detailed descriptions are limited to non-standard techniques.

The layer growth was performed in an AIXTRON 200/4 RF-S MOVPE reactor equipped with a susceptor for deposition on 2" substrates. Due to the limited number of available 2" LiAlO₂ substrates, the wafers have been cut to smaller pieces (either squares with 12 mm edge length or quarter pieces of 2"). To keep them fixed during epitaxy, a specially prepared sapphire dummy wafer has been used as positioning device. The standard sources for GaN deposition were trimethylgallium (TMGa) and NH₃. The MQW stack was deposited using triethylgallium (TEGa) and trimethylindium (TMIn). The carrier gas could be switched between H₂ and N₂. Both NH₃ and H₂ were introduced through additional purifier systems. The doping sources for n-type and p-type conductive layers were silane (SiH₄) and biscyclopentadienylmagnesium (Cp₂Mg), respectively. The deposition temperature was measured optically via light pipe on the bottom side of the heated susceptor disc and on the wafer surface through a top window (in the following named as surface temperature). The latter was performed using an Laytec EpiR DA TT *in situ* monitoring system, which also allows simultaneous recording of the reflected light at various wavelengths from 280 nm to 770 nm. Reflectivity oscillations at 605 nm wavelength have been used to estimate layer thicknesses and growth rates. The combination of temperature and reflectivity measurement enabled reflectivity correction of the pyrometer signal thus enhancing the accuracy of the surface temperature measurement.

X-ray reflectivity (XRR) scans were performed to determine the thickness and density of very thin films. An X-ray mirror and 2 mm beam mask narrowed the primary beam down to a size of $0.1 \cdot 2 \text{ mm}^2$, while a parallel plate collimator and a 0.1 mm detector slit were employed to reduce the divergence of the reflected beam.

Structural data were collected by X-ray diffraction (XRD) performed on a PANalytical X'Pert Materials Research Diffractometer. The system comprises a 2-crystal

Ge(220) monochromator and an X-ray mirror in the incident beam path. Depending on desired resolution, the diffracted beam is either directly collected in an open detector configuration, which can be narrowed with a 1 mm receiving slit, or measured via the usage of a Ge(220) 2-bounce channel-cut analyzer crystal, for which the measurement is named as high resolution XRD (HRXRD). To gain some information about the anisotropy the crystalline microstructure, two X-ray incident beam directions have been employed for symmetrical scans. This was done in a way that their projection on the surface plane matches the GaN c -axis or a -axis direction, respectively. Omega scans with open detector geometry on the symmetrical reflections $(1\bar{1}00)$, $(2\bar{2}00)$, and $(3\bar{3}00)$ allowed the extraction of the lateral coherence length (LCL) and the mosaic tilt $\Delta\omega_{mos}$ in the two respective crystal directions employing a method described in [112, 113]. The LCL expresses the average lateral extension of an undistorted crystal domain, while the mosaic tilt is a measure for the mean inclination of a crystallite with respect to the growth axis. The measured Omega scan full width at half maximum (FWHM) values for each Bragg angle Θ_{hkl} of the reflection is connected to both quantities according to equation (5.1).

$$FWHM(\Theta_{hkl}) = \Delta\omega_{mos} + \frac{\lambda_{XRD}}{2 \cdot LCL \cdot \sin(\Theta_{hkl})} \quad (5.1)$$

Herein, λ_{XRD} denotes the X-ray wavelength of the XRD system (= 0.15406 nm). The extraction of mosaic tilt and LCL is done by plotting $FWHM(\Theta_{hkl}) \cdot \sin(\Theta_{hkl}) / \lambda_{XRD}$ versus $\sin(\Theta_{hkl}) / \lambda_{XRD}$. A fit of this x-y curve using linear regression with minimum squares yields both the slope, which is proportional to $\Delta\omega_{mos}$, and the intersection with the y-axis, which is inverse proportional to the LCL.

An advanced characterization of the crystal structure was possible by means of cross-sectional transmission electron microscopy (TEM) and high-resolution TEM (HRTEM). This technique enables the visualization and identification of defects in diffraction mode. The diffraction g vector was changed by tilting the specimen with respect to the electron beam. A detailed description of the theory and application of TEM/HRTEM is described in [114]. All observations were carried out on a JEOL JEM-3010 transmission electron microscope with a LaB₆ electron source at a voltage of 300 kV.

In addition, electron channelling contrast imaging (ECCI) was applied to estimate defect densities in the m -plane GaN films [115]. This was performed with a tilting angle of 45° and an acceleration voltage of 30 kV.

Optical investigation was conducted by photoluminescence (PL) spectroscopy. This setup includes a HeCd laser ($\lambda = 325.0$ nm) and a pulsed N₂ laser ($\lambda = 337.1$ nm) for low and high power excitation levels, respectively. To account for the in-plane polarization of the emitted light, a rotatable polarization filter is put in front of the optical fibre which guides the light to the polychromator and CCD detector. PL studies were also performed using the fourth harmonic ($\lambda = 266.3$ nm) of an yttrium aluminium garnet YAG:Nd³⁺ laser, which delivers very high excitation powers. These experiments were carried out with the help of a cylindric lens to excite a 1 mm²-sized spot. The signal is taken from the edges of the sample as illustrated in Figure 5.1 a).

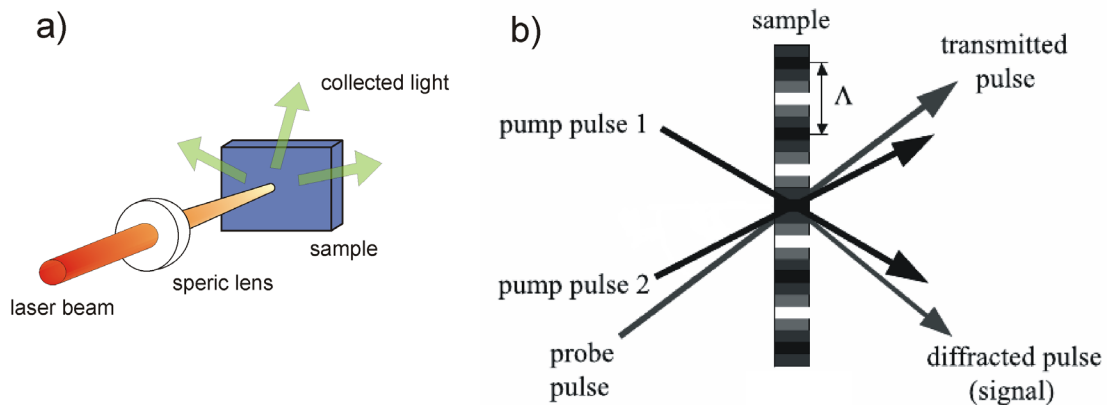


Figure 5.1: Measurement configuration for high excitation PL (a) and for transient carrier grating experiments (b).

Another optical technique employed in this thesis is named four wave mixing (FWM) [116]. The method is based on the generation of a free-carrier transient grating with a grating period Λ by optical pumping of a semiconductor with two interfering “pump” laser beams. A third probe beam is directed on the excited semiconductor area, and its diffracted signal can be used to characterize the quality of the grating and its decay. The beam geometry is shown in Figure 5.1 b). The dependency of the diffraction quality on excitation level can reveal carrier density-dependent recombination

mechanisms. A determination of the transient behaviour of the diffracted signal yields information on minority carrier lifetimes and diffusion lengths in the semiconductor. The measured decay time τ_G of the transient grating is linked to the carrier lifetime τ according to equation (5.2).

$$\tau_G^{-1} = \tau^{-1} + \left(\frac{2\pi}{\Lambda}\right)^2 \cdot D_{bipolar} \quad (5.2)$$

This equation involves a contribution of diffusive decay time characterized by a bipolar diffusion coefficient $D_{bipolar}$. A variation of the carrier grating period Λ allows the separation of diffusive decay and intrinsic carrier lifetime.

Electron and hole mobility and concentration values of nominally undoped *m*-plane GaN films were extracted by Hall measurements on a Bio Rad HL5500 using processed Hall bridge structures for six-point measurements. The latter was done with the help of an inductively coupled plasma reactive ion etching (ICP-RIE) etching step to define a mesa for the Hall bridge structure with 1 mm length and 0.25 mm width. For the etching process a gas mixture consisting of 10 sccm BCl₃, 32 sccm Cl₂, and 5 sccm N₂ were introduced into a low-pressure ($\sim 10^{-2}$ mbar) reaction chamber at a radio frequency power of 550 W. Metal contacts consist of an evaporated stack of Ti/Al/Ti/Au (10/40/150/100 nm). The alignment of the Hall bridges was chosen parallel and perpendicular to the GaN *c*-axis to test for in-plane anisotropy. For Hall test measurements on Mg-doped *m*-plane GaN films, the material was annealed for 15 min at 700 °C in an open tube furnace under flowing N₂. After this step, a conductive silver contact was applied on the sample edges in a van der Pauw geometry and annealed on a hotplate for 5 min at 300 °C. This was followed by standard four-point van der Pauw Hall measurements.

6 Study on pretreatment of the LiAlO_2 surface and its effect on GaN epitaxy

As discussed in section 4.3, the stability of the LiAlO_2 substrate in aggressive environment is limited. To enable successful group III nitride epitaxy, it is essential to be aware of these limitations and to ensure a sufficiently stable surface during nucleation. This chapter begins with basic experiments to elucidate the stability of LiAlO_2 under MOVPE growth conditions, followed by a description of the surface modification taking place during a nitridation step before growth. In a further section, the effect of the nitridation on the subsequent growth of GaN thin films is demonstrated.

6.1 Stability of LiAlO_2 in MOVPE growth environment

In MOVPE growth, two potentially harmful factors for the substrate have to be considered. These are the growth temperature and the presence of reactive substances, such as NH_3 and H_2 . As found by Sun et al., high temperatures up to 1300 °C are not causing any severe decomposition of the substrate in an N_2 ambient [100]. However, growth studies using HVPE have shown that the substrate may locally transform into LiAl_5O_8 through a release of Li_2O in an NH_3/H_2 growth ambient at ~ 900 °C [117]. Also, distinct substrate damage was observed when LiAlO_2 is exposed to H_2 and NH_3 at temperatures above 1070 °C [109].

In the present work, two basic experiments have been performed to elucidate the etching mechanism at high temperature. In a first one, LiAlO_2 substrates were put into the MOVPE chamber and heated up to a surface temperature of either 950 °C, 1080 °C, or 1150 °C under H_2 ambient using a temperature ramp of 50 K/min. The monitored reflectivity of the substrate surface slightly dropped after exceeding 1060 °C, indicating a degraded surface quality by an etching mechanism which is consistent to the reports by Xu et al. [109]. Furthermore, the substrates heated to 1080 °C and 1150 °C exhibit a distinctly changed, opaque surface appearance which

is visible both by bare eye and optical microscopy. The wafer heated to 950 °C does not show any change in morphology and still has a mirror-like surface. One can conclude that an exposure of the LiAlO₂ wafer to H₂ at high temperature has a negative impact on the surface quality. Although no direct degradation by H₂ at 950 °C can be observed, most groups perform the GaN nucleation step on LiAlO₂ in a H₂-free environment [18, 99, 109].

To study the effect of the H₂ ambient at an intermediate deposition temperature of 900 °C, a second experiment was carried out to compare the growth of GaN in N₂ and H₂ ambient. For the deposition of this 300 nm thick GaN film, the reactor pressure was kept at 300 mbar, the V/III ratio was set to 1010, and a growth rate of ~ 20 nm/min was chosen. No pre-deposition was employed, i.e. NH₃ and TMGa were opened at the same time. A photograph of the resulting layer surfaces is displayed in Figure 6.1. While in case of growth under N₂ ambient, a mirror-like surface is achieved, the sample grown directly in an H₂ environment suffers from strong surface degradation visible by bare eye.

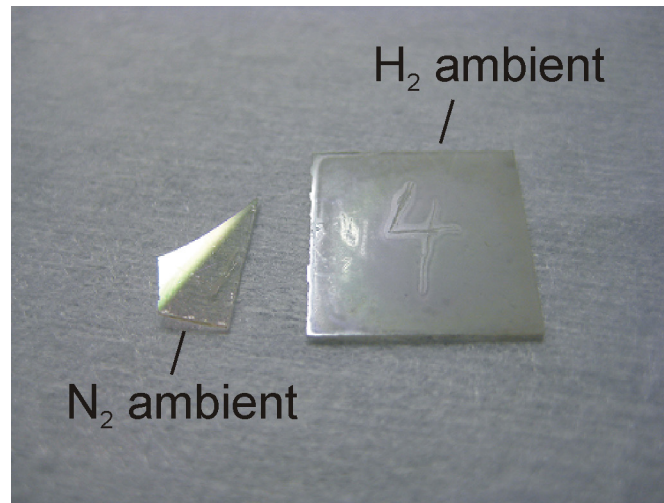


Figure 6.1: Photograph of surface of 300 nm thick GaN films on LiAlO₂ substrate after direct deposition using N₂ and H₂ carrier gas.

The severe surface degradation after the deposition in H₂ ambient may be related to a weakened LiAlO₂ surface stability, which prevents a firm linking of the GaN lattice. A diffusion of H₂ into the LiAlO₂ crystal could be a possible explanation for the

limited mechanical stability during the nucleation of GaN. Further studies would be required to identify the exact origin of this phenomenon. Anyway, the direct exposure of the LiAlO₂ surface to H₂ should be avoided to ensure a proper deposition process.

6.2 Study of nitridation-induced surface modification

Further investigations on the GaN film directly grown in N₂ environment show a low-quality, mixed-phase GaN crystal with both *c*-plane and *m*-plane orientation. This situation can be improved by employing a 2 min nitridation step, as proposed by Dikme et al. [18]. Nitridation, i.e. in-situ exposure to NH₃ at ~ 900 °C, is thought to induce a chemical change of the topmost surface atoms of the substrate stabilizing the surface for subsequent growth. Reed et al. found that during nitridation of LiAlO₂, an Al-N bond forms on the surface, and they suggested that a thin material consisting of a mixed oxide-nitride character with *c*-plane orientation is generated [97]. Thus, the following deposition of GaN by MOVPE also yielded *c*-plane oriented GaN films in their studies. This is supported by the experiments of Richter et al., who reported that the nitridation of LiAlO₂ is accompanied by the releasing of Li and O, which is beneficial for the subsequent growth of thick *c*-plane GaN films by HVPE [98]. Other results for growth of GaN by MOVPE and MBE show that a nitridation step always induces a phase mixture of the GaN layer and should therefore be avoided [99, 100]. In contrast, reports by other groups show phase-pure *m*-plane GaN films after such nitridation step [18, 118].

To shed light on the mechanisms taking place during nitridation, a thorough investigation of the LiAlO₂ surface after nitridation has been conducted. The nitridation step was performed at 900 °C in N₂ ambient using an NH₃ molar flux of 89 mmol/min at a reactor pressure of 300 mbar. A first experiment was aimed at the chemical stability of the modified LiAlO₂ surface. Substrates with and without a 2 min nitridation step were immersed for 5 min in de-ionized water. To check for possible surface etching, AFM scans were performed before and after this procedure. The corresponding surface morphologies are displayed in Figure 6.2. While the surfaces of the layers with and without nitridation are virtually identical before the water dip, distinct changes are revealed thereafter. Only the untreated LiAlO₂ surface exhibits significant morphological changes caused by the etching in water. Elongated stripes without

preferential orientation are uncovered, which increases the root mean square (RMS) roughness from 0.4 nm to 6.4 nm. The stripes are most likely due to sub-surface polishing damage, since a locally damaged crystal will be easier to etch or may have altered hygroscopic properties. Even in undistorted areas of the AFM scan, the substrate surface is significantly rougher after water dipping when no nitridation is performed. The RMS value in an $1 \cdot 1 \mu\text{m}^2$ area increases from 0.2 nm to 1.6 nm after etching. In contrast, only a slight enhancement of the RMS roughness from 0.2 nm to 0.4 nm is present for the sample exposed to NH_3 .

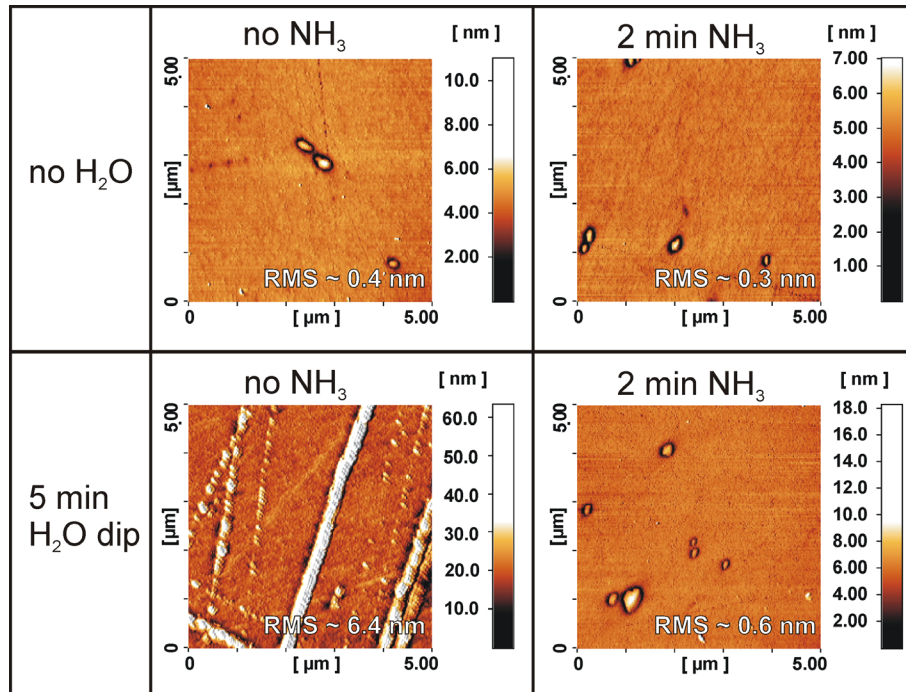


Figure 6.2: AFM surface scans of LiAlO₂ substrates with and without exposure to NH_3 before and after a 5 min water dip.

The clearly reduced etchability by water is an indication for the suspected formation of a nitride-based surface layer with higher stability. To prove this theory, XRR has been carried out on a LiAlO₂ substrate, which was exposed to NH_3 for 5 min. Figure 6.3 shows the XRR spectra of this treated sample and a LiAlO₂ reference together with the fitted simulation curve of a heterostructure consisting of a thin layer. A clearly visible difference of the reflectivity curves of the substrate with and without

exposure to NH₃ reveals the change of the LiAlO₂ crystal surface. The fitting procedure leads to a very good agreement of the measured curve and yields a specific density ρ of 3.07 g/cm³ and a surface roughness of 0.5 nm. Considering the density value in the simulation, the formation of AlN ($\rho = 3.23$ g/cm³ [119]) is the most plausible explanation. The possibility of phase transformation of the topmost γ -LiAlO₂ ($\rho = 2.615$ g/cm³ [95]) surface into α -LiAlO₂ ($\rho = 3.401$ g/cm³ [95]), β -LiAlO₂ ($\rho = 2.600$ g/cm³ [95]) or LiAl₅O₈ ($\rho = 3.6$ g/cm³ [120]) is rather unlikely because of the relatively large deviation of their densities to the refined value and the presence of a well-defined layer with low roughness.

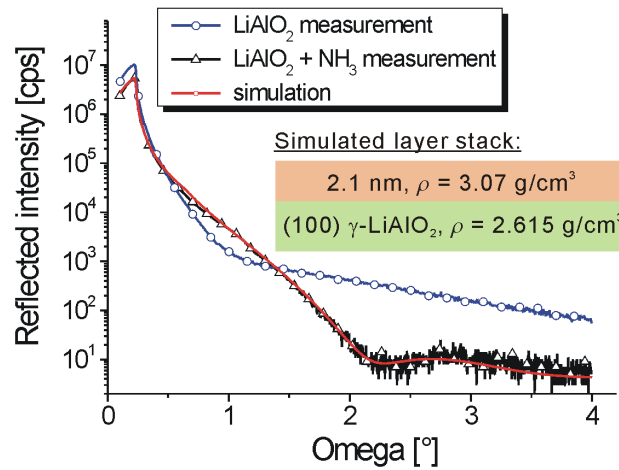


Figure 6.3: XRR spectra of both blank (open circles) and 5 min nitridated (open triangles) LiAlO₂ substrate. A simulation fit for a LiAlO₂/surface layer heterostructure (red curve) is also displayed.

The discrepancy between the simulated density and the one of AlN bulk material is not fully understood yet but a plausible explanation includes the incorporation of light impurity atoms into the AlN lattice. Indications for a lowered density in thin AlN films have also been found by Jokinen et al. and Zollner et al. [121, 122]. The latter group performed Rutherford backscattering experiments on MBE-grown AlN on Si(111) and found a density value of 3.0 g/cm³ for AlN. H and O atoms localized on defects were assumed as possible origin [122]. This was recently confirmed by

another report, which describes a significant lowering of the AlN density between 2.8 g/cm³ and 2.4 g/cm³ when the atomic H concentration is increased from 13% to 27% [123].

HRTEM was employed to support the XRR data and to address the important question of crystal orientation of the thin interlayer. In order to avoid electron beam-induced damaging of the LiAlO₂ substrate, the inspection was executed at low power excitation regime with an electron beam current density of around 3 pA/cm². The cross-section HRTEM image of a substrate exposed to NH₃ for 2 min is given in Figure 6.4. The zone axis vector denotes the direction perpendicular to the cross-section plane and is oriented along [010] of LiAlO₂ in this measurement.

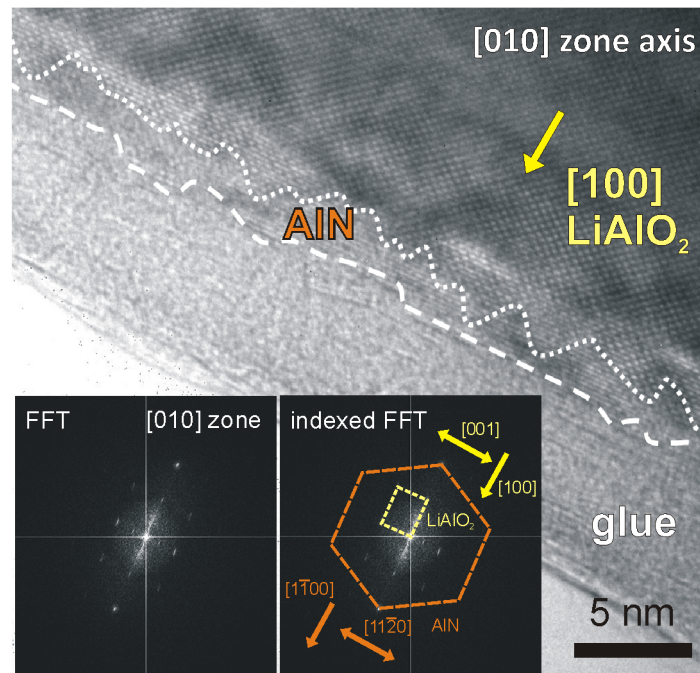


Figure 6.4: HRTEM image of the LiAlO₂ surface after 2 min exposure to NH₃ along the [010] zone axis. Material interfaces are marked by dashed lines. The insets show the FFT patterns with and without indication of the crystal unit cells and directions.

The fast Fourier-transformed (FFT) image in the inset clearly proves the presence of a hexagonal crystalline interlayer. An analysis of the diffraction pattern reveals an out-of-plane lattice constant of 0.259 nm. Considering this value and the orientation of

the FFT pattern, one can conclude that this crystal is (1 $\bar{1}$ 00) *m*-plane AlN. The in-plane epitaxial relationship is found to be $[0001]_{\text{AlN}} \parallel [010]_{\text{LiAlO}_2}$ and $[11\bar{2}0]_{\text{AlN}} \parallel [001]_{\text{LiAlO}_2}$. One should note that the nominal out-of plane lattice constant for *m*-plane AlN is 0.2695 nm. This corresponds to tensile strain in the investigated film, which can be very well expected due to the relatively large substrate-lattice mismatch for *m*-plane AlN on γ -LiAlO₂ of 3.7% and 0.9% in $[0001]_{\text{AlN}} \parallel [010]_{\text{LiAlO}_2}$ and $[11\bar{2}0]_{\text{AlN}} \parallel [001]_{\text{LiAlO}_2}$ direction, respectively. It is worth to mention that all prepared TEM specimens did not show any indication for a phase transformation of γ -LiAlO₂ into LiAl₅O₈. From Figure 6.4, it is hard to find an exact thickness value for the AlN layer due to a strong corrugation of the AlN-LiAlO₂ interface. This roughening is yet not fully understood but probably also a result of the damaging of the LiAlO₂ lattice during the TEM observation. However, one can take advantage of this poor stability and produce a hole in the substrate by persistent electron beam penetration. The result of such a process is shown in Figure 6.5 a).

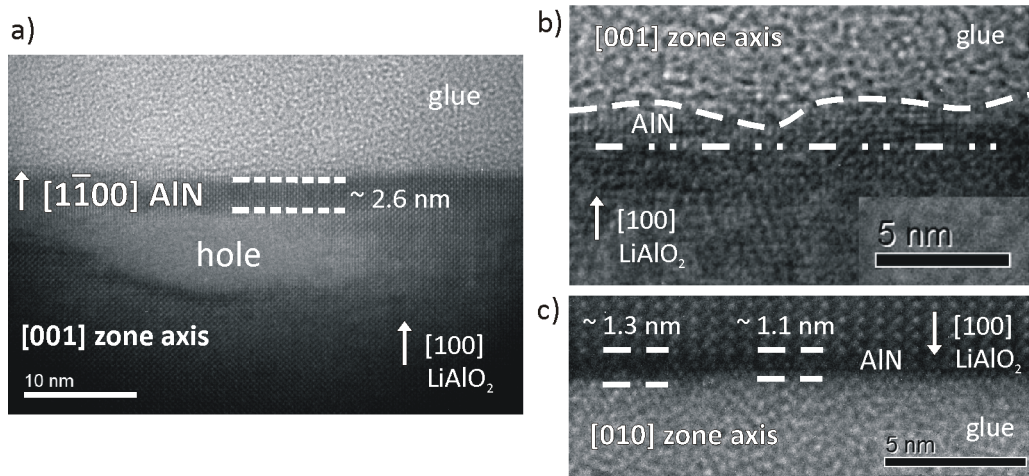


Figure 6.5: a) Cross-section HRTEM image of a 5 min nitridated LiAlO₂ surface after prolonged exposure to the electron beam shown along the [001] zone axis; b) and c) show the AlN/LiAlO₂ interface along the [001] and [010] zone, respectively. Material boundaries are schematically visualized.

One can see that during the prolonged observation time, a hole within the LiAlO₂ substrate has been burned in the thin specimen. As one may expect, the nitridation-

induced thin AlN film is stable enough to withstand this treatment. From such an image, a better determination of the thickness is possible. The extracted value of 2.6 nm is in relatively good agreement to the XRR results. Furthermore, a different surface quality along the two crystal directions is found. This phenomenon is illustrated in Figure 6.5 b) and c), which show cross-section TEM images for the $[001]_{\text{LiAlO}_2} \parallel [11\bar{2}0]_{\text{AlN}}$ (a) and $[010]_{\text{LiAlO}_2} \parallel [0001]_{\text{AlN}}$ (b) zone axis, respectively. The surface in the $[001]$ zone axis displayed in Figure 6.5 b) is dominated by a small-scale waviness, while for the other observation direction, it appears very smooth with small step-like features of ~ 0.2 nm height. Since the out-of-plane lattice constant of *m*-plane AlN was measured to be ~ 0.26 nm, it seems plausible that such steps correspond to one monolayer of *m*-plane AlN. The difference in surface roughness might be correlated to the anisotropic strain being present when the nitridation layer is formed. The process might be driven by lattice mismatch since the theoretical value of the anisotropic lattice mismatch along $[010]_{\text{LiAlO}_2} \parallel [0001]_{\text{AlN}}$ is much larger compared to the perpendicular direction. Such relaxation mechanism has also been reported for the nitridation of Al₂O₃ substrates, for which the formation of protrusions was observed [124]. A similar but anisotropic relaxation process might be responsible for the different surface characteristics observed for both directions. The physical origin of the different interface and surface qualities along the $[010]$ zone axis in Figure 6.4 and Figure 6.5 c) is yet unclear. It can be suspected that small variations in the TEM preparation process or the LiAlO₂ crystal quality itself are responsible. More experiments are required to answer this question with certainty.

As the main conclusion of this study, nitridation of LiAlO₂ leads to the formation of a few nm thin *m*-plane AlN interlayer, which is more stable against wet etching and electron beam irradiation.

6.3 Impact of nitridation on subsequent GaN epitaxy

With the knowledge of the processes on the substrate surface during nitridation, this section will now aim towards the question on the impact on GaN epitaxy. 300 nm thick GaN films were deposited in N₂ ambient after the NH₃ exposure, which was varied in duration from 0 s (no nitridation) to 300 s. The reactor pressure was kept at 300 mbar, and a V/III ratio of 1010 was chosen.

The effect of the nitridation step on the phase purity of the deposited *m*-plane GaN films is depicted in the HRXRD 2Theta/Omega scans in Figure 6.6 a). A shoulder on the left side of the LiAlO₂ peak indicates a small amount of *c*-plane GaN for the untreated sample (0 s NH₃). In the case of NH₃ exposure, no such shoulder but an increasing intensity for the *m*-plane GaN peak is observed.

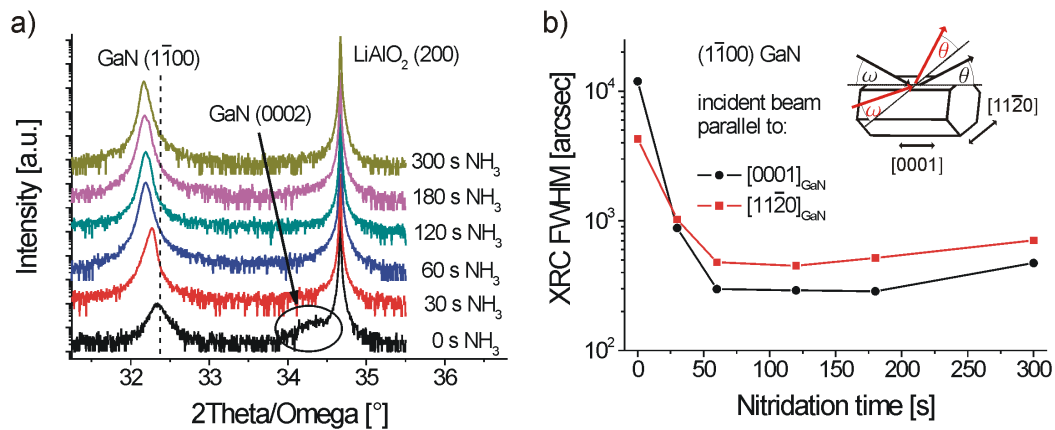


Figure 6.6: a) HRXRD 2Theta/Omega scans and b) XRC FWHM values for *m*-plane GaN films with different nitridation times. The dashed line in a) shows the nominal position of strain-free *m*-plane GaN. The illustration in the upper right corner of b) indicates the alignment of the probe beam with respect to the *m*-plane GaN crystal.

It is interesting to note that the GaN 2Theta peak position shifts from 32.34° (which is very close to its expected position at 32.39°) for the film without nitridation to 32.19° for all layers above 30 s NH₃ exposure. This is associated to a high out-of-plane tensile strain (and thus in-plane compressive strain), which has been reported for the growth of thin *m*-plane GaN films on LiAlO₂ by other groups before [17, 125]. The rising intensity of the GaN peak is also reflected in more narrow peak shapes in X-ray rocking curve (XRC) scans. The FWHM values of the peaks are shown in Figure 6.6 b) for incident beam directions parallel and perpendicular to the GaN *c*-axis. From this plot, a dramatic reduction of the peak widths after nitridation for both directions becomes visible. One finds smallest peak widths of 291 and 450 arcsec (for scans along the [0001] and [11̄20] direction, respectively) for a nitridation time of 120 s, while above this value, the situation is getting slightly worse again. This implies an

improvement in crystal perfection with an optimized nitridation process. Considering the anisotropy of the measured FWHM values, an inversion can be observed. The film without nitridation process shows higher FWHM when measured parallel to the GaN *c*-axis, while for nitridation times above 30 s, the situation is reversed. Altered in-plane growth rates, which affect the lateral extension of crystal domains and lead to an anisotropy of Omega peak widths may be responsible.

An identical trend of improved quality with longer nitridation times can also be seen by RT PL spectroscopy. The spectra of the layers with 0 and 300 s of NH₃ exposure are exemplarily given in Figure 6.7 a). It becomes apparent that for the sample without substrate pretreatment, almost no near band-edge emission is visible while the layer grown with nitridation shows some clear emission at 3.47 eV.

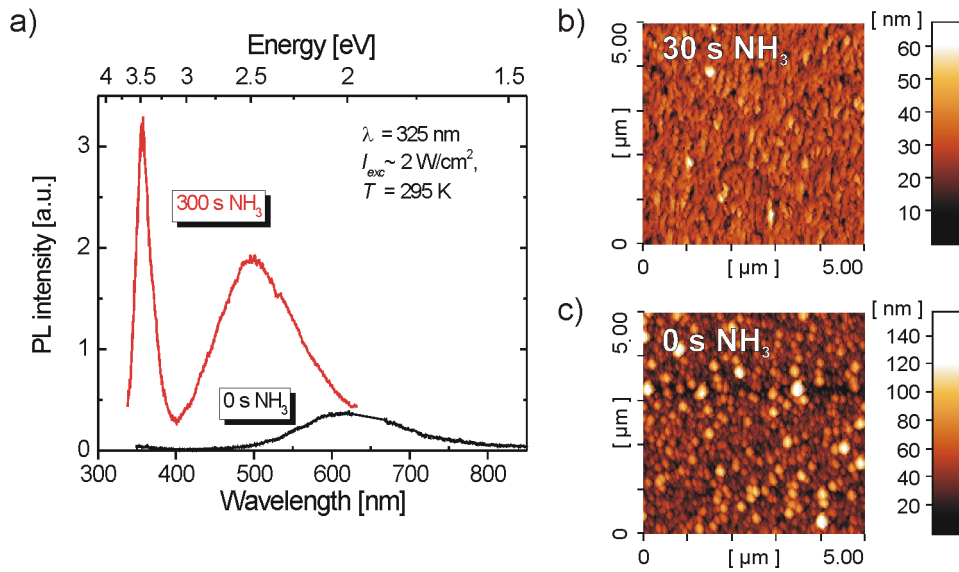


Figure 6.7: a) RT PL spectra and b-c) AFM scans for *m*-plane GaN layers with 0 s and 300 s nitridation step before growth.

The large energy value for a RT scan can be explained by considerable in-plane compressive strain in the phase-pure *m*-plane GaN films as already indicated in Figure 6.6. Beside of the GaN main peak, a probably defect-related signal at 2.5 eV is detected for all GaN films with nitridation step in Figure 6.7 a), which is similar to the commonly known yellow luminescence (YL) in *c*-plane GaN [126]. More

comments on this peak will be given in section 8. For the layer without nitridation step, the broad defect band is shifted to 2 eV. Furthermore, a significant improvement in layer quality with the nitridation process can be demonstrated regarding the surface morphology. This is visualized in Figure 6.7 b) and c). The average RMS roughness values decrease from about 20 nm to 6 nm after only 30 s of nitridation and remain almost constant for prolonged exposure to NH₃. Moreover, a transformation from a grainy, rough surface into a smoother one occurs. If no nitridation step is applied, lateral growth seems to be strongly suppressed. One may explain this behaviour by a damaging of the substrate during growth start, preventing the crystal nuclei from expanding horizontally. The lack of coalescence of the small grains allows an almost strain-free epitaxy of this mixed-phase GaN islands as found in Figure 6.6, whereas coalesced *m*-plane GaN films suffer from larger strain.

It is also interesting to note that the usage of a nitridation step even allows for the direct growth of *m*-plane GaN in H₂ ambient. Even though the quality of such layers is slightly inferior to layers deposited in N₂, which can be explained by partial substrate damaging, it clearly underlines the enhanced stability of the nitridated substrate.

As a main conclusion of this study, sufficient nitridation is surely necessary to protect the substrate surface and obtain smooth, phase-pure *m*-plane GaN films with high crystal quality. So far only thin GaN films have been deposited to investigate the effect of substrate pretreatment. In the following, thicker *m*-plane GaN films will be grown to study the crystal structure and layer properties in detail.

7 Anisotropic crystal properties of *m*-plane GaN films on LiAlO₂

This chapter comprises a structural, morphological, electrical and optical investigation of thicker *m*-plane GaN films on LiAlO₂ substrates. Special attention is dedicated to the film anisotropy. First, the epitaxial process for the deposition of thicker GaN films is described. After that, layer properties like surface morphology, crystalline structure as well as optical and electrical characteristics are discussed.

7.1 Three-step growth technique for thick GaN film deposition

Based on a previously developed growth process, a three-step growth procedure was chosen to deposit GaN films with thicknesses between ~ 70 nm and ~ 1.7 μ m [127]. The standard growth process and layer structure are schematically depicted in Figure 7.1 a) and b), respectively. It comprises a nitridation step with duration of 2, 5, or 8 min. In case of 2 and 5 min nitridation (“N” in Figure 7.1), the NH₃ flow is switched on after reaching the growth temperature of 890 °C. For 8 min nitridation time, NH₃ is already introduced during the 3 min temperature ramp-up starting at 500 °C. After the growth temperature is reached, another 5 min of nitridation is performed. The nitridation is followed by the deposition of an initial sealing layer in N₂ ambient (“S”), and the subsequent growth in H₂ atmosphere (“G”). H₂ as carrier gas is known to be beneficial for GaN deposition because it helps to reduce the number of newly formed GaN nuclei, which can lower the total edge-type dislocation density [128]. However, a direct nucleation of GaN in H₂ ambient after nitridation yields lower quality, which is probably because of partial substrate degradation as already mentioned in chapter 6. A ~ 70 nm thick GaN film grown in N₂ was found suitable to achieve good surface morphology and low XRC peak widths. The deposition in H₂ ambient was carried out at a slightly higher reactor temperature of 900 °C. The TMGa flux was set to 86 μ mol/min and the reactor pressure was kept at

300 mbar during all steps. If not further specified, an NH₃ flow rate of 89 mmol/min was chosen. These values correspond to a V/III ratio of 1010.

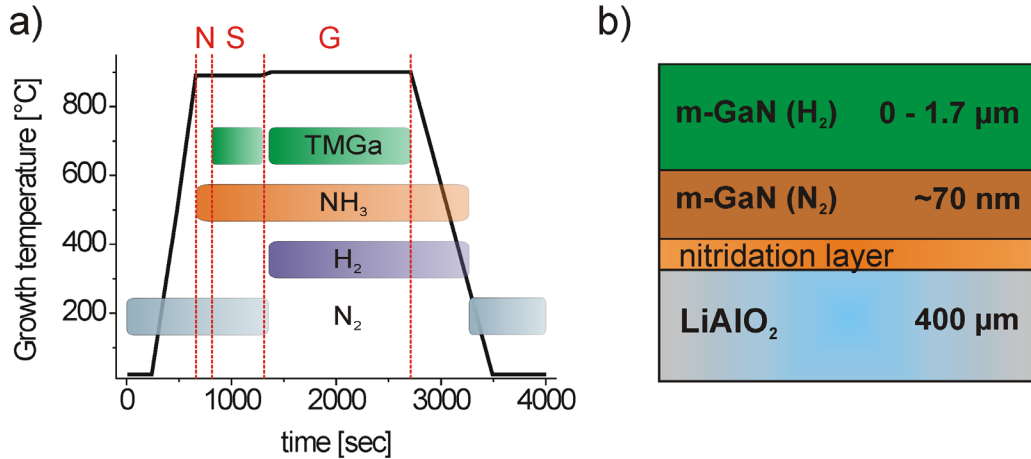


Figure 7.1: a) Standard deposition process for *m*-plane GaN films using the 3-step technique including nitridation (N), sealing layer (S), and main layer growth (G).
b) Resulting layer stack.

The *in situ* measured surface temperature and reflectivity for a 1.7 μm thick *m*-plane GaN film on LiAlO₂ with 2 min nitridation time is exemplarily displayed in Figure 7.2 a). The surface temperature is only accessible above ~600 °C. The small temperature drop after the deposition of the N₂-GaN layer is due to the switching of carrier gas. Two wavelengths are displayed to monitor growth rate and surface roughness. The signal taken at 605 nm shows distinctly damped oscillations, which may be caused by sub-bandgap absorption in the GaN film. The probable origin is an incorporation of impurities, a topic which will be discussed in detail in chapter 8. The reflectivity at 349 nm shows a decline during deposition. This can be explained by an increased surface roughness. If NH₃ is already introduced during the temperature ramping step at 500 °C, distinct changes become visible in the *in situ* reflectivity data. This is demonstrated in Figure 7.2 b) for the case of a 0.9 μm thick *m*-plane GaN film, which was deposited after 8 min nitridation time. The initial amplitude for the reflectivity values is reaching lower values compared to Figure 7.2 a), but in contrast,

less contraction with growth time occurs for the signal at 605 nm. Also, the reflectivity at 349 nm is almost constant.

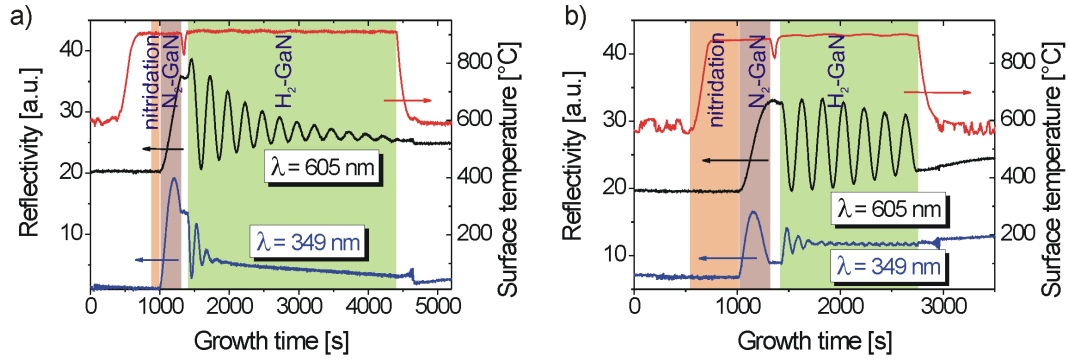


Figure 7.2: Surface temperature and reflectivity of *m*-plane GaN films grown with a) 2 min nitridation step at 890 °C and b) 8 min nitridation step starting at 500 °C.

Reflectivity datasets are vertically shifted for clarity.

These effects may be explained by less absorption and surface roughening during growth and indicate superior quality of the deposited *m*-plane GaN film starting nitridation already at low temperature (LT). One may explain this effect by less damage being introduced into the substrate when the AlN nitridation layer is formed at decreased temperature.

7.2 Surface features of *m*-plane GaN films on LiAlO₂

7.2.1 Morphology of optimized GaN films

This chapter will discuss properties related to the surface quality of *m*-plane GaN films. If not further specified, all data stem from the 900 nm thick layer grown by an optimized deposition process using NH₃ exposure during temperature ramping with a total nitridation time of 8 min.

Two AFM images for large ($50 \cdot 50 \mu\text{m}^2$) and small ($2 \cdot 2 \mu\text{m}^2$) area scans are given in Figure 7.3 a) and b), respectively. The in-plane crystal directions have been

determined by XRD and are depicted as well. The larger-area scan in Figure 7.3 a) is dominated by huge rhombically shaped hillocks, elongated along the $[11\bar{2}0]$ direction. A similar pyramidal macroscopic undulation with comparable inclination angles along both in-plane axes was also reported for the homoepitaxy of *m*-plane GaN films on bulk substrates [129]. In this report, it has also been demonstrated that the usage of slightly off-oriented substrates can eliminate this roughening. The effect was explained by Farrell et al., who showed that a dislocation with a screw-component at the apex of the pyramid leads to spiral growth and is thus responsible for the special morphology [130].

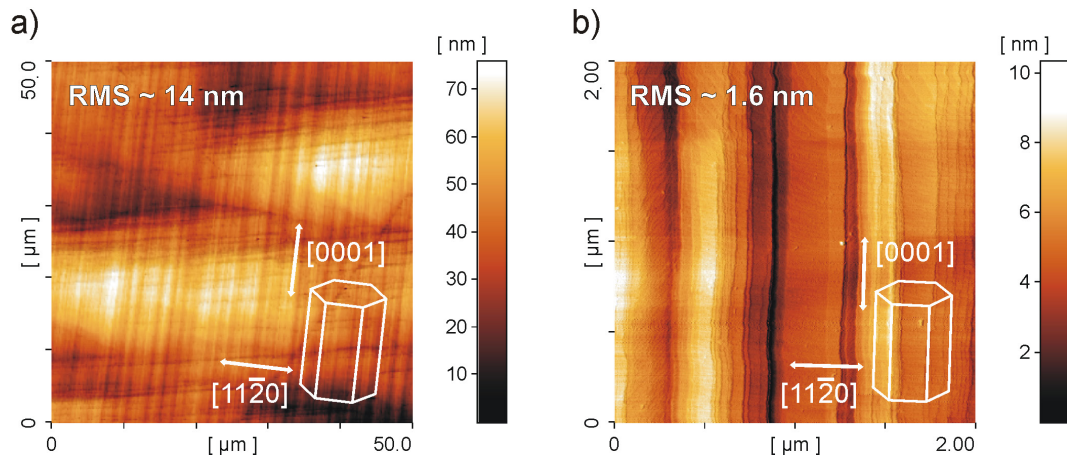


Figure 7.3: AFM images of *m*-plane GaN surface using a scan area of a) $50 \cdot 50 \mu\text{m}^2$ and b) $2 \cdot 2 \mu\text{m}^2$. The crystal directions are schematically visualized.

A similar mechanism is assumed to cause the macroscopic features in the *m*-plane GaN films on LiAlO₂. As a second apparent surface characteristic, parallel lines running along the $[0001]$ direction can be observed. The AFM scan performed on a smaller area shown in Figure 7.3 b) highlights this finding. The lines are basically stripes of material with the same surface level running parallel to the GaN *c*-axis direction. They are separated by steps of typically 1-2 nm height and an average line density of $6 \cdot 10^4 \text{ cm}^{-1}$. Usually, stripe-like surface undulations in *m*-plane GaN films are aligned in the $[11\bar{2}0]$ direction [17, 35, 92, 131-133]. However, Raman spectroscopy confirms that in the case of MOVPE-grown films on LiAlO₂, the stripe orientation is along $[0001]$, details of this study are described elsewhere [134]. The striated

surface pattern is present also for slightly changed nitridation conditions, growth temperature, and V/III ratio. Yet, if the thickness of the deposited film is 200 nm or below, only a hillock-dominated surface without stripes can be seen. An unfinished coalescence process or altered strain state may be seen as possible reason for this change. The strain state of the films will be discussed in section 7.3.1.

A likely explanation for the special morphology with stripes along [0001] is a strongly anisotropic diffusion of species on the growing surface. Anisotropic adatom diffusion barriers have been theoretically predicted both for *a*-plane and *m*-plane GaN surfaces [56, 135]. These calculation are in agreement with the experimentally observed striated surface along the GaN *c*-axis for *a*-plane films on *r*-plane sapphire [86]. In contrast, for *m*-plane surfaces, lower diffusion barriers and thus higher lateral growth rate along the $[11\bar{2}0]$ direction corresponding to a stripe formation along $[11\bar{2}0]$ are expected [56, 135]. However, if anisotropic strain is involved, the situation may be reversed due to the strong impact of lattice compression on the lateral growth mode [136, 137]. The lattice mismatch values for both AlN and GaN on LiAlO₂ are highly anisotropic. Since the AlN interlayer was found to be tensile strained (compare section 6.2) and the GaN films exhibit compressive strain (compare section 6.3), some contribution to the in-plane diffusion barrier heights may well be expected. It should be mentioned that Hoshi et al. also reported on a striated surface pattern along [0001] direction for their *m*-plane GaN films homoepitaxially deposited by NH₃-source MBE but blamed inappropriate surface preparation to be responsible [138]. The surface stripe orientation of *m*-plane GaN layers is thus presumably influenced by many factors and may be modified by slight changes in strain and surface condition caused by an altered deposition process or substrate pretreatment.

Taking a closer look at the morphology between the steps in Figure 7.3 b), one can recognize a much smoother surface with a local RMS roughness of ~ 0.2 nm in an area with dimensions of $0.4 \cdot 0.4 \mu\text{m}^2$. The only visible feature here is a step-flow surface pattern with average step height of around 0.27 nm. This is in good agreement to the out-of-plane lattice constant of *m*-plane GaN, which amounts to 0.276 nm, and thus corresponds to one monolayer. While step-terrace surfaces are common for high-quality *c*-plane GaN films, they are rarely observed for the typically highly dislocated nonpolar layers. Monolayer atomic steps have been reported for *m*-plane GaN homoepitaxy [139]. The few reports on the achievement of step-flow growth mode in

nonpolar heteroepitaxy are restricted to the nearly defect-free wing regions of films grown by sidewall ELOG technique [45, 92, 93]. The observation of step-flow surface morphology was reproducibly found even for slightly modified deposition parameters and thus provides evidence for a relatively low defect density of *m*-plane GaN films grown on LiAlO₂ substrates using the 3-step MOVPE technique.

7.2.2 Effect of V/III ratio on surface morphology

The described anisotropic surface features (hillocks, striation) are generally observed for a wide range of deposition and substrate pretreatment conditions. However, a noticeable change in surface morphology was found for altered V/III molar flux ratios during H₂-GaN deposition. The investigated films have a thickness of 1.4 μm and have been grown after a 2 min nitridation step at 890 $^{\circ}\text{C}$. V/III molar flux ratio was varied between 505 and 2020 by changing the NH₃ flux from 44 mmol/min to 178 mmol/min. Figure 7.4 a) and b) exemplarily depict two AFM images for *m*-plane GaN films grown with V/III ratios of 1010 and 2020, respectively.

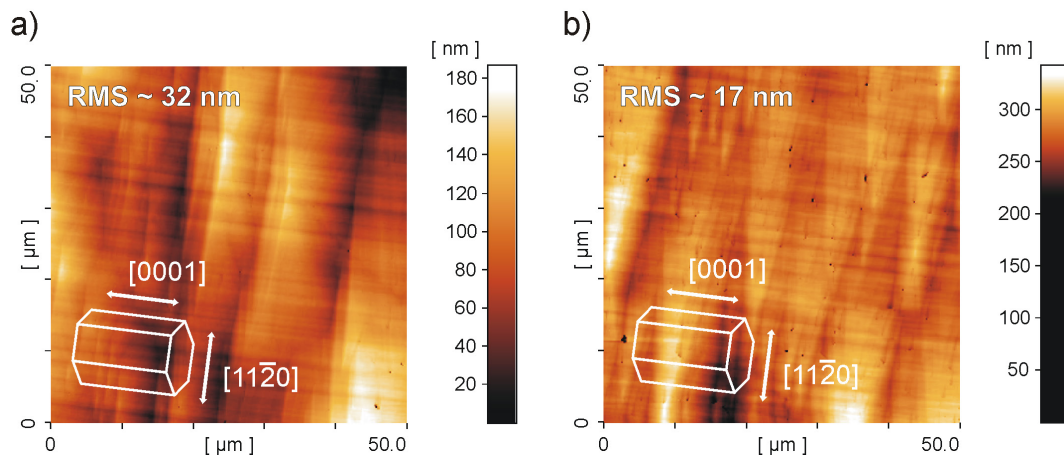


Figure 7.4: AFM images of *m*-plane GaN films grown with a V/III ratio of a) 1010 and b) 2020. The crystal directions are schematically visualized.

Similar to the previously described optimized film, the surface in Figure 7.4 a) exhibits a tiled appearance but with larger hillocks. In contrast, smaller triangular features show up in Figure 7.4 b). This results in a decrease of the RMS roughness

from 37 nm to 17 nm when the V/III ratio is increased from 505 to 2020. The striated pattern is visible in both cases without significant changes of the stripe density. Unlike in Figure 7.3, a few small holes are additionally observed in Figure 7.4 a) and, to a higher extend, in Figure 7.4 b). For layers with 2 min nitridation step, their density is typically in the order of 10^6 cm^{-2} for a V/III ratio of 1010 and increases up to 10^7 cm^{-2} at the largest V/III ratio of 2020. These holes can be enlarged by a short wet etching step in H_3PO_4 at 160 °C for 1 - 2 min. As a result, the holes take a rectangular shape indicating a higher etch rate along the GaN *c*-axis. Since V/III ratio is known to influence the growth rate of different facets of the GaN crystal [88], a reduced lateral growth rate is thought to be responsible for the generation of these holes. The change in lateral growth rate probably causes also the altered hillock pattern. However, an optimized growth procedure using 8 min nitridation starting at 500 °C yields only negligible hole densities on the surface, so the holes are obviously also related to the substrate pretreatment and may very well be initiated by defects, which are generated at an initial growth stage. One may even speculate that a damaged substrate surface causes single crystallites of *m*-plane GaN to nucleate on the O-sub-lattice of LiAlO₂ (compare Figure 4.1), which thus inhibits the local coalescence to the neighbouring crystal.

The demonstrated results show that *m*-plane GaN films on LiAlO₂ suffer from a large roughness on a macroscopic scale, which can probably be overcome by the usage of miscut or less defected LiAlO₂ substrates. Looking on a microscopic scale, the optimized *m*-plane GaN films exhibit a striated pattern due to the in-plane anisotropy during epitaxy. Between these stripes, the surface is perfectly smooth, which may be seen as an indication for high crystal quality. The following chapter will further elucidate the structural quality of the crystal.

7.3 Structural properties of *m*-plane GaN films on LiAlO₂

7.3.1 Defect and strain characterization by XRD

Results regarding defect structure and strain of the *m*-plane GaN films will be presented in the following. XRC Omega scans using a 1 mm detector slit were taken

with the incident X-ray beam along the two in-plane crystallographic axes to detect the structural layer anisotropy, which may be caused by planar defects like BSF [140, 141]. The scans performed on the symmetric ($1\bar{1}00$) GaN reflection are displayed for the optimized 0.9 μm thick *m*-plane GaN film in Figure 7.5. Beside the main peak, both curves also exhibit a shoulder or a small peak at 17.7° , which are caused by the (200) reflection of the LiAlO₂ substrate. The logarithmic scale plot shows a very low FWHM peak width of $224''$ along the GaN *c*-axis and a much broader curve with an FWHM of $1832''$ in perpendicular direction. The strongly anisotropic peak broadening is likely related to the special anisotropic growth mode, which results in the above described striated morphology.

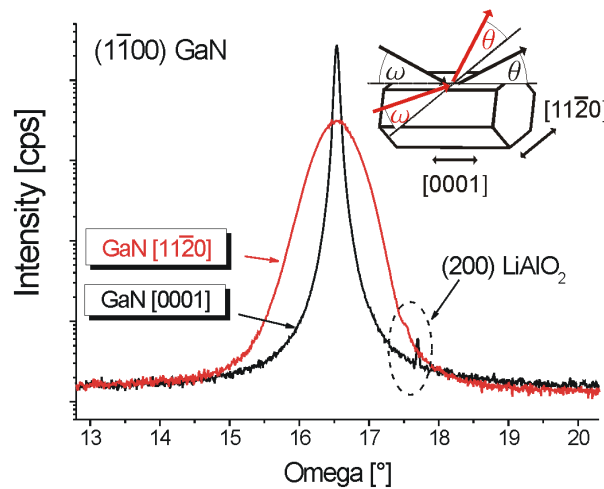


Figure 7.5: Symmetric ($1\bar{1}00$) XRC spectra of a 0.9 μm thick *m*-plane GaN film for two incident X-ray beam directions. The illustration in the upper right corner indicates the alignment of the probe beam with respect to the *m*-plane GaN crystal.

The coherent growth of elongated stripes along [0001] is expected to result in a narrow peak shape. In contrast, the large number of boundaries along the perpendicular $[11\bar{2}0]$ axis causes strong XRC peak broadening. To quantify this effect, both LCL and mosaic tilt $\Delta\omega_{mos}$ have been determined. This analysis excludes the Omega peak width for the GaN ($3\bar{3}00$) reflection taken parallel to the [0001] direction of GaN because of non-negligible superposition with an unidentified other peak. The

data are summarized in Table 7.1. Low and high tilt angles in $[0001]$ and $[11\bar{2}0]$ direction are extracted, respectively. Furthermore, an extremely large LCL is found parallel to the GaN *c*-axis while the perpendicular direction exhibits a much lower value. It is important to note that a reliable determination of LCL values above 1 μm is not possible due to the limited accuracy of this method. Thus, one can only state that the dominating broadening effect for the measurement along $[0001]$ is not caused by a limited lateral microcrystalline coherence but by crystalline tilt. The LCL for the scanning direction along $[11\bar{2}0]$ is quite reasonable and reflects the mean spacing of the stripe features on the surface (compare Figure 7.3).

*Table 7.1: XRC FWHM, $\Delta\omega_{\text{mos}}$, and LCL for a 0.9 μm thick *m*-plane GaN film on LiAlO₂ with 8 min nitridation time measured along both in-plane crystal directions.*

		XRC FWHM GaN			calculated	calculated
		$(1\bar{1}00)$	$(2\bar{2}00)$	$(3\bar{3}00)$	$\Delta\omega_{\text{mos}}$	LCL
\parallel	<i>c</i> -axis	306''	305''	(416'')	305''	50 μm
\perp	<i>c</i> -axis	2526''	2446''	2387''	2318''	254 nm

McLaurin et al. proposed to use the LCL in *c*-axis direction for the calculation of the BSF density [141]. If BSF are the dominating defect types in the film, this assumption is valid since the LCL expresses the average extension of an undistorted crystal region. Due to a lack of sensitivity of the $(3\bar{3}00)$ reflection to BSF [142], the LCL should be calculated without using this peak width, which was not evaluated in our study anyway. The LCL of 50 μm can be translated into a BSF density of $2 \cdot 10^2 \text{ cm}^{-1}$. The lower detection limit of the method is around $1 \cdot 10^4 \text{ cm}^{-1}$, which can thus be regarded as an upper limit for the BSF density of the optimized *m*-plane GaN films.

Moram et al. pointed out that the quantification of BSF densities using XRD cannot be used for accurate determination because the surface morphology may have an impact on the peak widths as well [142]. Instead, they suggested to use a rough estimation for the BSF number by comparing the $(2\bar{2}00)$ and $(3\bar{3}00)$ reciprocal lattice points (RLP) [143]. The enhancement of intensity on the far-angle wing along the Q_x coordinate in the $(2\bar{2}00)$ RLP is caused by diffuse scattering on BSF and may

thus be analyzed for an approximate BSF quantification. Since the $(3\bar{3}00)$ reflection is not affected by BSF, one can use this peak shape as a reference. Moram et al. ascribed clearly visible streaking to BSF densities above $3 \cdot 10^5 \text{ cm}^{-1}$ in *a*-plane GaN. Reciprocal space maps for both reflections are shown in Figure 7.6 a) for the optimized *m*-plane GaN film on LiAlO₂. Both RLP appear very sharp with very little broadening along Q_X . A pronounced diffuse streaking of the $(2\bar{2}00)$ RLP compared to the $(3\bar{3}00)$ RLP in the Q_X range of ± 0.05 as seen by Moram et al. cannot be observed. The absence of an enhanced intensity by diffuse scattering in this range is also illustrated in Figure 7.6 b), which shows the extracted Q_X scans at the peaks of the RLP. In view of this situation and of the previously described XRD results, one can estimate that the *m*-plane GaN films investigated in this study exhibit BSF densities, which are clearly lower than 10^5 cm^{-1} .

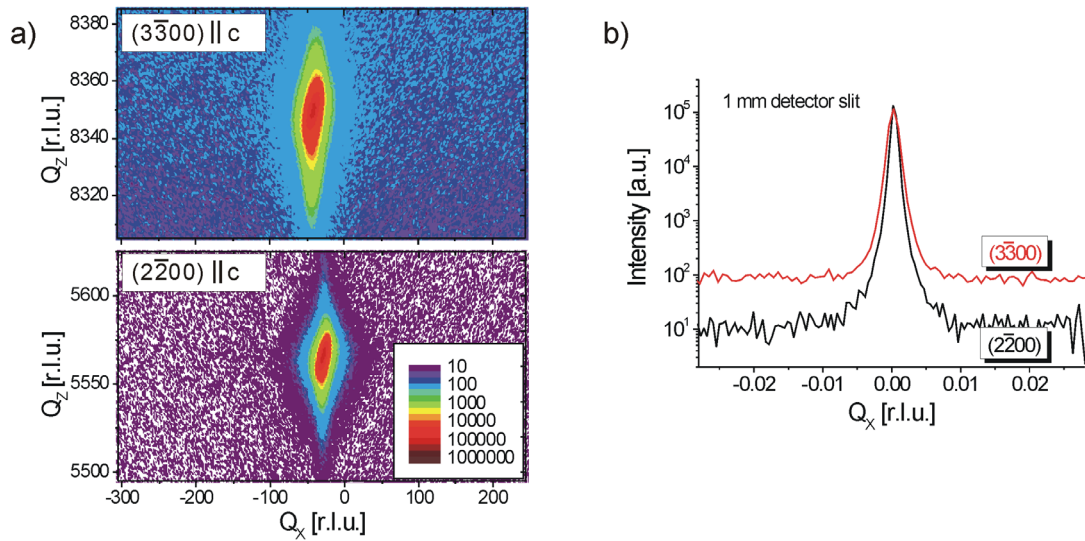


Figure 7.6: a) XRD reciprocal space maps of a $0.9 \mu\text{m}$ thick *m*-plane GaN film for the $(2\bar{2}00)$ and $(3\bar{3}00)$ reflection measured with incident beam direction coplanar to $[0001]$. b) Extracted Q_X scans at the peak maximum.

To obtain more information on the development of the special crystalline microstructure during epitaxy, several samples with different thicknesses between 70 nm and

1.7 μm were grown and characterized using HRXRD. All films comprise a 2 min nitridation step. The XRC peak widths for various layer thicknesses and two incident beam directions are depicted in Figure 7.7 a). For very thin layers, only little or no peak width anisotropy is present with FWHM as low as $\sim 200''$. In contrast, when the film thickness reaches $\sim 0.9 \mu\text{m}$, much broader peak widths are found for the $[11\bar{2}0]$ measurement direction. For even thicker films, the FWHM in this direction is slightly reduced again while a weak increase is found for the FWHM values measured along $[0001]$.

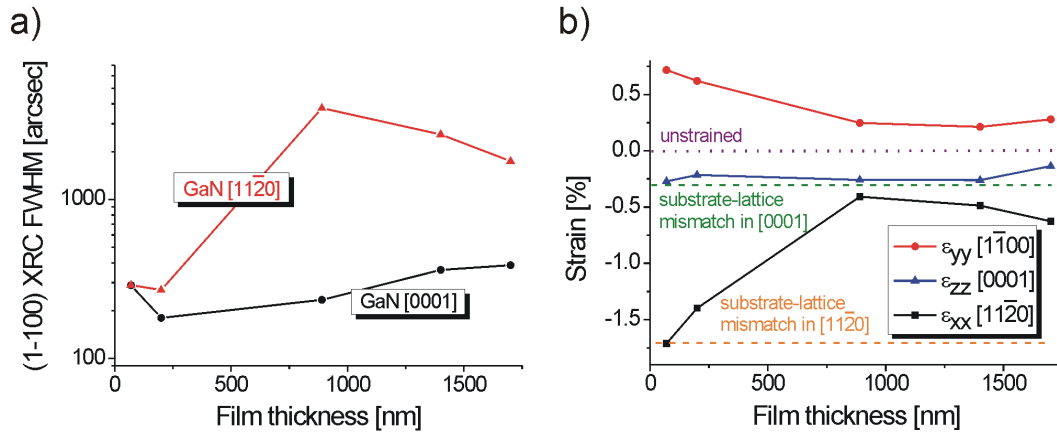


Figure 7.7: a) Symmetric $(1\bar{1}00)$ GaN XRC FWHM along two incident beam directions and b) measured strain in m -plane GaN films for different film thicknesses.

To gain a better understanding of the underlying physical mechanisms, the strain in the m -plane GaN films was also investigated. To allow for a calculation of the in-plane strain values, asymmetric HRXRD scans on lattice planes, which are tilted either towards the (0001) or $(11\bar{2}0)$ plane, were performed. For the nomenclature of strain values, the a -axis, m -axis, and c -axis direction are represented by x , y , and z , respectively, as already introduced in Figure 2.1. The dependency of the in-plane (ϵ_{xx} , ϵ_{zz}) and out-of plane (ϵ_{yy}) strain against thickness is plotted in Figure 7.7 b).

These data contain some deviations since asymmetric plane reflections typically exhibit low intensity due to weak scattering efficiency. However, one still can extract valuable information. In $[0001]$ direction, a comparably small compressive strain

component is present, which is obviously mainly defined by the initial substrate-lattice mismatch and appears to be nearly unchanged with film thickness. In contrast to that, the lattice deviation in $[11\bar{2}0]$ is much larger for thin films and exhibits a gradual decrease for thicker layers. It is interesting to note that even the 1.7 μm thick film does not show full relaxation. Quite surprising is the fact that the measured value of -1.7% for the 70 nm film is in such a good agreement to the substrate-lattice mismatch. One should also keep in mind that this is a huge value for any epitaxial system. It may be argued that the large strain can only be maintained because of the lack of a suitable glide plane. The absence of such glide plane prevents effective relaxation by defect introduction. The out-of-plane tensile strain in $[1\bar{1}00]$ direction is a result of the two in-plane compressive strain components and decreases for thicker layers.

A final note should be made on thermal expansion. The mismatch of the thermal expansion coefficients for *m*-plane GaN and LiAlO₂ is highest along the $[11\bar{2}0]_{\text{GaN}} \parallel [001]_{\text{LiAlO}_2}$ direction, where the thermal expansion of LiAlO₂ is roughly three times larger than the value for GaN. This decreases the nominal substrate-lattice mismatch along this direction from -1.7% to -0.8%. Assuming coherent growth without any formation of misfit dislocations, the layers would be strongly compressed along the GaN *a*-axis during cool-down. This indicates that a large fraction of the strain is induced after growth. Since compressively strained films are less inclined to cracking, all layers up to 1.7 μm thickness are still intact. However, cracking and delamination of the GaN thin film was observed for layer thicknesses above 1.9 μm .

Combining the results on strain state and the XRC peak widths, one can state that a relaxation process takes place for film thicknesses above 200 nm, which decreases the high in-plane strain along the GaN *a*-axis. This is accompanied by larger XRC peak widths especially in *a*-direction, obviously caused by mosaic tilt. In view of the appearance of the striated morphology for films thicker than 200 nm, one may conclude that the special anisotropic growth mode is probably also helpful to relax the huge initial strain caused by substrate-lattice mismatch along the GaN $[11\bar{2}0]$ direction. Besides, it is worth to note that the strain within the GaN layers can be slightly altered by changing the V/III ratio. Increasing this ratio in the H₂-GaN layer from 505 to 2020 lowers the out-of-plane strain component in a 1.4 μm thick film from 0.26% to 0.19%. The different growth mode, which is accompanied by a higher

generated pit density and smaller hillocks as displayed in Figure 7.4, can possibly be blamed for this effect.

7.3.2 TEM investigation of crystal microstructure

TEM provides a good insight into the present defect types and densities within the GaN film. Due to the brittle nature of the LiAlO₂ material and the large strain between substrate and deposited film, only a small number of high-quality cross-section images could be obtained. All data discussed in this section were collected from a $\sim 1.4 \mu\text{m}$ thick *m*-plane GaN film grown after 2 min nitridation. Figure 7.8 shows two dark-field TEM images taken along a cross-section of the $[11\bar{2}0]$ zone axis with different diffraction *g* vectors. In Figure 7.8 a), a very distorted region close to the LiAlO₂ substrate can be seen, which does not allow any defect identification.

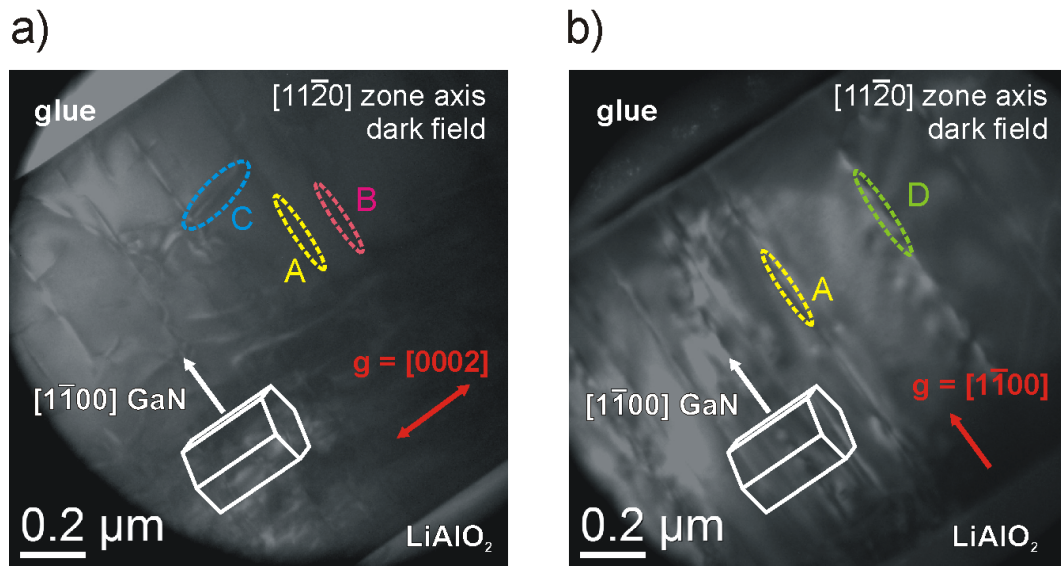


Figure 7.8: TEM cross-section images of a $1.4 \mu\text{m}$ GaN film on LiAlO₂ taken along the $[11\bar{2}0]$ zone using dark-field conditions. The diffraction vector *g* was chosen as a) $[0002]$ and b) $[1\bar{1}00]$. Distinguished defect types are marked.

After 400 - 500 nm, the structural quality is found strongly improved. Here, several lines aligned parallel to $[1\bar{1}00]$ and only a few inclined lines are in contrast. When

aligning the g vector parallel to the growth direction as displayed in Figure 7.8 b), less distortion within the GaN film close to the substrate but overall more dislocation lines intersecting the whole GaN layer become apparent. According to the $g \cdot b$ visibility criterion, one can distinguish four defect types labelled as ‘A’, ‘B’, ‘C’, and ‘D’. Defects marked as ‘A’ are visible in both images and can therefore be identified as Frank partial dislocation. One can find in total four of these defects in the given images. ‘B’ and ‘C’ are only observed for $g = [0002]$ and are probably of edge-type and mixed-type character, respectively. Defect ‘D’ is in contrast for $g = [1\bar{1}00]$ only and also seen four times here. The viewing conditions allow an identification as either Frank-Shockley partial or stair-rod dislocation. An interesting remark can be made about the observed density of Frank partial dislocations. As discussed in chapter 3.1.1, these defects are bound to I₁- or E-type BSF. The latter type is rarely observed in nonpolar films and can probably be neglected here. As a consequence, one can estimate the local I₁-BSF density via the mean separation of Frank partials to $4.7 \cdot 10^4 \text{ cm}^{-1}$. This value is somewhat higher compared to the upper limit of 10^4 cm^{-1} found by XRD, which can be understood by taking into account the greatly different volumes of characterization for both techniques.

TEM images with cross-section along the $[0001]$ zone are displayed in Figure 7.9 showing quite a different defect distribution. Figure 7.9 a) is taken under dark-field conditions with g parallel to $[1\bar{1}00]$ while for Figure 7.9 b), a g vector of $[11\bar{2}0]$ was chosen. Again, some lines running parallel to the growth direction are found and named as ‘E’ and ‘F’, respectively. Since both images do not show exactly the same sample area, it is not possible to unambiguously define the character of these defects. It is only possible to state that ‘E’ is either a screw-type TD, a Frank partial TD, or a stair-rod dislocation. For defect ‘F’, the screw-type character can be excluded. In addition, dislocation lines being 60° inclined with respect to the surface are in contrast for both g vectors. These lines marked as ‘G’ with propagation direction l of $[1\bar{2}10]$ or $[2\bar{1}\bar{1}0]$ originate at the substrate-film interface and penetrate the whole layer. Their character can be interpreted as either pure screw-type or mixed-type. Lo et al. also identified defects running at a 60° angle using TEM cross-section images in the $[0001]$ zone axis of MBE-grown *m*-plane GaN films on LiAlO₂ [144]. They connected these lines to PSF, which are associated with mixed-type TD. The PSF

were thought to be generated during the coalescence of islands leaving a 60° grain boundary angle in between.

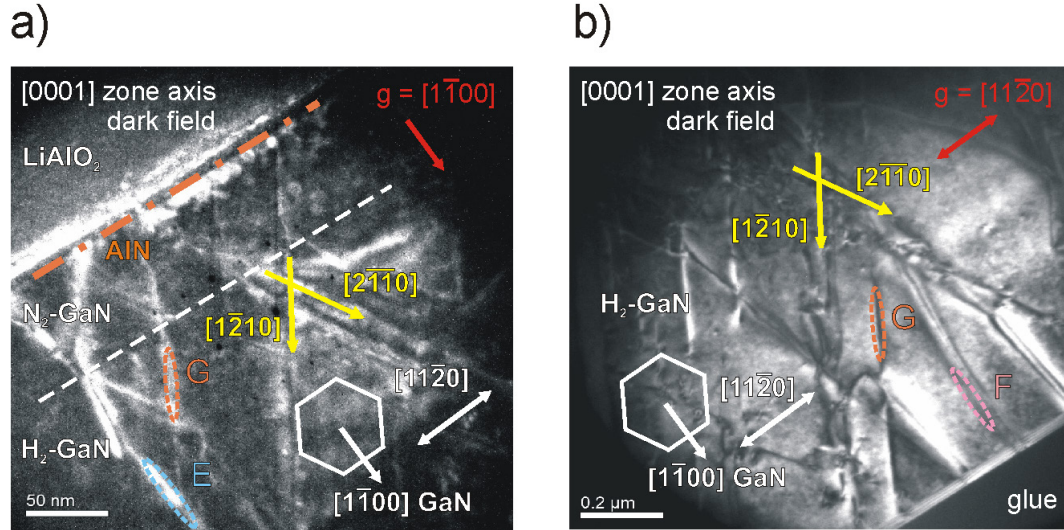


Figure 7.9: TEM cross-section images of a 1.4 μm GaN film on LiAlO₂ taken along the [0001] zone using dark-field conditions. The diffraction vector g was chosen as a) $[1\bar{1}00]$ and b) $[11\bar{2}0]$. Distinguished defect types are marked.

In this context, it is also interesting to mention a study on MOVPE-grown *m*-plane GaN on LiAlO₂ revealing similar 60° tilted defects in cross-section TEM [40]. This group also showed a network of planar defects in plan-view TEM images. Some of these defects appear to be located on the 60° inclined $(10\bar{1}0)$ prismatic plane while others are located on differently tilted planes [40]. A probable connection to coalescence boundaries was speculated on. In addition to that, zigzag-shaped structures composed of such planar defects were identified in cross-section images and were seen as one origin for the generation of BSF during film growth [40]. XRC FWHM values with the incident beam parallel to [0001] increasing with sample thickness were seen as confirmation for this theory. However, an erroneous determination of the X-ray incident beam direction with respect to the sample orientation makes their interpretation of BSF generation at the defects on the prismatic planes questionable [40].

The overall structural quality found in this TEM study appears to be reasonable given the fact that large defect-free areas between single dislocations are observed in the cross-section. Still, exact BSF and TD area densities cannot be specified since the preparation of plan-view TEM specimens was impossible within this study, which is due to the brittle substrate and the large strain within the GaN layers.

7.3.3 Defects revealed by Electron Channelling Contrast Imaging (ECCI)

The ECCI technique is an alternative route to assess TD area densities. Crystalline defects produce a lattice distortion, which gives rise to contrast in plan-view surface images produced by scattered channelling electrons, therefore also allowing a quantitative determination [115]. Figure 7.10 depicts such an image taken from a 0.9 μm thick GaN film with 5 min nitridation step. Beside of the typical stripe features, black dots are in contrast representing TD with a density of $\sim 1 \cdot 10^9 \text{ cm}^{-2}$.

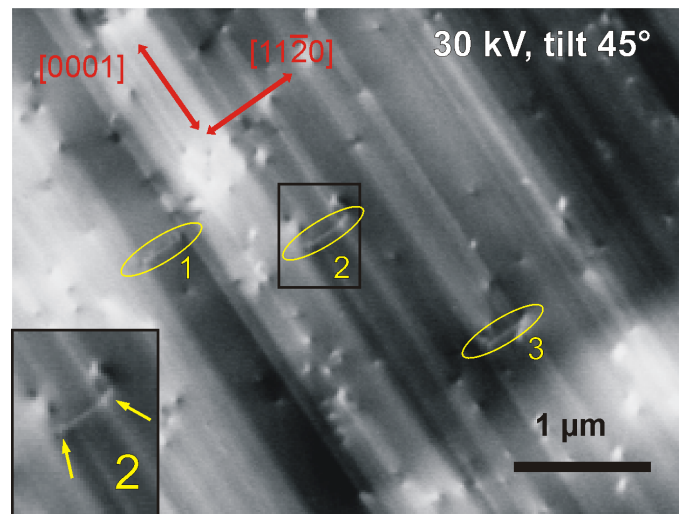


Figure 7.10: ECCI from a 0.9 μm thick m-plane GaN film using 5 min nitridation. Yellow circles mark the position of BSF. The magnification in the lower left corner highlights the surrounding partial dislocations.

One can find that these defects are not homogeneously distributed and leave large areas of quasi-dislocation-free material in between. The dislocation type cannot be determined at present. Beside of line defects, BSF are also in contrast under these

viewing conditions. This is the first report about the visibility of BSF in nonpolar GaN films using ECCI. The contrast mechanism is not fully understood but it can be assumed that altered surface strain is responsible for the contrast. The BSF appear as lines along $[11\bar{2}0]$ with a length of roughly 300 nm. Taking a closer look, one can also recognize line defects at the edge of each BSF. They can clearly be interpreted as surrounding partial dislocations of either Frank- or Frank-Shockley-type. Counting the visible BSF in several images yields an area density of $7 \cdot 10^7 \text{ cm}^{-2}$. Although the specification of BSF densities per unit area is straightforward and exact, it is not a common way to notify these densities in literature. There are several ways to recalculate BSF area densities into line density values. Assuming a random distribution of BSF in both crystal directions, one can extract the root of the area density, which yields a line density of $8.4 \cdot 10^3 \text{ cm}^{-1}$. In view of the hitherto given numbers, this number appears plausible. However, as mentioned before, the exact physical mechanism leading to the BSF contrast in the ECCI is yet not fully understood. Thus, one cannot unambiguously state the type of the BSF, which are visible in ECCI. Therefore, it is very difficult to compare these numbers and draw good conclusions out of it. But one can already state that this method is highly promising for the further development of nonpolar GaN films on any kind of substrate.

The most important consequences from the structural study of *m*-plane GaN films on LiAlO₂ can be summarized as follows: The layers are made up of stripes aligned parallel to the GaN *c*-axis, which consist of very coherent and high-quality crystal domains. The total defect density is relatively low for heteroepitaxially deposited nonpolar GaN films. The BSF and TD density is in the order of $1 \cdot 10^4 \text{ cm}^{-1}$ and $1 \cdot 10^9 \text{ cm}^{-1}$, respectively. The defect structure is quite complex with Frank partial dislocations and defects running at a 60° angle being the most prominent ones. The latter type obviously lies on the $(10\bar{1}0)$ prismatic plane and may be related to a prismatic stacking fault, but no clear indication for this theory could be found so far.

7.4 Optical properties of *m*-plane GaN films on LiAlO₂

Studying optical characteristics of *m*-plane GaN films is essential because an emission spectrum can give insights into defects and impurities in the crystal. Also, the special anisotropic nature of the *m*-plane GaN layer gives rise to polarized

emission as described in chapter 3.2, which is interesting from a scientific point of view but may also be of use in several applications. This section is divided into two parts. First, the emission properties of *m*-plane GaN films are studied by PL taking the polarization of emission into special consideration. After that, the luminescence characteristics at high excitation levels are determined to study the optical performance in conditions similar to LD or high-brightness LED operation.

7.4.1 Polarization-resolved luminescence characteristics

PL was performed at 14 K and 300 K on a 0.9 μm thick *m*-plane GaN film on LiAlO₂ with 8 min nitridation step. The spectra are displayed in Figure 7.11 a).

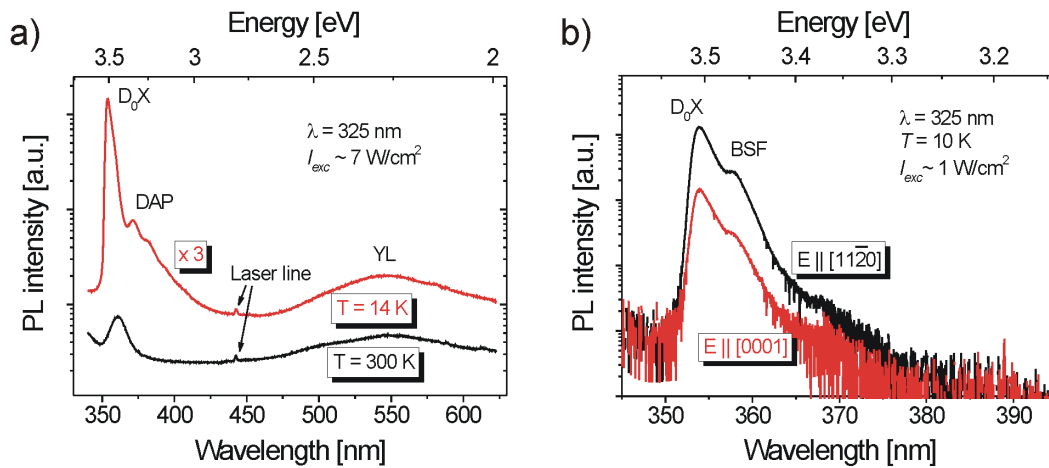


Figure 7.11: a) LT and RT PL spectra for 0.9 μm thick *m*-plane GaN film grown on 8 min nitridated LiAlO₂. The LT spectrum is shifted vertically for clarity. b) LT PL spectrum of 1.7 μm thick *m*-plane GaN with 5 min nitridation for emission polarization parallel and perpendicular to the GaN *c*-axis.

Several characteristic emission features can be identified. The RT scan shows a near-band-edge (NBE) emission peak at 3.44 eV and a broad band at around 2.3 eV, the position and shape of which are similar to the YL in *c*-plane GaN films [145-147]. The origin of this feature is most likely related to impurities, a topic which will be

discussed in detail in section 8.2. The YL is basically unchanged for the spectrum at LT. Additionally, an increased PL signal between 3.0 eV and 3.4 eV with small peaks at 3.34 eV and 3.25 eV is observed. The relative separation of these peaks is close to the GaN longitudinal optical phonon energy (~ 91.8 meV), which hints on the connection to donor-acceptor pair (DAP) transitions [148, 149]. A further contribution to the high PL intensity in this range may be caused by luminescence from PSF or BSF and their connected partial dislocations [46, 150]. Besides, a strong and sharp donor-bound exciton (D_0X) emission becomes the dominant emission peak appearing at an energy of 3.51 eV with a peak FWHM of 4.4 meV. Compared to typical peak positions of GaN films, the positions of both the LT D_0X and the RT NBE emission are strongly blue-shifted, which is easily explained by the large in-plane compressive strain. A closer look on the D_0X peak reveals a slightly asymmetric shape. It is difficult to separate the contributing emission peaks in this non-polarization-resolved PL spectrum because of an overlapping of peaks, which are caused by transitions to different valence subbands. A polarization-resolved spectrum of a similar sample but with 1.8 μm thickness and 5 min nitridation time before growth is shown in Figure 7.11 b). In these graphs, a distinct shoulder on the lower-energy side is clearly visible at around ~ 3.47 eV for both polarization states. The most plausible interpretation of this line is a BSF-related luminescence, since a correlation of I_1 -type BSF and PL emission at 3.42 eV has been reported for *a*-plane GaN films [46-48]. To explain the different energetic position, the consideration of BSF as QW-like crystal distortions (compare section 3.1.1) is helpful. In this model, the band offsets are fixed and the emission from the QW will thus be shifted as the band gap changes due to strain. The energetic separation between the D_0X peak and BSF shoulder of ~ 40 meV is in reasonable agreement to values for *a*-plane GaN given in literature, which range from 48 meV to 61 meV [44, 48]. The much weaker intensity of this defect-related emission compared to the D_0X peak is in contrast to most literature reports about nonpolar heteroepitaxy of GaN and another clear sign of relatively low BSF density in the *m*-plane GaN films on LiAlO₂.

Comparing the emission intensities for both polarization directions displayed in Figure 7.11 b), one can find higher peaks for the polarization parallel to $[11\bar{2}0]$, which is due to the predominant $\langle X \rangle$ -like character of the HH band (compare section 3.2). This corresponds to a polarization of the T_1 transition along $[11\bar{2}0]$ as also

found by other groups [61-63]. The calculated DoP for different temperatures is plotted together with the NBE peak position in Figure 7.12 a). The dependency of the NBE energy on temperature is readily explained by the bandgap shrinkage. High DoP values up to 0.8 are detected for LT, which decline to ~ 0.4 for RT. This effect can be understood by taking into account the thermal escape of holes to lower-energy valence bands. As a consequence, the intensity of the T_1 transition is reduced for the benefit of T_2 .

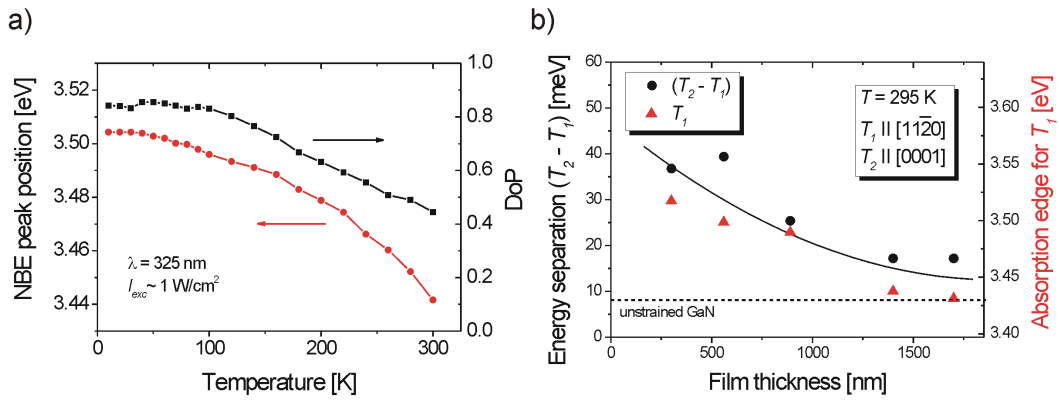


Figure 7.12: a) Development of the PL NBE peak position and its DoP with temperature. b) Valence subband energy separation and T_1 absorption edge at RT for various film thicknesses. The dashed line represents the respective values for unstrained GaN [21, 61]. The solid line is a guide for the eye.

Such a mechanism implies an energy difference ($T_2 - T_1$) of the two valence subbands below or close to thermal energy $k_B T$. Transmittance tests were performed to determine the exact valence subband separation for m -plane GaN films with different thicknesses. Figure 7.12 b) visualizes this dependency of RT subband energy separation ($T_2 - T_1$) and the RT absorption edge for the T_1 transition on the GaN film thickness. Larger film thickness is correlated to less in-plane compressive strain, which results in a lower bandgap. Although the values for the energy separation ($T_2 - T_1$) are quite scattered, an overall decreasing is obvious. The weaker energy separation is accompanied by a decrease of the RT DoP of the PL emission from ~ 0.6 to ~ 0.3 .

A lower energy separation and a smaller difference in oscillator strength for the T_1 and T_2 transitions (resulting in a lower DoP) with reduced in-plane strain of *m*-plane GaN films have been theoretically predicted and even quantified by Ghosh et al. [61]. The general trend of decreasing energy separation with thicker and therefore less strained films observed here is consistent with this theory. However, a good matching of the optically measured ($T_2 - T_1$) values with the energy separation calculated using the strain data obtained by HRXRD was not found. In fact, this calculation yields a typically by a factor of two larger separation compared to the result yielded by optical transmission. Two systematic errors are proposed: One is related to the limited accuracy of the in-plane strain measurement by HRXRD due to crystal imperfections and low reflected intensity at asymmetric planes. Further, the layer information in optical transmission stems from the whole depth range of a sample, while HRXRD takes mostly the strain state of the uppermost regions into account. The usage of transmission data for bandgap estimation is also the main reason why the values presented here are quite different to a similar experimental study by Misra et al., who used photoreflectance data to extract a subband energy separation of 46 meV for a 1.2 μm thick *m*-plane GaN film on LiAlO₂ [63]. Nevertheless, the optical study presents a further evidence for a strain relaxation process of *m*-plane GaN films on LiAlO₂ substrates.

7.4.2 Study of high-excitation luminescence and free carrier dynamics

To study the optical properties of *m*-plane GaN films at high excitation conditions, PL experiments were carried out at RT using the fourth harmonic of a YAG:Nd³⁺ laser as a light source [151]. The sample under investigation was a 1.6 μm thick GaN film grown after 2 min nitridation of LiAlO₂. To allow for a reference, a *c*-plane GaN film grown on sapphire was also characterized. This layer consisted of $\sim 2 \mu\text{m}$ GaN deposited onto a 300 nm AlN nucleation layer. Its threading dislocation density was estimated to be $\sim 5 \cdot 10^9 \text{ cm}^{-2}$ via etch pit density and XRD measurements [152]. Figure 7.13 a) displays the PL spectra of the *m*-plane GaN layer at various excitation levels. At the lowest excitation level of 0.62 mJ/cm^2 (which equals to a photogenerated carrier density of $\sim 2 \cdot 10^{18} \text{ cm}^{-3}$), a broad spontaneous emission band at 3.41 eV is observed, which is identical to the RT NBE peak from Figure 7.11 a). When increasing the excitation density I_{exc} to $\sim 0.87 \text{ mJ/cm}^2$, laterally amplified stimulated

emission (SE) emerges at 3.33 eV. The amplification without application of external mirrors has been observed for *c*-plane GaN in literature before and can be assumed to occur because of propagation of emission in lateral direction and its partial backscattering via layer imperfections like grain boundaries [153]. The redshift of the SE peak is caused by both re-absorption of luminescence with higher energy as well as band gap renormalization [153].

Excitation-dependent PL spectra were taken for the *c*-plane GaN reference layer as well. A similar appearance can be assessed with the SE emerging at a higher excitation level of 1.4 mJ/cm². The integrated intensity of the PL emission for both films as a function of excitation level is plotted in Figure 7.13 b). The threshold value is marked by vertical arrows.

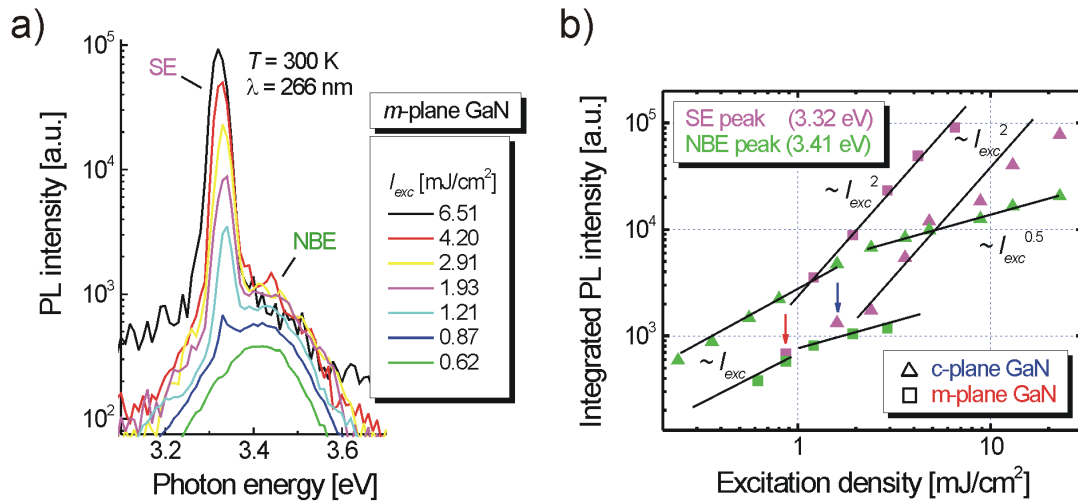


Figure 7.13: a) Excitation-dependent RT PL spectra of an *m*-plane GaN film. b) Integrated PL intensity plotted against excitation level for *m*-plane and *c*-plane GaN. The solid lines and vertical arrows indicate the proportionality of the PL intensity and the SE threshold, respectively.

At low excitation, a linear growth of the NBE emission is found for both samples. When the excitation level reaches the threshold value, a gradual saturation of the NBE intensity occurs (which can be described by a $\sim I_{exc}^{0.5}$ power law), while the SE shows a square increase. Since imperfections play a major role in the self-

amplification effect, the different defect structure could be responsible for the larger value of the SE threshold in the *c*-plane GaN film. It is also known, that some defects may act as radiative recombination centers emitting slightly below the bandgap, which would lower the SE threshold in the more defective layer [154]. Further, an influence of in-plane stress enhancing the band-edge emission in defective regions should also be considered [155]. The SE threshold value can also be determined via the monitoring of the intensity-dependent diffraction efficiency in a free-carrier transient grating, which is created by the interference of two pump beams in the FWM technique (compare Figure 5.1). This efficiency of diffraction for both the *m*-plane GaN and *c*-plane GaN film is plotted in Figure 7.14 a). A squared proportionality versus excitation intensity is found. The onset of SE leads to a lower diffraction efficiency due to a sudden decrease of the free carrier concentration by the SE process. One can extract SE threshold values of 0.8 and 1.3 mJ/cm² for the *m*-plane GaN and *c*-plane GaN layer, respectively, thus yielding a good confirmation of the values obtained by PL.

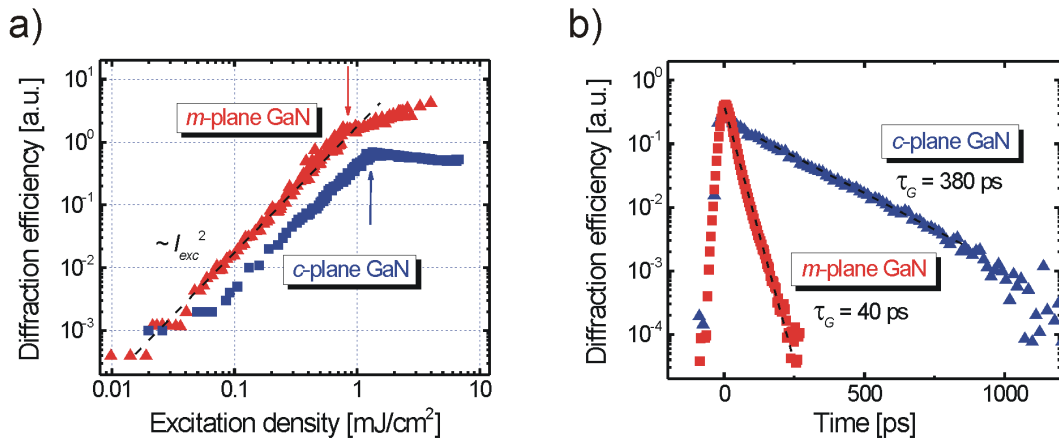


Figure 7.14: Diffraction efficiency of transient grating in *m*-plane and *c*-plane GaN films for a) excitation-dependent and b) time-resolved measurements. Vertical arrows mark the onset of SE.

The FWM technique can also be applied in a time-resolved measurement scheme, which allows for a monitoring of the carrier dynamics. Figure 7.14 b) displays the transient diffraction efficiency for both GaN films. The value exponentially decreases

after the pump beams are blanked. A grating decay time τ_G of 40 ps and 380 ps can be extracted for the *m*-plane and *c*-plane GaN layer, respectively, and was validated for a wide range of excitation levels. No dependency of the grating decay on grating period was detected for the *m*-plane GaN film, thus indicating negligible impact of a diffusive decay of the grating (as described in equation (5.2)) caused by minority (hole) carrier diffusion. Consequently, the determined grating decay time of 40 ps is equal to the carrier lifetime τ . It is notable to mention that PL decay times of 75 ps and 268 ps were found for free-standing *m*-plane GaN films grown on GaN/LiAlO₂ templates and sliced GaN boules, respectively [139, 156]. The much larger film thicknesses will of course result in a lower density of defects and impurities, so the difference can well be understood. In case of the *c*-plane GaN reference layer on sapphire, a grating decay time of 380 ps is measured. The slower recombination dynamics in polar MQW can partly be ascribed to the QCSE. Based on bipolar diffusion coefficient for *c*-plane GaN and a semi-empirical equation, both of which can be found in the literature, one can make an estimation for the total TD density [157, 158]. The calculated number for $N_{TD} \approx 4.6 \cdot 10^9 \text{ cm}^{-2}$ in the reference *c*-plane GaN layer is found consistent with the expectations. Nevertheless, a similar procedure cannot be applied for the *m*-plane GaN layer because for nonpolar GaN layers, the relationship between N_{TD} and lifetime was found to be extremely weak. Chichibu et al. found that if N_{TD} increases by three orders of magnitude, the PL lifetime decreases only twice, which is assumed to be caused by a dominant contribution of other electrically active defects [156].

All optical results appear to be consistent with the gathered structural data by yielding further evidence for the high quality of the *m*-plane GaN layers on LiAlO₂. The main features are a strong D₀X emission peak and only weak contributions of defects, which are mainly caused by impurities. Large in-plane compressive strain is identified and relaxes as films grow thicker. This reflects in a change of the absorption edge energy, the DoP, and the subband energy separation. The lower lasing threshold for *m*-plane GaN compared to *c*-plane GaN films is ascribed to a very different defect structure for the two orientations. The measured carrier lifetime for *m*-plane GaN on LiAlO₂ is consistent with other reports for high-quality nonpolar GaN films.

7.5 Doping and electrical characterization of *m*-plane GaN on LiAlO₂

Irrespective of growth technique, GaN films deposited on LiAlO₂ substrates are known to have a large unintentional n-type doping concentration [18, 77, 159]. The origin of this issue will be discussed in detail in chapter 8. One can make use of this unintentional doping level to study the in-plane anisotropic electron mobility μ . RT Hall measurements employing a Hall bridge geometry were carried out for that purpose. GaN layers with 2 min nitridation step and various thicknesses ranging from 260 nm to 1.7 μm were investigated. Ohmic behaviour was readily observed without further annealing step, which is obviously related to the high doping level. The space charge region of the Schottky barrier of the metal-semiconductor contact becomes extremely thin in that case and can thus be neglected. The development of electron concentration and in-plane mobility for directions parallel and perpendicular to the *c*-axis is plotted in Figure 7.15. With increasing layer thickness, the background electron concentration is reduced from $\sim 10^{20} \text{ cm}^{-3}$ to $\sim 10^{19} \text{ cm}^{-3}$. In view of the large horizontal separation of the contacts compared to the film thickness, one can assume that even the lower-lying areas of the layer contribute to the Hall result. The measurement of thicker films is therefore hampered by a superposition of the higher electron concentration on the bottom and the lower carrier density on the top. The decline of electron density is most likely linked to the lower impurity incorporation, which also leads to less scattering of carriers, thereby increasing the mobility from $20 \text{ cm}^2/\text{Vs}$ to more than $120 \text{ cm}^2/\text{Vs}$. The decrease of mobility after 1 μm film thickness is ascribed to a lower GaN crystal quality probably due to strain-induced defect generation. The samples compared here have been grown on distinguished sets of LiAlO₂ substrates. Thus, different substrate qualities may also play a role.

While the electron densities show no or only negligible deviations for the two measurement directions, a clear anisotropy of the in-plane mobility was found, especially for larger mobility values. The effective electron mass of GaN does not exhibit any anisotropy, which could give rise to larger mobility in the *c*-axis direction [57, 65]. Thus, only the special anisotropic crystalline structure with the stripes being oriented along [0001] can be blamed for the observed larger values along this direction.

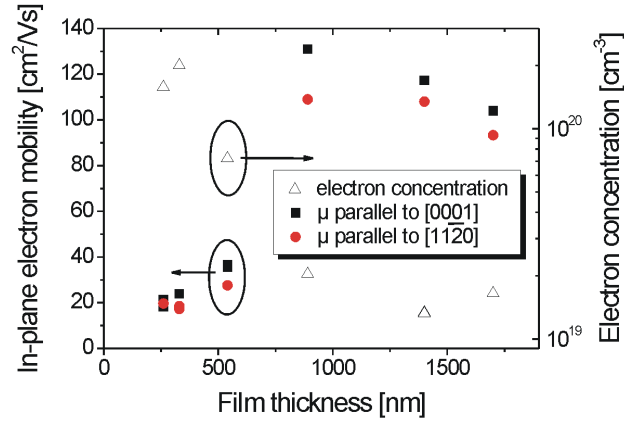


Figure 7.15: RT electron concentration and in-plane electron Hall mobility measured along the two in-plane crystal axes of *m*-plane GaN films with different thicknesses.

Both in-plane mobility values are superior to data for MBE-grown films on LiAlO₂ and comparable to reports for 300 - 400 μm thick HVPE-grown *m*-plane GaN films on LiAlO₂, which is ascribed to the well-engineered MOVPE deposition process [77, 159, 160]. However, higher electron mobilities were achieved for Si-doped *m*-plane GaN layers on *m*-plane 6H-SiC [90]. In this case, values of up to 500 cm²/Vs and 300 cm²/Vs at an electron density of $4 \cdot 10^{19} \text{ cm}^{-3}$ have been reported for the $[11\bar{2}0]$ and $[0001]$ direction, respectively. The difference was ascribed to scattering near structural defects like BSF.

In spite of the large unintentional n-type background doping level, p-type conductivity was also achieved. However, a large amount of Mg is necessary to overcompensate the free electron concentration in *m*-plane GaN on LiAlO₂. Films grown at 900 °C with Mg/Ga ratios of 0.8% and 1.3%, which are standard doping ratios for reference *c*-plane GaN layers, did not result in p-type conductivity in RT Hall measurements. Increasing the Mg/Ga ratio to 2.6% led to p-type doped films. The Hall results showed a linear behaviour of the I - V curves and a free hole concentration of $8 \cdot 10^{17} \text{ cm}^{-3}$ at a hole mobility of 1.3 cm²/Vs after the same annealing procedure. The very low hole mobility is likely caused by the large defect and impurity concentration in these highly doped films. On the other hand, one can partly ascribe it to the fact that both the growth and annealing conditions have not been optimized for Mg-doped *m*-

plane GaN layers and all parameters were taken from the procedure developed for *c*-plane GaN films.

The electrical data of *m*-plane GaN films on LiAlO₂ underline the high structural material quality. The observed anisotropy of the electron mobility can be explained by the anisotropic growth mode, which results in improved crystalline coherence along the *c*-axis of GaN. A large background electron concentration presents a challenge to achieve high-quality p-type doped films. Thus, any improvements on this issue heavily rely on a reduction of the unintentional doping level. In order to achieve this goal, its origin needs to be understood in detail, which is the aim of the following chapter.

8 Impurities in *m*-plane GaN films on LiAlO₂

This chapter deals with the issue of impurity incorporation in *m*-plane GaN films on LiAlO₂. Beside of the detection of impurities, possible mechanisms of incorporation into the GaN lattice are discussed.

8.1 Identification and quantification of impurity atoms

When looking for foreign atoms in a crystal, one needs to be aware about potential sources for contamination. The source and carrier gas molecules in the MOVPE process contain H and carbon (C), both of which are foreign atoms for GaN epitaxy. Furthermore, water is a common impurity in NH₃. Even though an additional purifier has been used for epitaxy in all experiments, the supply of small amounts of O cannot be excluded. Another source of impurities is given by the LiAlO₂ substrate. As already discussed in section 6.1, the stability of LiAlO₂ in the MOVPE environment is questionable, especially considering a possible release of Li₂O [117]. Thus, O and Li are potential impurity atoms for GaN epitaxy. Time-of-flight secondary ion mass spectroscopy (SIMS) experiments were carried out on two *m*-plane GaN films on LiAlO₂. One of them was grown with a total thickness of 1.6 μm after a 2 min nitridation step. Another layer comprises an 8 min nitridation process and a thickness of 0.9 μm. The SIMS analysis was performed using argon (Ar) and O sputter gas to be sensitive for O and Li foreign atoms in the GaN lattice, respectively. Calibration measurements on O- and Li-implanted *c*-plane GaN films were performed to enable a quantitative analysis of these elements.

Figure 8.1 a) shows the SIMS depth profile for the 1.6 μm *m*-plane GaN layer using Ar sputter gas. Besides of the signal arising from Ga bound to N, only O and C bound to N atoms are detected in this spectrum. C is located on a N site and is thought to act as a deep acceptor in GaN with activation energy of 0.9 eV [147]. It is therefore typically located below the Fermi level of GaN and can only have a limited impact on electrical properties. A strong contribution to the n-type conductivity can be expected

from O, as it is known to form a shallow donor in GaN [161]. And indeed, the detected O level of $1 \cdot 10^{19} \text{ cm}^{-3}$ is in very good agreement to the electron concentration extracted from RT Hall measurements. One can also note a distinct decline of the O signal towards the layer surface. This hints on a slightly lower incorporation of O in the upper region of the film. The sharp increase for C-N and O beyond a depth of $1.5 \mu\text{m}$ can be ascribed to a partial sputtering of the substrate.

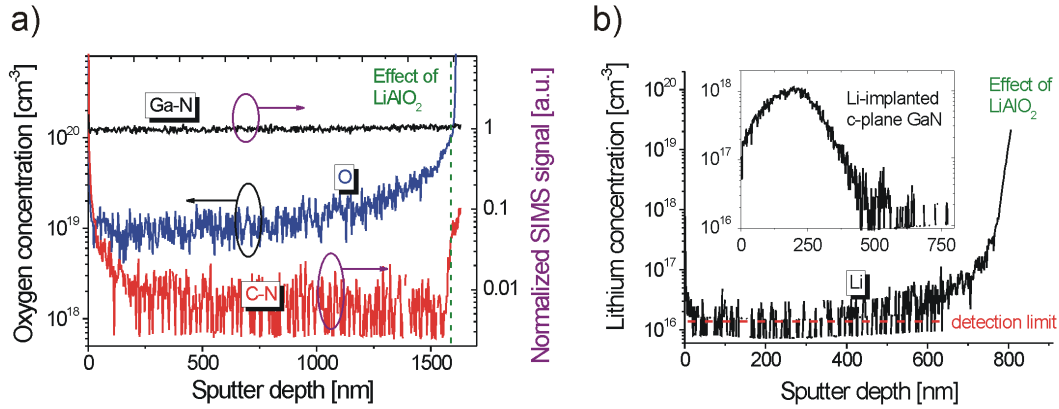


Figure 8.1: SIMS depth profiles of m-plane GaN on LiAlO₂. a) Qualitative profiling of Ga-N and C-N and quantitative analysis of O concentration in a $1.6 \mu\text{m}$ GaN film using Ar sputter gas; b) Quantitative Li detection in a $0.9 \mu\text{m}$ GaN film using O sputter gas. The inset shows the Li-implanted calibration sample.

The increase of the C-N concentration close to the surface is not fully understood at present. Yet, it is worth to mention that also the O signal exhibits a similar but much sharper surface peak. Figure 8.1 b) displays the Li depth profile for the $0.9 \mu\text{m}$ thick GaN film measured using O as sputter gas. Again, a decline of the Li concentration from the substrate-layer interface towards the surface is found. The lowest measured concentration of Li in the GaN layer of $\sim 1.4 \cdot 10^{16} \text{ cm}^{-3}$ is hardly exceeding the detection limit of the analysis. Similar to the C-N and O signal, the Li concentration is slightly increased close to the surface. It is interesting to note that all implanted c-plane GaN calibration samples do not exhibit such a surface effect. The spectrum for the Li-implanted layer is exemplarily given in the inset of Figure 8.1 b). A further discussion of these surface features is postponed to the next section.

Dikme et al. reported on the presence of even higher levels of O in the order of $5 \cdot 10^{19} \text{ cm}^{-3}$ for their MOVPE-grown *m*-plane GaN films on LiAlO₂ using InGaN:Mg buffer layers [18]. They further mentioned the presence of Li with its density being roughly one order of magnitude lower than the one for O. One can thus assess that either the stability of the LiAlO₂ substrate or the deposition process itself has strongly improved compared to these earlier experiments. However, an even lower O level of around 10^{18} cm^{-3} was specified in case of MBE-grown *m*-plane GaN on LiAlO₂, which may be related to the completely different growth conditions including lower deposition temperature as well as ultra-high vacuum and high-purity environment [159]. Of course, the overall very high O background levels in both this study and literature reports still need a physical explanation.

A naturally increased incorporation of O impurities on *m*-plane GaN surfaces compared to other orientations like the Ga-faced *c*-plane or the *a*-plane surface was recently reported by Cruz et al. [162]. Even though these studies were carried out on bulk GaN substrates, O background levels up to $3 \cdot 10^{18} \text{ cm}^{-3}$ have been detected when the growth temperature was 890 °C. Residual impurities in the used source gases have been blamed as the probable origin. In contrast, the density of O atoms drops below $5 \cdot 10^{16} \text{ cm}^{-3}$ for deposition processes performed at temperatures above 1100 °C. This was explained by the limited stability of Ga oxides on the GaN surface at elevated temperatures [163]. In case of deposition of *m*-plane GaN on LiAlO₂, both the decreased temperature on the GaN surface as well as the substrate as potential O source may have an impact, so an unambiguous conclusion on the impurity source and the doping mechanisms is not possible. Additional experimental efforts have been made to elucidate the problem.

8.2 Mechanisms of impurity incorporation during MOVPE of *m*-plane GaN on LiAlO₂

Beside of an increased affinity of the *m*-plane GaN surface for O atoms at low growth temperatures, several other potential mechanisms for higher O incorporation are conceivable. One may be related to the surface morphology, which exhibits hillocks and steps with more or less inclined facets. Although the *m*-plane surface already exhibits increased O incorporation, even larger affinities for O have been found for

some semipolar planes like the $(1\bar{1}01)$ or $(11\bar{2}2)$ surface [162]. Thus, some tilted facets of the *m*-plane GaN layer may attract considerable amounts of O, which are subsequently incorporated into the bulk film. Even if one assumes an unchanged affinity for O, the mere increase of the total free surface area caused by roughness during epitaxy might already have a significant impact on the impurity incorporation. However, an experimental confirmation of this theory is not an easy task because a complete suppression of the surface features of *m*-plane GaN films on LiAlO₂ has not been achieved so far. As a second factor, O out-diffusion from the LiAlO₂ substrate has to be considered. There are basically two ways for diffusion of species into the GaN layer: One is related to solid-state diffusion, which may be enhanced by defects [164]. However, the upper limit for the diffusivity of O in GaN at a much higher temperature of 1125 °C has been specified to $2.7 \cdot 10^{13} \text{ cm}^2/\text{s}$, which would not be able to describe the observed tendency [165].

Another mechanism could involve diffusion of the foreign species into the reactor atmosphere and subsequent re-incorporation into the GaN film. Special experiments have been carried out to test for potential autodoping via the gas phase [166]. A sapphire substrate was put next to a LiAlO₂ substrate piece into the MOVPE reactor for the deposition of a $\sim 1.2 \text{ }\mu\text{m}$ thick *c*-plane GaN film grown on top of a thin GaN nucleation layer. The surface temperature during the nucleation step and main layer growth was set to $\sim 500 \text{ }^\circ\text{C}$ and $1070 \text{ }^\circ\text{C}$, respectively. XRC Omega scans and RT Hall measurements have been performed on both this layer and a reference *c*-plane GaN film grown under equal conditions but without the co-loaded LiAlO₂ substrate. The results are listed in Table 8.1.

Table 8.1: XRC FWHM and RT Hall results for c-plane GaN films with and without a co-loaded piece of LiAlO₂.

	XRC FWHM GaN		Electron	Electron
	(0002)	/ (10 $\bar{1}$ 2)	mobility	density
GaN/Al ₂ O ₃	307''	462''	178 cm ² /Vs	$0.77 \cdot 10^{17} \text{ cm}^{-3}$
GaN/Al ₂ O ₃ : LiAlO ₂	360''	666''	182 cm ² /Vs	$2.17 \cdot 10^{17} \text{ cm}^{-3}$

Beside of a slightly degraded sample quality, the LiAlO₂ inside the reactor obviously increases the background electron concentration of this *c*-plane GaN film. Yet, the doping concentration is still almost two orders of magnitude lower compared to the one typically achieved for *m*-plane GaN films on LiAlO₂, which is readily explained by the different surface orientation and higher growth temperature. The possible impact of impurity incorporation on the optical properties has been studied by comparative PL measurements. The LT spectra of both GaN films are depicted in Figure 8.2 and show almost equally intense NBE emission peaks.

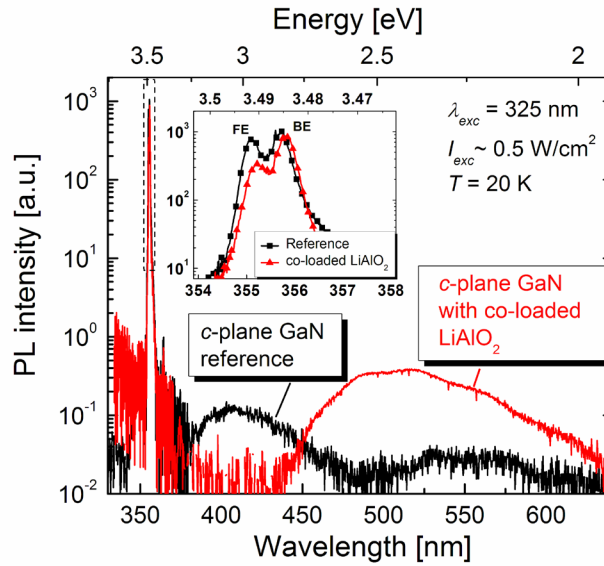


Figure 8.2: LT PL spectra of *c*-plane GaN films grown with and without co-loaded LiAlO₂. The inset shows a magnification of the GaN exciton emission peaks.

Two main differences are distinct. One is related to the GaN peak at ~ 3.5 eV, which is separated into a free exciton (FE) and a bound exciton (BE) peak as highlighted in the inset of Figure 8.2. The FE emission is less intense for the film with the co-loaded LiAlO₂ substrate. As a second effect, a broad band at ~ 2.5 eV emerges in this potentially contaminated film, while the reference GaN layer shows a weaker emission at ~ 3 eV. The origin of the latter peak is unclear yet, but the broad emission at ~ 2.5 eV resembles the YL band of GaN. This band involves a transition from a

shallow donor to a deep acceptor [145]. While the acceptor may either involve Ga vacancies or C impurities on a N site [126, 147, 167], the shallow donor is most likely linked to the presence of O [146]. Thus, these results provide strong evidence for an out-diffusion of O-containing species from the LiAlO₂ substrate.

In a second experiment, the substrate backside of a 0.9 μm thick *m*-plane GaN specimen was sealed by evaporation of a 0.8 μm thick Ti coating to prevent any direct out-diffusion of impurities from the substrate. After cleaning of this template in boiling solvents, 0.45 μm GaN was deposited on top. Since the Ti surface is transformed into titanium nitride, the backside appears golden without any stains or holes. The XRC FWHM data of the film is equal to the one of a reference layer. However, in contrast to our expectations, the measured electron concentration of the backside-coated template even slightly increases to $2.8 \cdot 10^{19} \text{ cm}^{-3}$ compared to $2.3 \cdot 10^{19} \text{ cm}^{-3}$ for the reference film. SIMS O and Li depth profiles for this re-grown *m*-plane GaN film are shown in Figure 8.3. The position of the growth interruption is marked by a sudden increase of both the O and Li impurity levels.

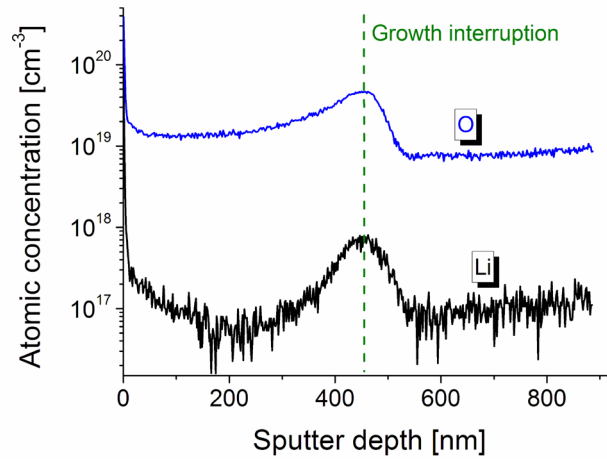


Figure 8.3: SIMS depth profiles of *m*-plane GaN film for O measured using Ar sputter gas and Li measured using O sputter gas. The position of growth interruption and metal deposition on the substrate backside is marked by dashed lines.

Since the LiAlO₂ surface was not exposed to the reactor ambient in this case, a direct out-diffusion from the substrate cannot be blamed as the single origin. Instead, residual impurity atoms on the surface of the template may play a more important role. Similar to Figure 8.1, an increased concentration of foreign atoms very close to the surface can again be observed in both graphs in Figure 8.3. As mentioned before, this surface peak is not seen in the Li-implanted sample. Thus, the effect is obviously not caused by residual dirt on the sample surface but should rather be related to the presence of impurities in the reactor chamber after the deposition process. Residual impurities in the gas phase may attach to the GaN surface during cool-down and form this thin accumulation layer. Another mechanism likely to be involved is the higher incorporation of impurities at the more defective re-growth interface region. Accumulation of impurities near highly dislocated areas has been reported for GaN films before [168].

To conclude these results, one can state that although out-diffusion of O and Li from the substrate into the gas phase is evident, it is not the single effect contributing to the autodoping process of the GaN film. Another important factor is the high stability of impurity atoms on the rough *m*-plane GaN surface at low growth temperature. These residual foreign atoms are likely to form a thin contamination layer on the surface after growth. To avoid high background impurity levels, an optimization of the deposition process towards higher growth temperatures and smoother surfaces appears to be the most promising way.

9 Growth and characterization of *m*-plane InGaN/GaN multiple quantum well heterostructures

This chapter provides some experimental data on *m*-plane InGaN/GaN-based MQW grown on LiAlO₂ regarding structural and optical properties and focussing on basic differences to *c*-plane-oriented heterostructures. The first part is focussed on structural and morphological layer properties. Optical characterization is described in the second section, followed by the demonstration of *m*-plane InGaN-based LED characteristics.

9.1 Morphological and structural properties of *m*-plane InGaN/GaN quantum well structures

Epitaxial growth of the InGaN/GaN multiple quantum wells was performed on top of $\sim 1 \mu\text{m}$ thick *m*-plane GaN buffer layers on LiAlO₂, which were fabricated under optimized conditions (employing an 8 min nitridation step) as described in section 7.1. However, due to substrate reproducibility issues, which manifest in larger roughness and increased XRC FWHM values, a slightly degraded crystalline quality of the GaN buffer was found for the MQW samples. This is reflected by a broadened XRC FWHM value for GaN of $\sim 420''$ for the (1 $\bar{1}$ 00) reflection taken along [0001] beam direction (compared to $305''$ for GaN films on high-quality LiAlO₂ substrates). Following the GaN deposition, the temperature T_g was ramped down to the surface temperature for well and barrier growth. T_g was varied between 690 °C and 780 °C to adjust the In content in the different samples [166]. Carrier gas was switched to N₂, and a V/III ratio of 270 was chosen. Five QW structures were deposited with well and barrier thicknesses being set to 4 and 16 nm, respectively. As a reference, the same MQW growth conditions have been applied to deposit a *c*-plane InGaN/GaN MQW on a GaN/AlN/sapphire buffer layer at a temperature of 750 °C. Since the growth rates for *m*-plane and *c*-plane MQW deposition were found to be slightly different, the growth times have been slightly adjusted resulting in a well and barrier thickness

of 5 and 16 nm, respectively. Figure 9.1 shows the symmetric HRXRD 2Theta/Omega scans for the *c*-plane (a) and *m*-plane (b) InGaN MQW structures at 750 °C deposition temperature. Both scans show the GaN main peak and distinct superlattice (SL) oscillations up to the 4th order. This indicates high interface quality and allows for a simulation to determine both the composition and the exact well/barrier thicknesses.

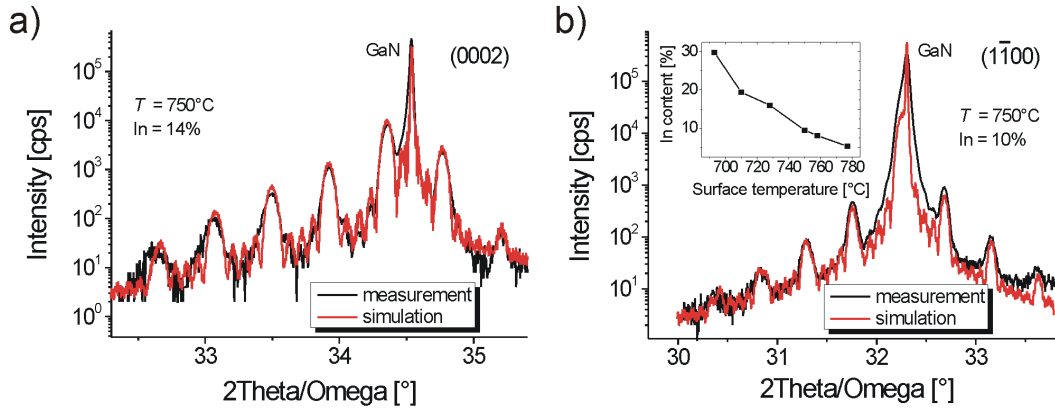


Figure 9.1: Measured and simulated HRXRD symmetrical 2Theta/Omega scans for a) *c*-plane and b) *m*-plane InGaN/GaN MQW grown at equal conditions. The inset of b) shows the dependency of In content on the surface temperature for *m*-plane MQW.

In case of the *c*-plane MQW in Figure 9.1 a), an excellent fit can be achieved yielding an In fraction of 14%. Since the SL oscillations of the *m*-plane MQW structure in Figure 9.1 b) are slightly less pronounced, the assumption of some diffuse scattering was necessary to attain a good simulation fit. An In content of only 10% is extracted, which is in agreement to literature reports about lower In incorporation efficiency on *m*-plane surfaces [19, 32, 169]. The inset of Figure 9.1 b) also displays the dependency of In concentration on surface temperature during MQW deposition. In spite of the lower incorporation efficiency, In fractions between 5% and 30% could be achieved. The virtually linear decrease with temperature is a typical behaviour for MOVPE deposition of InGaN alloys [170].

All compositional data extracted by simulation fits of symmetrical 2Theta/Omega scans are based on the assumption of pseudomorphic QW growth. This is confirmed

by HRXRD reciprocal space maps (RSM) of the *m*-plane MQW structure, which were taken for two asymmetric reflections as shown in Figure 9.2. RSM are plotted for the $(2\bar{2}03)$ and $(3\bar{2}\bar{1}0)$ reflections, which refer to planes tilted in the *c*- and *a*-axis direction, respectively. In both cases, the GaN peak and SL oscillations caused by the InGaN MQW are visible. The $(3\bar{2}\bar{1}0)$ map exhibits stronger broadening along Q_x with only one visible SL peak representing a higher structural disorder. This phenomenon is obviously a reproduction of the anisotropic crystal coherence of the underlying GaN buffer. Although the Q_x positions for GaN and the SL fringes are difficult to determine from this plot, no clear indication for relaxation can be detected. A more informative scan could be achieved for the $(2\bar{2}03)$ reflection, which corresponds to a tilt of the plane along the GaN *c*-axis. The distinct SL oscillations are found at the same horizontal position as the GaN main peak and are thus clear evidence for the pseudomorphic growth mode of the InGaN QW. The same situation was also found for other InGaN compositions with exception of the sample with 30% In fraction, which shows too weak SL oscillation intensity to rule out partial relaxation.

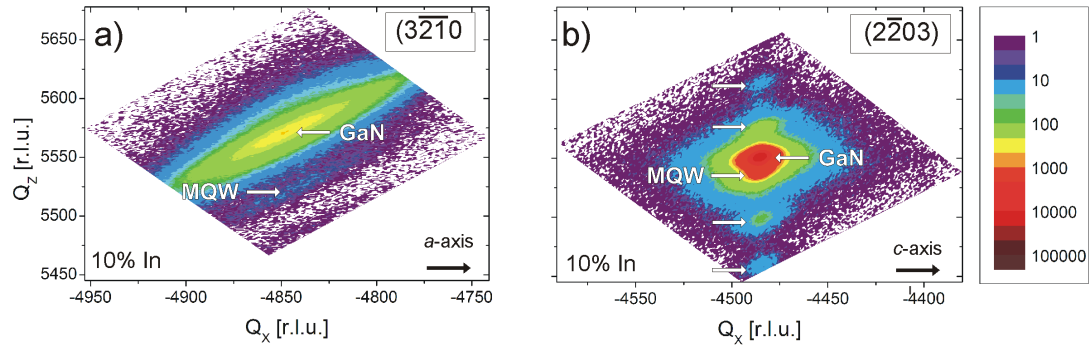


Figure 9.2: HRXRD RSM of a) $(3\bar{2}\bar{1}0)$ and b) $(2\bar{2}03)$ reflection of an *m*-plane $\text{In}_{0.1}\text{Ga}_{0.9}\text{N}/\text{GaN}$ MQW. The arrows indicate the peak position of GaN and the MQW SL oscillations.

The surface morphology of the *m*-plane InGaN/GaN MQW was probed by AFM. Figure 9.3 exemplarily displays two surface scan images for MQW structures grown with a) 5% and b) 30% In fraction. In addition to the stripes extended towards the

[0001] direction, which stem from the *m*-plane GaN buffer layer, a corrugated pattern with elongated features in the perpendicular $[11\bar{2}0]$ direction is visible on the MQW surface. These grooves increase in density for larger In contents. The origin of the undulations can only be speculated on at this time. Both the higher strain as well as the lower growth temperature for the high-In-fraction MQW deposition may affect the diffusion length of species and cause an altered surface morphology. Also, a generation of BSF within the MQW structure is possible, which would likely have an impact since BSF have been reported to cause similar striped surface features in *m*-plane GaN [35, 92].

To determine whether the MQW deposition step has such detrimental influence on the structural sample quality, ECCI was performed on the *m*-plane InGaN MQW with 5% In fraction (not shown here). The extracted average TD and BSF density values are as low as $3.6 \cdot 10^9 \text{ cm}^{-2}$ and $0.9 \cdot 10^4 \text{ cm}^{-1}$, respectively. Moreover, all BSF revealed by ECCI are located in between the stripe-like features. This indicates that BSF formation is not an origin for this pattern and that the good crystal quality is maintained also during the MQW deposition.

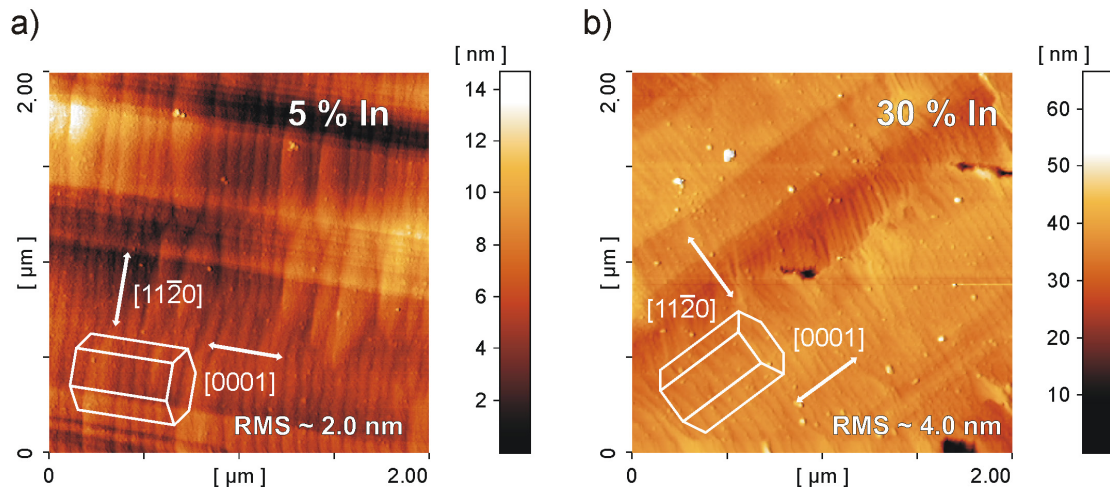


Figure 9.3: AFM images of *m*-plane InGaN/GaN MQW on LiAlO₂ with In fractions of a) 5% and b) 30%. The crystal directions are schematically visualized.

The RMS roughness in a $2 \cdot 2 \mu\text{m}^2$ scan area is found to increase from 2 nm to 4 nm when the In content is enhanced from 5 % to 30%. The roughness is obviously

dominated by some small particles and pits with the latter being more distinct for high In fractions as visible in Figure 9.3 b). A more detailed investigation of these features has been carried out using SEM and cross-section TEM. Figure 9.4 a) exemplarily shows an SEM image for an InGaN/GaN MQW sample with 20% In fraction. Again, stripes along $[11\bar{2}0]$ direction and some surface pits are observed. No particles can be found in SEM for all MQW samples proving that their presence in the AFM scans of Figure 9.3 is likely related to accumulated dust on the surface only.

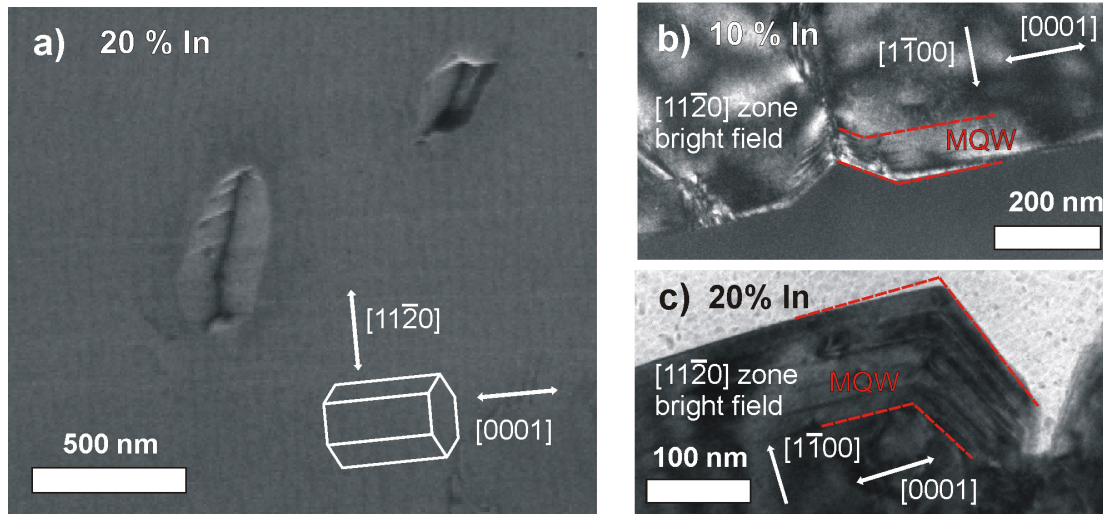


Figure 9.4: Pits on the m-plane InGaN/GaN MQW surface visualized by a) plan-view SEM and cross-section TEM for b) 10% and c) 20 % In content. The MQW region and crystal directions with respect to the surface are also indicated.

The relatively large size of the pits raises the question on their origin and time of generation during the deposition process. As demonstrated earlier (compare Figure 7.3 and Figure 7.4), pit generation was very rarely observed in our optimized GaN deposition process. However, due to substrate reproducibility issues, stronger pit formation in the GaN buffer of the MQW samples cannot be ruled out. The TEM cross-section images in Figure 9.4 b) and c), which were taken along the $[11\bar{2}0]$ zone, clearly indicate a connection of these surface pits to a defect or a bundle of defects within the GaN buffer layer. The depth of the pit in Figure 9.4 c) reaches below the level of the first QW indicating that the pit was already present on the GaN

surface before the MQW growth was initiated. A triangular pit shape is found for both 10% and 20% In content. The MQW growth step obviously leads to an enlargement of the pit size, which is likely because of lowered growth temperature and thus altered diffusion length in the vicinity of a pit. While the pits increase in size, the MQW structure is also deposited on the tilted facets of the pit. Due to the lower facet growth rate, the period length and total thickness of the MQW becomes smaller on the tilted planes, which may affect the emission wavelength. Furthermore, the incorporation of In can be expected to be different on the surface of such semipolar facet planes compared to the *m*-plane surface [171].

More detailed cross-section TEM images of the InGaN/GaN MQW with 20% In content are supplied in Figure 9.5. The overview viewgraph in a) indicates sharp interfaces and allows for an extraction of the exact well/barrier thicknesses, which are found in good agreement to the HRXRD data.

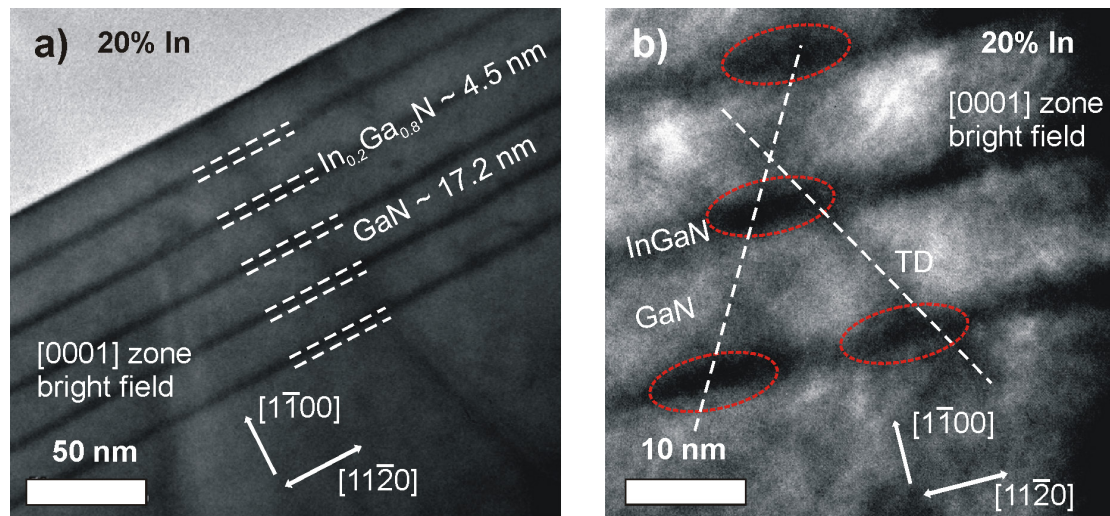


Figure 9.5: Cross-section TEM images of an *m*-plane $\text{In}_{0.2}\text{Ga}_{0.8}\text{N}/\text{GaN}$ MQW on LiAlO_2 taken along the $[0001]$ zone in an a) overview and b) close-up view showing local QW fluctuations as marked by red circles.

Some line dislocations arising in the GaN buffer layer seem to penetrate the MQW stack without any generation or annihilation process occurring. This is highlighted in Figure 9.5 b) showing a close-up view of some TD within the MQW region running

at a 60° angle with respect to the surface. The QW appears darker at the point of intersection with a TD. This may be either explained by compositional or thickness fluctuations of the InGaN well. Local changes of the QW width and composition are, unlike to polar heterostructures, not expected to cause any changes in the out-of-plane electric field applied on the m -plane QW. However, segregation of In can still have an impact on the local band structure and thus affect optical properties as it is described in section 9.2.

A detailed structural investigation of the MQW region was also performed for the $[11\bar{2}0]$ cross-section using HRTEM. It was possible to observe BSF penetrating the MQW stack as displayed in Figure 9.6 a). The HRTEM image was taken from a MQW sample with 10% In content. Note that in this imaging mode, QW and barrier layer show weak contrast and are thus not well resolved.

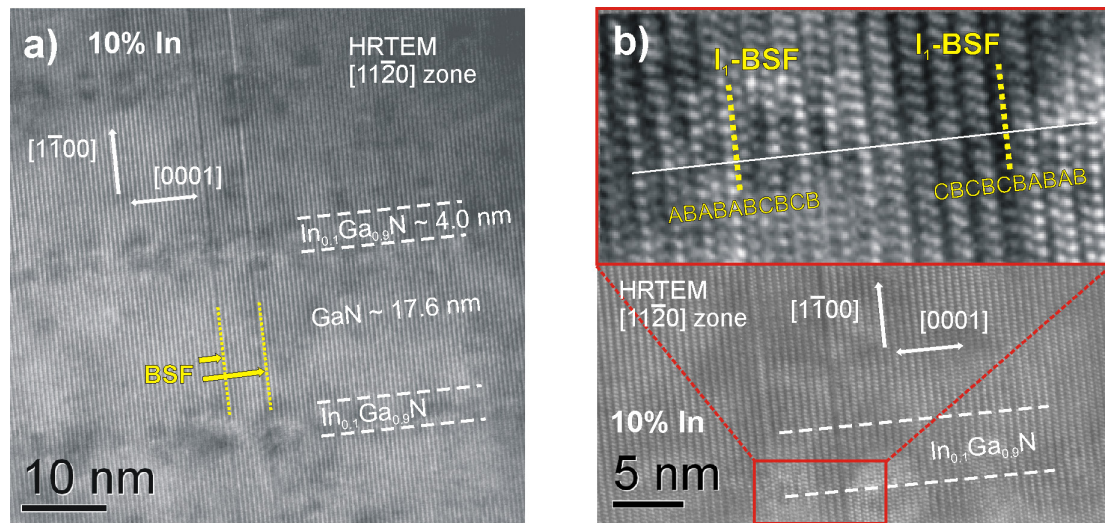


Figure 9.6: HRTEM images taken along the $[11\bar{2}0]$ cross-section of an m -plane $\text{In}_{0.1}\text{Ga}_{0.9}\text{N}/\text{GaN}$ MQW on LiAlO_2 . BSF visible in the overview in a) can be identified using an magnified and Fourier-filtered image shown in b). The solid white line in the upper part of b) is a guide to the eye to recognize the stacking sequence.

The BSF appear to be passing through the QW without any interaction. For an ambiguous determination of the defect type, a higher magnification is selected in Figure 9.6 b). The upper part of this figure indicates the detailed lattice structure in

the vicinity of the BSF at a QW-barrier interface. The distinctly changed stacking sequence is a direct evidence that these BSF are of I_1 -type. The identification of BSF in nonpolar InGaN-based MQW structures was only recently reported for the first time [172]. This paper describes the investigation of MQW grown on free-standing *m*-plane GaN substrates and points out that I_1 -type BSF may be generated in the MQW region if a high In content (26%) is chosen. The larger BSF density combined with an increased number of partial TD was also blamed responsible for reduced LED output power. The driving force for the generation of I_1 -type BSF in the MQW is most probably strain release. Another origin may be growth instabilities due to the reduced temperature, which is needed to achieve large In fractions. Our results are in this respect consistent to the literature report since no BSF generation within the MQW stack was observed for this sample having 10% In fraction.

Recapitulating the structural data, it was found that the growth of *m*-plane InGaN/GaN MQW on LiAlO₂ suffers from lower In incorporation efficiency compared to *c*-plane heterostructures. In spite of that, InGaN/GaN MQW with In fraction up to 30% could be realized, which exhibit reasonable structural and interface quality. Surface pits on the underlying GaN buffer, which are probably related to substrate imperfections, are enlarged during MQW deposition. This leads to the growth of InGaN wells on the tilted pit facets resulting in altered well/barrier thicknesses and probably also changed well composition. TD running at a 60° angle are penetrating the InGaN wells without bending or forming dislocation loops. However, they seem to increase either the In fraction or the well thickness. I_1 -type BSF intersect the MQW also without apparent annihilation or generation taking place for samples with In fractions up to 10%.

9.2 Optical characterization of InGaN/GaN MQW on LiAlO₂

9.2.1 RT photoluminescence characteristics

RT PL spectra have been taken from *m*-plane InGaN/GaN MQW samples with different In fractions. The results are displayed in Figure 9.7 a). Only the PL signal with polarization of $E \parallel [11\bar{2}0]$ is given here. Strong and sharp peaks with FWHM

values down to 120 meV are detected for In fractions of up to 10%, while for higher In concentration, the peaks are becoming much broader and reach FWHM of up to 252 meV for the sample with 30% In content. This sudden broadening of the emission may stem from a segregation of In-rich InGaN clusters at lower growth temperatures, which has also been reported to occur in *c*-plane quantum wells [173–175]. It should be mentioned that phase separation of InGaN is seen as a prerequisite for high recombination efficiency in InGaN-based LED because such clusters allow for the recombination of localized carriers without the detrimental influence of line defects in the material [176]. However, In-rich material may also very well be deposited on the tilted facets of the surface pits, which were observed in Figure 9.4. Enhanced In incorporation near surface defects has also been reported for *a*-plane InGaN-based MQW [177].

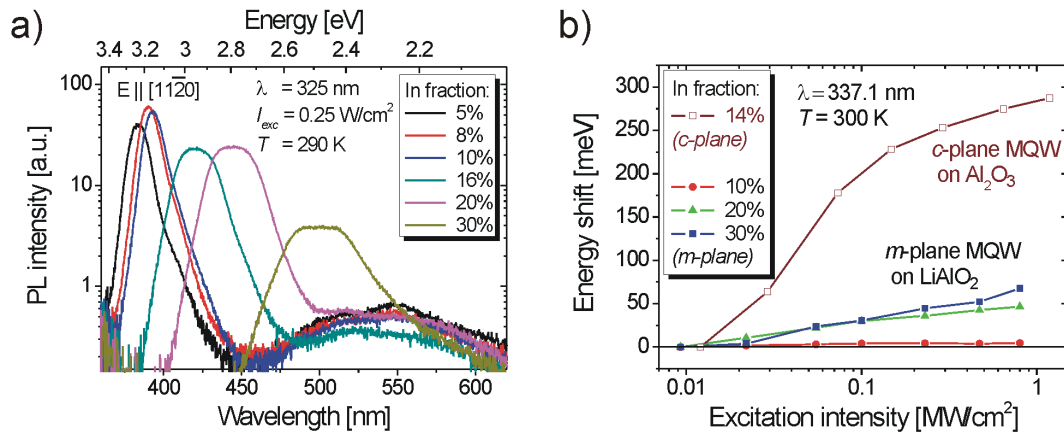


Figure 9.7: a) RT PL spectra for an m-plane InGaN/GaN MQW. b) Peak energy shift for selected In fractions in comparison to a c-plane InGaN/GaN MQW reference.

It is also well known that BSF induce a QW-like potential energy confinement in GaN films and thus lead to additional localization in AlGaN/GaN MQW structures [178]. However, studies of this mechanism in the InGaN/GaN system and its effect on the radiative and non-radiative recombination mechanisms are yet lacking. Note that the expected potential difference of a BSF-induced QW state within the InGaN well can be assumed to be close to the one for GaN (~ 100 meV [44]) and should be

roughly constant for different In fractions. The emission peak for the lowest In fraction in Figure 9.7 a) exhibits a shoulder on the low-energy side, which according to its energetic distance to the main InGaN peak may be related to such a luminescence caused by BSF penetrating the QW. For MQW samples with In fraction above 10%, this BSF emission may gain one order of magnitude in intensity and substantially contribute to the emission broadening. This would require a sudden increase of the BSF density during the deposition of MQW structures with In fractions larger than 10%, which could not be verified in this study. Another possibility would be that the weak BSF emission from additional confinement in the MQW is superimposed by the peak broadening, which stems from In segregation in samples with high In content.

Intensity-dependent PL gives further evidence for a segregation process. Figure 9.7 b) exemplarily summarizes the resulting energy shifts for three *m*-plane InGaN/GaN MQW with different In contents and one *c*-plane reference MQW with similar stacking sequence and 14% In content grown on Al₂O₃. The excitation intensity was varied by two orders of magnitude and only the emission with $E \parallel [11\bar{2}0]$ was taken into account for the nonpolar MQW samples. One can easily recognize that for low amounts of incorporated In (10%), the peak shift is totally negligible. This proves the absence of the QCSE and is consistent with earlier reports on *m*-plane InGaN/GaN MQW [179, 180]. However, a small but distinct peak shift towards higher energy is present for the *m*-plane MQW with 20% and 30% In and appears to be larger for samples with higher In fraction. As expected, this shift is much lower compared to the one found for a comparable *c*-plane MQW structure, which is displayed for reference in Figure 9.7 b). The origin of the PL band shift for the high-In-fraction *m*-plane MQW is obviously related to the filling of deep energy states (band tails) due to potential fluctuations. This explanation was also given for the even higher wavelength shifts, which were reported for semipolar InGaN-based yellow-emitting LED [181]. Even for high-quality blue *m*-plane InGaN-based LED, peak shifts in the range of 10 - 40 meV are a common observation [182]. If one assumes clustering of In within the QW plane, the QCSE might of course be present along the *c*-axis direction. It is very difficult to quantify the impact of this effect on optical properties since graded compositions have to be considered. Anyway, the concentration gradient of stacked well/barrier pairs can be expected to be much higher compared to the one caused by

segregation of In. The polarization differences are therefore probably very low and can be neglected.

A very important question arises regarding to the position of In-rich regions within the QW. The segregation of In may preferentially take place near line defects since some evidence for such a mechanism was already provided in Figure 9.5 b). Assuming that these line defects trigger nonradiative recombination processes, a clustering of In at defects would of course be highly disadvantageous for the efficiency of an LED. The reduced RT PL intensity for MQW with In fractions above 10% observed in Figure 9.7 a) may be taken as a first indication for reduced recombination efficiency due to clustering or defect generation. Further studies are required to clarify this issue.

9.2.2 Temperature-resolved photoluminescence

The clustering mechanism is also reflected in temperature-dependent PL data. Figure 9.8 a) displays the relative temperature-induced shift of the emission energies (with $E \parallel [11\bar{2}0]$) for the *m*-plane InGaN/GaN MQW samples. The peak emission energy at 10 K was taken as a reference. The theoretical Varshni bandgap energy shift for an $\text{In}_{0.15}\text{Ga}_{0.85}\text{N}$ layer derived by a linear interpolation between the data for GaN and InN is also displayed for comparison [183]. With the exception of the MQW structure grown with 30% In fraction, all samples feature a stronger emission energy red-shift below $T = 110$ K compared to the interpolated Varshni behaviour. This energetic difference is reduced at higher temperatures leading to an S-shaped trend. The temperatures at which the energy shift becomes weaker seem to increase with In fraction of the QW and are denominated as T_{escape} . The phenomenon hints on a charge carrier localization effect as it is known for *c*-plane MQW [184, 185]. While carriers are confined at local potential minima sites within the QW for $T < T_{\text{escape}}$, an increase of temperature allows them to escape the minima and occupy higher-energy levels.

Usually, the characteristic localization escape temperatures in *c*-plane MQW are well below 150 K [184, 185]. The higher values for *m*-plane InGaN MQW may be explained by stronger localization. However, short radiative recombination times due to the absence of the out-of-plane QCSE or due to defects can also reduce the thermal redistribution of carriers, which leads to higher measured values for T_{escape} .

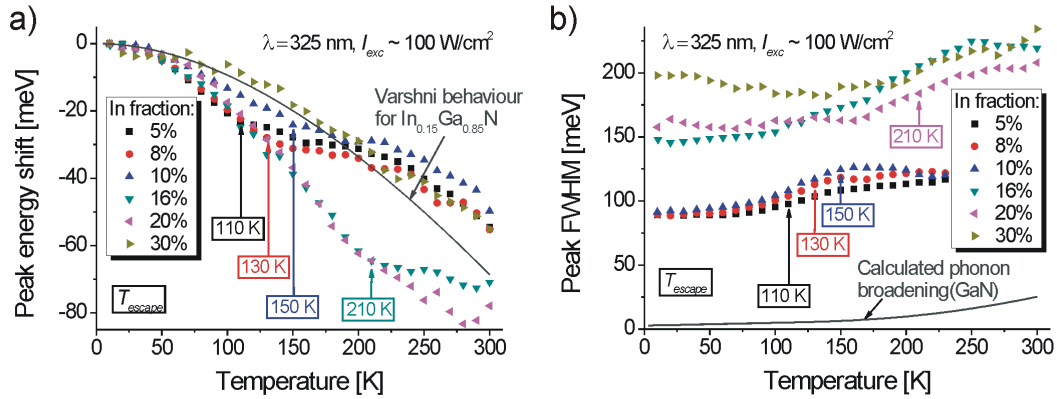


Figure 9.8: Temperature dependence of PL InGaN a) peak shift and b) FWHM. The Varshni temperature dependence of the bandgap energy for $\text{In}_{0.15}\text{Ga}_{0.85}\text{N}$ and the theoretical broadening by phonon interaction for GaN are also included.

Note that the S-shape of the peak energy temperature dependence is completely suppressed for very high excitation intensity ($I_{\text{exc}} = 300 \text{ kW/cm}^2$). This is easily understood by the saturation of localization centres and a dominating contribution from the non-localized InGaN QW emission. For the samples with 20% and 30% In content, the respective temperatures are impossible to define exactly because of data scattering and the lack of data points above 300 K. It cannot be excluded that the PL signal of these MQW originates only from strongly localized sites and all redistribution processes are effectively suppressed up to 300 K for this sample.

Figure 9.8 b) shows the development of the PL peak width against temperature for the *m*-plane MQW samples. For comparison, the line width broadening based on acoustical and optical phonon interaction of a GaN peak is also included [186]. Similar to the RT PL data, a sudden enlargement of the 10 K peak width from $\sim 90 \text{ meV}$ to $\sim 150 \text{ meV}$ can be found when the In fraction is increased above 10%. The temperature dependence of the measured FWHM values strongly differs to the phonon interaction broadening of GaN regarding its absolute magnitude and trend. When the temperature of the PL measurement approaches the characteristic temperature T_{escape} , charge carriers redistribute between localization sites. As a consequence, recombination with different energies occurs, thus enlarging the FWHM of the emission peak [187]. For the MQW with In fraction of 20% and 30%, the respective

maximum would probably appear at $T > 300$ K and is therefore not observable in Figure 9.8 b). It is quite astonishing that hints to carrier localization appear already at a very low In fraction of only 5%. One has to note that the intensity-dependent PL data in Figure 9.7 b) do not supply evidence for strong In segregation in this sample. Yet, slight potential fluctuations due to local distortions in the InGaN well cannot be ruled out. Spatial strain inhomogeneities or defects in the GaN buffer layer may be an origin for such localization sites.

9.2.3 Determination of polarized emission and absorption behaviour

The possibility to achieve highly polarized emission is one of the key benefits for the deposition of nonpolar GaN-based heterostructures. Although several groups were able to demonstrate nonpolar or semipolar MQW and LED with high DoP values, little is known about the limiting factors for the achievement of high DoP ratios in InGaN-based MQW [188-191]. Beside of the general recommendation to minimize light scattering on the side facets of packaged LED [192], only a general trend of higher DoP with larger In content has been identified by several groups [191, 193, 194]. Similar to the polarized emission properties of *m*-plane GaN films, in-plane compressive strain induced by higher In fractions is known to enhance the DoP in *m*-plane InGaN/GaN MQW because of the increased energy separation of the valence subbands [195].

The confirmation of this theory is visible in Figure 9.9 a), which shows the measured DoP of the RT PL emission of the *m*-plane InGaN MQW on LiAlO₂. The PL signal was collected with an excitation wavelength of 337.1 nm at an intensity of 300 kW/cm². For comparison, reported DoP values of *m*-plane InGaN/GaN LED grown on free-standing GaN substrates are shown as well [193]. One can recognize a similar trend but significantly lower ratios in the given study. Polarization-resolved photocurrent (PC) absorption spectra have been taken by applying conductive silver contacts. This enables a reliable determination of the absolute energy difference of the T_1 and T_2 transition energies, which are displayed in Figure 9.9 a) as well [196]. Again, literature values are given as a reference [193]. The direct comparison reveals a large deviation of the energy separation, which is impossible to explain by compositional uncertainties or errors within the determination of the values for $(T_2 - T_1)$.

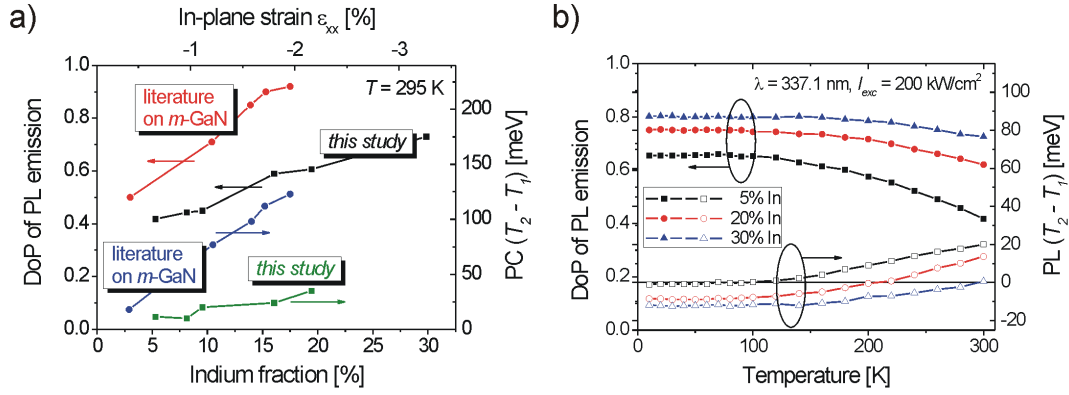


Figure 9.9: a) PL DoP and PC absorption spectra transition energy difference of valence subbands ($T_2 - T_1$) for different In fractions in the MQW. b) PL DoP and PL ($T_2 - T_1$) for different temperatures. The literature data in a) is taken from [193].

It is interesting to note that literature reports on *m*-plane InGaN/GaN LED on LiAlO₂ with an In fraction of 30% also specify an energy splitting of only 37 meV [197]. In this report, the discrepancy to the calculated value was ascribed to errors in the material parameters, which does not appear credible in view of the results achieved on free-standing *m*-plane GaN.

For a better understanding of the situation, the DoP and energy difference of the PL emission were also measured at various temperatures. The values are plotted in Figure 9.9 b) for samples with In fractions of 5%, 20%, and 30%. A higher In content results in a larger DoP in the whole temperature range. Further, a decline of the DoP is observed at elevated temperatures. This drop is weaker when more In is incorporated, which is again due to larger strain and thus higher energy separation between the valence subbands [195]. The valence subband separation was also investigated in the whole temperature range. Since PC absorption measurements at LT were impossible to carry out, the temperature-dependent energy separation was approximated by the energetic difference of the PL emission peaks with different polarization state. Although the energy differences determined from the PL data do not directly correspond to the exact values for ($T_2 - T_1$), a general trend for the temperature dependency can be found. The results for 5%, 20%, and 30% In are displayed in Figure 9.9 b) as well.

Similar to literature reports, an enlargement of the energetic difference with temperature increase is observed [190, 193]. However, the lowest In content exhibits the highest energetic difference of the PL peaks for all temperatures, which is in stark contrast to the PC absorption data. Moreover, the energy separation takes negative values at LT for all MQW, being more negative for larger In fractions. In other words, the PL component with $E \parallel [0001]$, which is denoted as T_2 transition, has a lower weighted mean photon energy while still being lower in intensity compared to the T_1 transition with $E \parallel [11\bar{2}0]$.

A possible explanation for the negative energy difference observed in PL measurements is related to the above described presence of band tails due to clustering of In. The effect can most easily be understood if one assumes the band structure at LT for which no thermal emission of holes takes place and thus only the HH valence subband is usually populated by holes. A schematic illustration of the spatial band diagram is given in Figure 9.10.

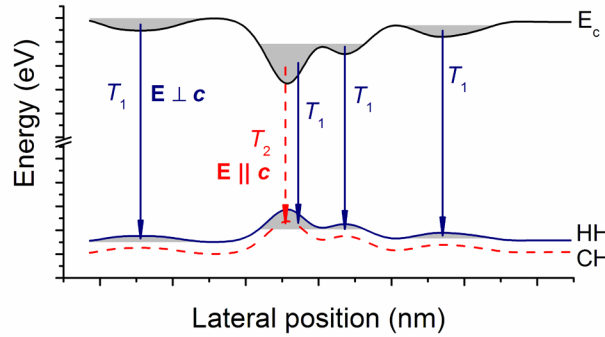


Figure 9.10: Schematic diagram of potential distribution of inhomogeneously composed InGaN. Accumulated carriers are visualized by grey areas.

Localization of carriers in In-rich regions may lead to a situation, in which also a band tail of the CH subband becomes occupied at LT. In this case, T_2 transitions would have in average lower photon energy compared to T_1 because the latter transition occurs predominantly from non-segregated InGaN regions or shallower clusters, both of which exhibiting unoccupied CH subband states. The PL component with $E \parallel [0001]$ is mainly formed by T_2 transitions, since the polarization selection

rules for this crystal orientation and compressive strain state prevent a strong contribution of T_1 [59]. Since this PL component with mostly T_2 transitions arises from deep localized states only, a red shift and eventually negative energy separation of the two polarization directions occur. For InGaN wells with more homogeneous composition, the CH valence subband would not be occupied at low temperatures. T_2 transitions are thus absent in this case and the emission with $E \parallel [0001]$ consists of the weak contribution of T_1 transitions only, which results in zero energy separation at LT as confirmed by the experiments of Kubota et al. [193].

Since band tails play a huge role for this special phenomenon, the effect is stronger if recombination processes are involved. The energetic differences extracted from PC absorption spectra are not affected to this large extent and therefore yield a different energy separation at RT. Lower values for the DoP compared to literature data are also explained by this mechanism because of a larger T_2 emission component from localized states. Stronger clustering at higher In fraction will enhance this effect and counteract the enhancement of the DoP caused by larger in-plane compressive strain.

In summary, the optical characterization shows strong and sharp RT PL peaks related to the MQW emission for samples containing low In fractions up to 10%. A sudden peak broadening takes place when more In was incorporated. This effect is most likely connected to an In segregation process, evidence for which is also found in intensity- and temperature-resolved PL data. The degree of polarization and subband energy separation follow the expected trend but the absolute values are lower compared to literature reports of *m*-plane InGaN/GaN MQW deposited on bulk GaN substrates. A theory was conceived, which again ascribes this effect to the In segregation mechanism.

9.3 Demonstration of *m*-plane InGaN/GaN-based LED

Since the QCSE is absent in *m*-plane InGaN/GaN MQW, higher recombination efficiency and improved performance of MQW-based LED can be expected. However, several peculiarities of *m*-plane GaN layers and *m*-plane InGaN MQW deposited on LiAlO₂ substrates have already been revealed. This section will show how these effects impact the electroluminescence (EL) characteristics of *m*-plane LED devices.

A schematic cross-section of the layer stack is given in Figure 9.11 a). The studied *m*-plane LED were grown on a $\sim 1.3 \mu\text{m}$ thick, unintentionally n-type doped *m*-plane GaN buffer layer. Similar to the *m*-plane InGaN MQW sample series described above, a 5-fold MQW was deposited with well and barrier thicknesses of 2.5 and 19.5 nm, respectively. The MQW surface temperature was set to 730°C resulting in an In fraction of 16%, which is consistent to the data in the inset of Figure 9.1 b). A 90 nm thick Mg-doped GaN layer was grown on top at 900°C , details on the Mg doping were given in section 7.5. LED devices have been processed from this wafer after thermal activation of the p-doped GaN layer for 15 min at 700°C . The processing included a partial dry etching of the layer stack down to the n-type conductive GaN layer using an ICP-RIE tool. The parameters of this 12 min step are specified in section 5 and resulted in an etching depth of 640 nm.

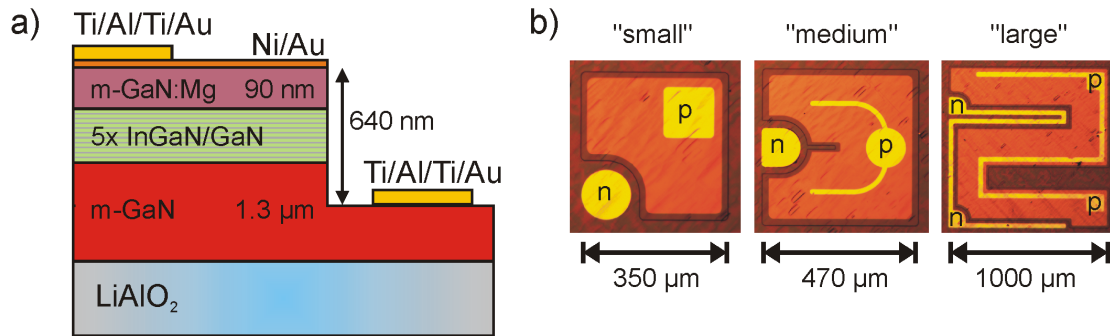


Figure 9.11: Layer stack (a) and different device layouts (b) of fabricated *m*-plane InGaN/GaN LED on LiAlO_2 . Metal p- and n-type contacts are labelled.

Three different layouts have been used resulting in mesa structures with lateral extensions of $350 \cdot 350 \mu\text{m}^2$ ("small"), $470 \cdot 470 \mu\text{m}^2$ ("medium"), and $1000 \cdot 1000 \mu\text{m}^2$ ("large"). A semi-transparent top p-type contact consisting of a Ni/Au stack with 5 and 20 nm thickness, respectively, was applied on top of the mesa surface. A Ti/Al/Ti/Au stack was used for local fortification of the p-type contact as well as for the lower n-type contact with respective metal thicknesses of 10/40/150/100 nm. Annealing of the p-type metal contact was performed for 10 min at 495°C in an open tube furnace under flowing N_2 . No n-type metal contact

annealing was done. A top view of the three different fabricated LED variants is displayed in Figure 9.11 b).

The quality of both contacts was characterized by circular transmission line method measurements. The specific resistivity of the n-type contact is $\sim 3.8 \cdot 10^{-7} \Omega\text{cm}^2$, which is comparable to values given in literature [198] and in good agreement to data extracted from typical *c*-plane GaN-based LED on sapphire and Si, which were grown and processed in the same lab. However, no contact resistivity for the p-type contact could be extracted because the *I-V* curves are only perfectly linear for absolute voltages below 1.3 V. Above this value, an exponential behaviour is observed indicating that the p-type contact area exhibits small regions with Schottky diode characteristics. One can ascribe this to the non-optimized Mg-doping and annealing procedure. The processed LED was probed on-wafer with an optical fiber connected to a spectrometer being placed a few mm above the device. Figure 9.12 a) shows the resulting electroluminescence spectrum for the smallest active area layout at a current of 70 mA corresponding to a current density of 829 mA/mm^2 .

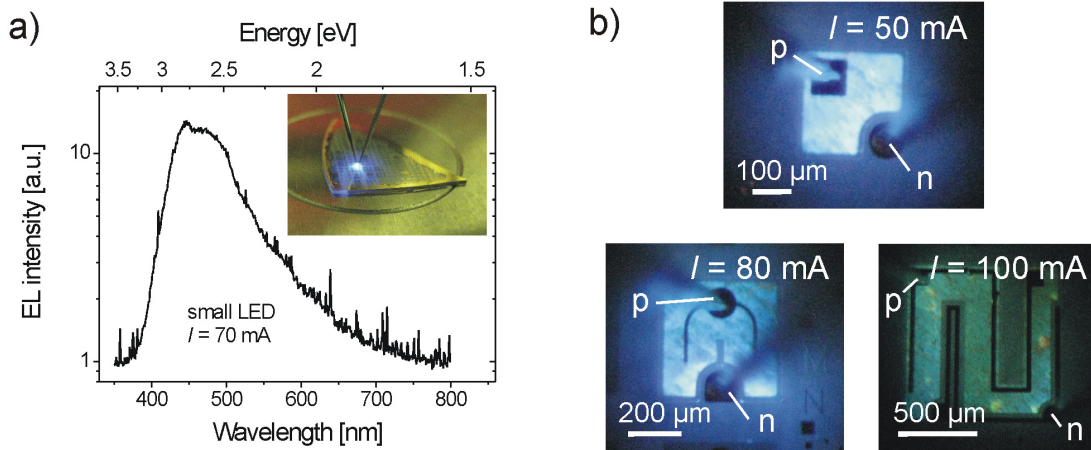


Figure 9.12: a) EL spectrum and photograph of EL operation of “small” m-plane GaN-based LED. b) Optical microscope images of all three LED types under EL operation.

The inset shows a photograph image of the operating LED. The EL spectrum shows a relatively broad emission in the blue-green spectral region. The peak can be separated

into at least two contributions, a sharper peak at 2.79 eV and a broader one at 2.63 eV. On the low-energy side of these peaks, the emission declines very gently. The peak positions deviate to the PL result of samples with equal MQW stack and In content, which exhibit a main peak at 2.95 eV. The high injected current density in the case of the EL experiment may cause a saturation of emission from band tails and would justify a peak shift towards higher energy, which is the opposite to what is observed here. Two effects can be blamed responsible for the difference between the EL and PL spectra: As for one, the PL experiment excites the barriers of the MQW as well. Since the diffusion length of carriers is very low in *m*-plane GaN, recombination may occur within GaN and contribute to a higher-energy emission wing of the PL peak. The second process is related to the surface pits on the GaN buffer, which the MQW structure was also deposited on. The triangular shape of the pits and the lower total MQW thickness cause locally higher electric fields and hence induce a higher current density. Since the incorporation of In on the facets is likely to be larger compared to planar growth, the emission energy from these pits will be reduced. Unlike to In clustering effects, the volume of the emitting material is in the order of 100 nm, so a saturation of emission with higher current will not readily occur. Optical microscope images of the differently sized devices under operation are depicted in Figure 9.12 b). One finds that the blue electroluminescence is modulated by the anisotropic features of the surface morphology. The “large” device could only be tested in a two-point contact scheme and is therefore hampered by insufficient current spreading. Especially in this large device with lower current density, some regions appear to show an intense green or orange emission. This may again be explained by very small domains with locally decreased MQW thicknesses and higher In content. The higher current density passing through these spots induces a punctually brighter emission. Furthermore, an altered light extraction from the tilted facets leads to an apparently larger luminescent spot size.

Unfortunately, neither intensity-dependent EL spectra nor optical output power P_{out} could be determined in this study. One can however estimate that the optical power at 50 mA is clearly below 1 mW. Further work is therefore required to improve the light output. It should be kept in mind that the efficiency of *m*-plane InGaN/GaN LED heavily relies on the design and optimization of the MQW stack itself. As one example, much thicker barrier widths were found beneficial for the optical output

power in *m*-plane InGaN/GaN LED, which is in stark contrast to standard *c*-plane InGaN LED [169, 182].

There are only two literature reports on *m*-plane InGaN/GaN LED on LiAlO₂. Dikme et al. demonstrated blue LED with $P_{out} = 45 \mu\text{W}$ at $I = 20 \text{ mA}$ and $V = 12 \text{ V}$ [199], while Liu et al. report on blue-green devices with $P_{out} = 80 \mu\text{W}$ at $I = 20 \text{ mA}$ and $V = 1.6 \text{ V}$ [200]. The extremely low forward voltage in the latter study raises doubts about their optical measurements since blue-green emission from InGaN cannot be expected for such a low bias. However, the shape of the I - V curve shown in this paper hints on parallel conduction paths in these devices. In contrast, the relatively large forward voltage of 12 V in the report of Dikme et al. can be explained by a large contact or series resistance [199].

The I - V characteristics of the *m*-plane LED fabricated in the given study are depicted in Figure 9.13 a) showing clearly diode-like behaviour for all active area layouts. This graph also includes the calculated current densities.

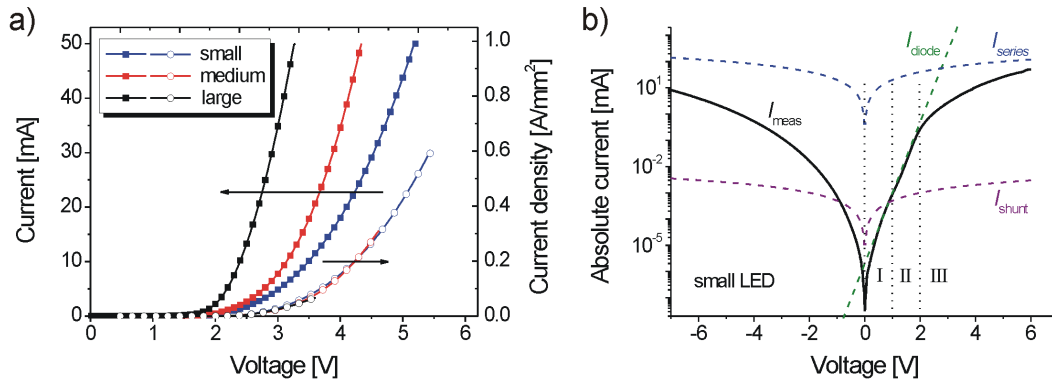


Figure 9.13: a) Current and current density versus voltage for *m*-plane GaN-based LED for all three active area sizes. b) I - V curve in logarithmic scale for the smallest active area. The trends for some conduction mechanisms are schematically indicated.

They show a virtually equal development for all sizes, which indicates that the current is flowing through the bulk material and not via the edges of the etched structure. The current limit of the measurement tool is at 100 mA, which is the reason for the different voltage ranges of the curves. The LED forward voltage is typically defined

at a current of 20 mA for a device size of $350 \cdot 350 \mu\text{m}^2$ (corresponding to a current density of 237 mA/mm^2). A reasonable value of 4.1 V can be determined in our case, which is only slightly larger than commercially available blue-green LED on sapphire. However, similar to the reports of Liu et al, the turn-on behaviour is not very abrupt [200]. A strong contribution of parallel leakage current in the devices is hence expected. Several physical effects can contribute to current leakage in InGaN/GaN LED. A logarithmic plot of the I - V curve of the smallest LED device is given in Figure 9.13 b) to get an idea about the conduction mechanisms. Beside of the measured data, the I - V tendencies for current passing through a parallel (I_{shunt}) and series resistance (I_{series}) as well as for diode current (I_{diode}) are indicated. The measured I - V behaviour for positive bias can now be separated into three domains labelled as “I”, “II”, and “III”:

At low voltages up to 1 V (“I”), the current is identical to the one in reverse direction and therefore only caused by leakage, which mostly stems from I_{shunt} . The expected simple proportionality to V is not exactly fulfilled, so other leakage mechanisms like barrier tunnelling are obviously also present. Although the leakage current in reverse direction is roughly six times lower compared to the data of *m*-plane LED on LiAlO_2 presented by Liu et al., its absolute value is still very high [200]. The presence of parallel conduction paths is also a well-known phenomenon in *c*-plane InGaN-based LED structures, for which it has been found that pure screw-type dislocations can contribute to vertical current leakage in GaN films [201]. This result was verified by Cao et al., who correlated the presence of V-shaped pits, which are induced by screw dislocations, in LED structures to a lower surface potential and higher leakage current [202]. As discussed in chapter 7.3, the total threading dislocation density in the *m*-plane GaN layers on LiAlO_2 is not much larger compared to standard *c*-plane GaN films. However, a considerable number of larger surface pits, which has been found on the *m*-plane InGaN/GaN MQW samples (compare Figure 9.4), may substantially contribute to parallel conduction paths. As mentioned above, these pits seem to be originated from defects in the GaN buffer layer. A reduction of defect density in the *m*-plane GaN films can therefore assumed to be helpful to minimize vertical current leakage in the LED. An alternative route would be to alter the growth conditions for the MQW deposition to prevent the enlargement of surface pits.

In the interval of 1 - 2 V (“II”), the logarithmic curve becomes a straight line, which is not visible in reverse bias direction. This exponential dependency with V can be explained by a dominating contribution of I_{diode} . However, the built-in voltage of a blue LED is expected to be at ~ 3 V. It has already been mentioned that the p-type contact showed partly Schottky-like behaviour for voltages above 1.3 V. This exponential behaviour can thus be ascribed to the limitations of the non-optimized p-type doped material deposition and contact annealing. Although current flowing through the perimeter of the LED can behave like a parasitic diode as well, this possibility is ruled out here because of the identical I - V curves for all LED sizes (compare Figure 9.13 a)).

When increasing the voltage above 2 V (“III”), the curve already starts to saturate. This is easily explained by the limitations imposed by the series resistance of the device. The onset of this restriction starts at a rather low voltage and the curve shape does not exactly follow the tendency expected by a series resistor. Current crowding is known to affect the I - V characteristics in laterally driven LED near the turn-on voltage and is probably the reason for the early saturation and nonlinear dependency [203]. The effects of the series resistance and current crowding in domain III may be a consequence of the limited mobility and carrier concentration in the p-type GaN layer. Improving the electrical properties of this top contact layer can therefore be expected to further enhance the performance of the *m*-plane InGaN/GaN LED.

10 Summary and conclusion

The growth of GaN-based quantum wells (QW) with a nonpolar orientation is accepted as a highly promising approach to eliminate internal polarization fields and thereby improve the wavelength stability and efficiency of future optoelectronic devices such as light emitting diodes (LED). In this thesis, a comprehensive study on the metal organic vapour phase (MOVPE) deposition of *m*-plane GaN films and InGaN/GaN QW on the cost-effective substrate LiAlO₂ is presented for the first time.

The study led to several breakthroughs in the field of nonpolar GaN epitaxy. As for one, the importance of a nitridation step for the growth of high-quality *m*-plane GaN films on LiAlO₂ has been demonstrated. This enabled the achievement of much lower line and planar defect density values compared to other heteroepitaxially grown nonpolar GaN layers. For the first time, basal plane stacking faults (BSF) could be visualized and quantified by using electron channelling contrast imaging (ECCI). Moreover, important new insights regarding the correlation of structural, morphological and optical properties of *m*-plane InGaN multiple quantum wells have been obtained.

Looking at the results in detail, it could be shown that in spite of the limited stability of the LiAlO₂ substrate, MOVPE can still be effectively used to deposit phase-pure *m*-plane GaN films on top. One key step is the application of a proper nitridation step before growth. It was demonstrated that the exposure to NH₃ at elevated temperatures leads to the transformation of the top LiAlO₂ surface layer into a thin *m*-plane AlN film. This layer acts as protective sealing layer and enhances the stability of the substrate surface during nitride deposition, which leads to high-quality, phase-pure, and smooth *m*-plane GaN layers.

The low lattice mismatch to *m*-plane GaN is one of the main advantages of the LiAlO₂ substrate material. It allows for coherent growth of thin GaN layers with the mismatch being 1:1 transformed into in-plane compressive strain. This strain is only partially relaxed even for layer thicknesses up to 1.7 μm . The lack of a suitable glide plane is seen as one origin for this. The low substrate-lattice mismatch is also thought

of as the main reason for the relatively low densities of threading dislocations (TD) and basal plane stacking faults (BSF), which are in the order of $1 \cdot 10^9 \text{ cm}^{-2}$ and $1 \cdot 10^4 \text{ cm}^{-1}$, respectively, as found in X-ray diffraction (XRD), transmission electron microscopy (TEM), and electron channelling contrast imaging (ECCI) studies. The high material quality and low BSF density is confirmed by photoluminescence (PL) spectra showing a strong GaN donor-bound exciton (D_0X) emission and only weak defect-related peaks. Time-resolved high-excitation PL and transient carrier grating experiments yield bipolar carrier lifetimes of 40 ps for the *m*-plane GaN films on LiAlO_2 , which is in good agreement to only slightly higher values for free-standing *m*-plane GaN substrates grown on GaN/ LiAlO_2 templates.

The surface morphology of the *m*-plane GaN films is dominated by macroscopic hillocks and a striated pattern elongated in the GaN *c*-axis direction. The former leads to an increase of the average root mean square (RMS) surface roughness to values of $\sim 20 \text{ nm}$ and is probably caused by spiral growth around threading dislocations with a screw component. The latter leads to steps with average height of 2 - 3 nm and most likely stems from an anisotropic growth mode with larger in-plane growth rate along the *c*-axis. In contrast, the small-scale RMS roughness of the *m*-plane GaN films between the characteristic steps is $\sim 0.2 \text{ nm}$, which allows the visibility of step-flow monolayer terraces. As a consequence of the in-plane anisotropy during growth, a much stronger broadening in XRD Omega scans can be observed along the *a*-axis direction. The structural anisotropy can also be seen in the electron mobility, which is typically above $120 \text{ cm}^2/\text{Vs}$ for $\sim 1 \text{ }\mu\text{m}$ thick GaN films and exhibits on average by 13% larger values along the *c*-axis direction.

A very challenging issue for *m*-plane GaN epitaxy on LiAlO_2 is impurity incorporation. O was identified as main impurity with its typical concentration being in the order of $1 \cdot 10^{19} \text{ cm}^{-3}$. In contrast, Li is incorporated at a much lower level of $1 \cdot 10^{16} \text{ cm}^{-3}$. One origin of both impurities was traced back to substrate outgassing. However, the strong affinity to O of the *m*-plane GaN surface at the deposition temperature presumably plays a much more important role for the high impurity level. The O impurities correspond to a high n-type background doping, which can be compensated by relatively large amounts of Mg to achieve p-type conductivity.

The successful epitaxy of *m*-plane InGaN/GaN multiple QW (MQW) was demonstrated with reasonable structural and interfacial quality. Lower incorporation of In

for *m*-plane InGaN films in comparison to equally fabricated *c*-plane structures was observed, which is consistent to literature reports. InGaN MQW with In fractions ranging from 5 to 30% could yet be deposited by adjustment of the reactor temperature. If surface pits are present on the GaN buffer layer, they are enlarged during the MQW growth step with the wells and barriers being also deposited on the tilted facets of these pits. High resolution TEM studies show both TD and I₁-type BSF penetrating the MQW structure. Evidence for annihilation or generation these defects within the MQW stack could not be observed. However, TD running at a 60° angle appear to locally increase either the composition or thickness of the InGaN wells.

Strong room temperature (RT) PL emission ranging from blue to green is observed for the *m*-plane InGaN/GaN MQW with peak widths of 120 meV and 252 meV for In fractions of 10% and 30%, respectively. Clustering of In within the InGaN wells or an altered composition of wells deposited on the tilted pit facets are the most likely reasons for a strong broadening of the RT PL peak from MQW structures with In contents above 16%. Furthermore, while the *m*-plane MQW structures with In fractions below 16% exhibit excellent peak wavelength stability due to the absence of the quantum confined Stark effect (QCSE), a slight peak shift is observed for larger In content. This also hints on significant In segregation. A detailed optical characterization shows the presence of InGaN band tails pointing towards partial In clustering even for MQW samples with low In content. Defects or strain inhomogeneities within the *m*-plane GaN lattice are assumed responsible for this effect. The presence of band tails also strongly affects the polarization of emission by altering recombination processes from the two valence subbands. This results in a lower degree of polarization and a smaller energetic difference between E_2 and E_1 in comparison to literature data.

The operation of *m*-plane InGaN/GaN-based LED was successfully demonstrated. These blue LED were processed with low contact resistances and exhibit a reasonable forward voltage of 4.1 V and a fairly homogeneous light emission from the active surface area. Although these devices show less parallel leakage current compared to literature reports on *m*-plane LED grown on LiAlO₂, the issue of current flowing through parallel resistances and tunnelling through the barriers without recombining radiatively is still an important challenge for further device improvement. Both effects are obviously related to the presence of V-pits in the MQW region but may

also be a result of the non-optimized MQW design and growth process. In addition, the non-optimized p-type doping procedure limits the forward current and hence reduces the light output. Another issue is surely related to the still large defect density, which causes nonradiative recombination thus limiting the overall LED efficiency. Further advancements in the deposition process are required to assess the full potential of *m*-plane InGaN/GaN-based LED.

List of figures

Figure 1.1: Bandgap energy versus in-plane lattice constant for AlN, GaN and InN and their ternary alloys (no bowing assumed). The energy range of the visible spectrum is schematically depicted.	5
Figure 2.1: Crystal structure of GaN in a ball-and-stick model. Ga and N atoms are displayed as big green and small blue spheres, respectively.	9
Figure 2.2: Calculated spontaneous and piezoelectric polarization and interface charge density in an $\text{In}_x\text{Ga}_{1-x}\text{N}/\text{GaN}$ QW for different In contents (a) and schematic representation of polarization-induced interface charges in the layer stack (b).....	14
Figure 2.3: Simulated band diagram of a single $\text{In}_{0.2}\text{Ga}_{0.8}\text{N}/\text{GaN}$ QW with (a) and without (b) polarization in growth direction. A low (10^{14} cm^{-3}) mobile electron density was assumed. Band offsets are caused by the fixed polarization charge σ	15
Figure 3.1: a) Schematic view of dissociation process of an edge-type dislocation into two partial dislocations leaving an I_2 -BSF in between, which shifts one basal plane by $R = 1/3[1\bar{1}00]$. b) Comparison of the unfaulted wurtzite lattice and the crystal structure with I_1 -, I_2 -, and E-type BSF (after [40]).	19
Figure 3.2: a) Illustration of the electronic band structure near the Brillouin zone centre point Γ for unstrained wurtzite GaN at 300 K (after [58]). Comparison of the energy levels at Γ for c-plane GaN (b) and m-plane GaN (c) under compressive strain.	23
Figure 4.1: Arrangement of the GaN unit cells on the LiAlO_2 substrate visualized using a ball-and-stick model. The red, violet and blue shaded areas indicate possible nucleation sites for $(1\bar{1}00)$ m-plane and (0001) c-plane GaN.	31
Figure 5.1: Measurement configuration for high excitation PL (a) and for transient carrier grating experiments (b).	36
Figure 6.1: Photograph of surface of 300 nm thick GaN films on LiAlO_2 substrate after direct deposition using N_2 and H_2 carrier gas.	39
Figure 6.2: AFM surface scans of LiAlO_2 substrates with and without exposure to NH_3 before and after a 5 min water dip.	41
Figure 6.3: XRR spectra of both blank (open circles) and 5 min nitridated (open triangles) LiAlO_2 substrate. A simulation fit for a LiAlO_2 /surface layer heterostructure (red curve) is also displayed.	42
Figure 6.4: HRTEM image of the LiAlO_2 surface after 2 min exposure to NH_3 along the $[010]$ zone axis. Material interfaces are marked by dashed lines. The insets show the FFT patterns with and without indication of the crystal unit cells and directions.	43
Figure 6.5: a) Cross-section HRTEM image of a 5 min nitridated LiAlO_2 surface after prolonged exposure to the electron beam shown along the $[001]$ zone axis; b) and c)	

show the AlN/LiAlO ₂ interface along the [001] and [010] zone, respectively. Material boundaries are schematically visualized.	44
Figure 6.6: a) HRXRD 2Theta/Omega scans and b) XRC FWHM values for m-plane GaN films with different nitridation times. The dashed line in a) shows the nominal position of strain-free m-plane GaN. The illustration in the upper right corner of b) indicates the alignment of the probe beam with respect to the m-plane GaN crystal.	46
Figure 6.7: a) RT PL spectra and b-c) AFM scans for m-plane GaN layers with 0 s and 300 s nitridation step before growth.	47
Figure 7.1: a) Standard deposition process for m-plane GaN films using the 3-step technique including nitridation (N), sealing layer (S), and main layer growth (G). b) Resulting layer stack.	50
Figure 7.2: Surface temperature and reflectivity of m-plane GaN films grown with a) 2 min nitridation step at 890 °C and b) 8 min nitridation step starting at 500 °C. Reflectivity datasets are vertically shifted for clarity.	51
Figure 7.3: AFM images of m-plane GaN surface using a scan area of a) 50 · 50 μm ² and b) 2 · 2 μm ² . The crystal directions are schematically visualized.	52
Figure 7.4: AFM images of m-plane GaN films grown with a V/III ratio of a) 1010 and b) 2020. The crystal directions are schematically visualized.	54
Figure 7.5: Symmetric (1 $\bar{1}$ 00) XRC spectra of a 0.9 μm thick m-plane GaN film for two incident X-ray beam directions. The illustration in the upper right corner indicates the alignment of the probe beam with respect to the m-plane GaN crystal.	56
Figure 7.6: a) XRD reciprocal space maps of a 0.9 μm thick m-plane GaN film for the (2 $\bar{2}$ 00) and (3 $\bar{3}$ 00) reflection measured with incident beam direction coplanar to [0001]. b) Extracted Q _x scans at the peak maximum.	58
Figure 7.7: a) Symmetric (1 $\bar{1}$ 00) GaN XRC FWHM along two incident beam directions and b) measured strain in m-plane GaN films for different film thicknesses.	59
Figure 7.8: TEM cross-section images of a 1.4 μm GaN film on LiAlO ₂ taken along the [1 $\bar{1}$ 2 0] zone using dark-field conditions. The diffraction vector g was chosen as a) [0002] and b) [1 $\bar{1}$ 00]. Distinguished defect types are marked.	61
Figure 7.9: TEM cross-section images of a 1.4 μm GaN film on LiAlO ₂ taken along the [0001] zone using dark-field conditions. The diffraction vector g was chosen as a) [1 $\bar{1}$ 00] and b) [1 $\bar{1}$ 2 0]. Distinguished defect types are marked.	63
Figure 7.10: ECCI from a 0.9 μm thick m-plane GaN film using 5 min nitridation. Yellow circles mark the position of BSF. The magnification in the lower left corner highlights the surrounding partial dislocations.	64
Figure 7.11: a) LT and RT PL spectra for 0.9 μm thick m-plane GaN film grown on 8 min nitridated LiAlO ₂ . The LT spectrum is shifted vertically for clarity. b) LT PL spectrum of 1.7 μm thick m-plane GaN with 5 min nitridation for emission polarization parallel and perpendicular to the GaN c-axis.	66
Figure 7.12: a) Development of the PL NBE peak position and its DoP with temperature. b) Valence subband energy separation and T ₁ absorption edge at RT for various film	

thicknesses. The dashed line represents the respective values for unstrained GaN [21, 61]. The solid line is a guide for the eye.	68
Figure 7.13: a) Excitation-dependent RT PL spectra of an m-plane GaN film. b) Integrated PL intensity plotted against excitation level for m-plane and c-plane GaN. The solid lines and vertical arrows indicate the proportionality of the PL intensity and the SE threshold, respectively.	70
Figure 7.14: Diffraction efficiency of transient grating in m-plane and c-plane GaN films for a) excitation-dependent and b) time-resolved measurements. Vertical arrows mark the onset of SE.	71
Figure 7.15: RT electron concentration and in-plane electron Hall mobility measured along the two in-plane crystal axes of m-plane GaN films with different thicknesses.	74
Figure 8.1: SIMS depth profiles of m-plane GaN on LiAlO ₂ . a) Qualitative profiling of Ga-N and C-N and quantitative analysis of O concentration in a 1.6 μm GaN film using Ar sputter gas; b) Quantitative Li detection in a 0.9 μm GaN film using O sputter gas. The inset shows the Li-implanted calibration sample.	77
Figure 8.2: LT PL spectra of c-plane GaN films grown with and without co-loaded LiAlO ₂ . The inset shows a magnification of the GaN exciton emission peaks.	80
Figure 8.3: SIMS depth profiles of m-plane GaN film for O measured using Ar sputter gas and Li measured using O sputter gas. The position of growth interruption and metal deposition on the substrate backside is marked by dashed lines.	81
Figure 9.1: Measured and simulated HRXRD symmetrical 2Theta/Omega scans for a) c-plane and b) m-plane InGa _{0.1} N/GaN MQW grown at equal conditions. The inset of b) shows the dependency of In content on the surface temperature for m-plane MQW.	84
Figure 9.2: HRXRD RSM of a) (3̄ 1̄ 0) and b) (2̄ 0 3) reflection of an m-plane In _{0.1} Ga _{0.9} N/GaN MQW. The arrows indicate the peak position of GaN and the MQW SL oscillations.	85
Figure 9.3: AFM images of m-plane InGa _{0.1} N/GaN MQW on LiAlO ₂ with In fractions of a) 5% and b) 30%. The crystal directions are schematically visualized.	86
Figure 9.4: Pits on the m-plane InGa _{0.1} N/GaN MQW surface visualized by a) plan-view SEM and cross-section TEM for b) 10% and c) 20 % In content. The MQW region and crystal directions with respect to the surface are also indicated.	87
Figure 9.5: Cross-section TEM images of an m-plane In _{0.2} Ga _{0.8} N/GaN MQW on LiAlO ₂ taken along the [0001] zone in a) overview and b) close-up view showing local QW fluctuations as marked by red circles.	88
Figure 9.6: HRTEM images taken along the [11̄ 2̄ 0] cross-section of an m-plane In _{0.1} Ga _{0.9} N/GaN MQW on LiAlO ₂ . BSF visible in the overview in a) can be identified using an magnified and Fourier-filtered image shown in b). The solid white line in the upper part of b) is a guide to the eye to recognize the stacking sequence.	89
Figure 9.7: a) RT PL spectra for an m-plane InGa _{0.1} N/GaN MQW. b) Peak energy shift for selected In fractions in comparison to a c-plane InGa _{0.1} N/GaN MQW reference.	91

Figure 9.8: Temperature dependence of PL InGaN a) peak shift and b) FWHM. The Varshni temperature dependence of the bandgap energy for $\text{In}_{0.15}\text{Ga}_{0.85}\text{N}$ and the theoretical broadening by phonon interaction for GaN are also included.	94
Figure 9.9: a) PL DoP and PC absorption spectra transition energy difference of valence subbands $T_2 - T_1$ for different In fractions in the MQW. b) PL DoP and PL $T_2 - T_1$ for different temperatures. The literature data in a) is taken from [193].	96
Figure 9.10: Schematic diagram of potential distribution of inhomogeneously composed InGaN. Accumulated carriers are visualized by grey areas.	97
Figure 9.11: Layer stack (a) and different device layouts (b) of fabricated m-plane InGaN/GaN LED on LiAlO_2 . Metal p- and n-type contacts are labelled.	99
Figure 9.12: a) EL spectrum and photograph of EL operation of “small” m-plane GaN-based LED. b) Optical microscope images of all three LED types under EL operation.	100
Figure 9.13: a) Current and current density versus voltage for m-plane GaN-based LED for all three active area sizes. b) I-V curve in logarithmic scale for the smallest active area. The trends for some conduction mechanisms are schematically indicated.	102

List of tables

Table 2.1: Selected group III nitride material parameters at $T = 300$ K.....	8
Table 2.2: Elastic constants for GaN, AlN and InN.	12
Table 3.1: Stacking and displacement vector of BSF types [41].....	20
Table 3.2: Hole effective masses for heavy-, light-, and crystal field split-off band along the directions parallel and perpendicular to the c-axis [57].....	25
Table 4.1: Properties of substrates for nonpolar GaN epitaxy at $T = 300$ K. All values refer to the orientation with respect to the GaN c-axis.	29
Table 7.1: XRC FWHM, $\Delta\omega_{\text{mos}}$, and LCL for a $0.9\text{ }\mu\text{m}$ thick m-plane GaN film on LiAlO_2 with 8 min nitridation time measured along both in-plane crystal directions.....	57
Table 8.1: XRC FWHM and RT Hall results for c-plane GaN films with and without a co- loaded piece of LiAlO_2	79

List of abbreviations

AFM	atomic force microscopy
Al_2O_3	aluminium oxide (sapphire)
a_{lay}	in-plane lattice constant of layer
a_{sub}	in-plane lattice constant of substrate
α	thermal expansion coefficient
AlGaInN	aluminium gallium indium nitride
AlGaN	aluminium gallium nitride
AlN	aluminium nitride
AlON	aluminium oxy-nitride
Ar	argon
b	Burgers vector
BE	bound exciton
BSF	basal plane stacking fault
C	carbon
C_{ij}	elastic constant
CB	conduction energy band
CCD	charge coupled detector
CH	crystal field split-off band
Cp_2Mg	Biscyclopentadienylmagnesium
D	electric displacement field
D_{adatom}	lateral adatom diffusion coefficient
D_0X	donor bound exciton
DoP	degree of polarization of emission
$\Delta\omega_{\text{mos}}$	mosaic tilt
E	electric field
$E_{1/2/3}$	transition energy from valence subbands to conduction band (c -plane GaN)
E_A	activation energy
E_C	conduction band energy
ε	lattice strain
ε_0	vacuum permittivity

EL	electroluminescence
ECCI	electron channelling contrast image
E_g	bandgap energy
ELOG	epitaxial lateral overgrowth
E_V	valence band energy
FE	free exciton
FFT	fast Fourier transformation
FWHM	full width at half maximum
FWM	four wave mixing
g	diffraction vector
Ga	gallium
GaAs	gallium arsenide
GaN	gallium nitride
GaP	gallium phosphide
H/H ₂	hydrogen
H ₃ PO ₄	phosphoric acid
HeCd	helium cadmium laser
HH	heavy hole valence subband
HRTEM	high-resolution transmission electron microscopy
HRXRD	high-resolution X-ray diffraction
HVPE	hydride vapour phase epitaxy
θ	Bragg diffraction angle
IDB	inversion domain boundary
I	current
I_{exc}	optical excitation power density
ICP-RIE	inductively coupled plasma reactive ion etching
In	indium
InGaN	indium gallium nitride
InN	indium nitride
$I_{ } / I_{\perp c}$	intensity with polarization parallel and perpendicular to the GaN c -axis
IQE	internal quantum efficiency
k_B	Boltzmann constant
k, k_x, k_z	wavenumber of charge carriers
l	dislocation line vector

A	free electron grating period
λ	wavelength (light, X-ray)
LASER	light amplification by stimulated emission of radiation
LCL	lateral coherence length
LD	laser diode
LED	light emitting diode
LH	light hole valence subband
Li	lithium
LiAlO_2	lithium aluminium oxide
LiAl_5O_8	lithium aluminium oxide
LiO_2	lithium oxide
LT	low temperature
m	lattice mismatch
m^*	effective charge carrier mass
m_0	free electron mass
μ	carrier mobility
MBE	molecular beam epitaxy
Mg	magnesium
MOVPE	metal organic vapour phase epitaxy
MQW	multiple quantum well
N/N_2	nitrogen
NBE	near band edge emission
N_{exc}	optically excited carrier density
N_{TD}	threading dislocation density
O	oxygen
PL	photoluminescence spectroscopy
P_{pz}	piezoelectric polarization
P_{sp}	spontaneous polarization
q	elementary charge
QCSE	quantum-confined Stark effect
QW	quantum well
Q_x	in-plane reciprocal space coordinate
Q_z	out-of-plane reciprocal space coordinate
R	defect displacement vector
ρ	mass density

RLP	reciprocal lattice point
RMS	root mean square
RT	room temperature
σ	lattice stress
σ_{int}	fixed interface charge density
SE	stimulated emission
SEM	secondary electron microscopy
Si	silicon
SiC	silicon carbide
SiH ₄	silane
SIMS	secondary ion mass spectrometry
SL	superlattice
SMB	stacking mismatch boundary
T	temperature
T_g	growth temperature
$T_{1/2/3}$	transition energy from valence subbands to conduction band (<i>m</i> -plane GaN)
τ	bipolar carrier lifetime
τ_G	free electron grating decay time
TD	threading dislocation
TEM	transmission electron microscopy
T_{escape}	localization escape temperature
TEGa	Triethylgallium
TMGa	Trimethylgallium
TMIn	Trimethylindium
t_{scat}	mean scattering time
UV	ultraviolet
V	voltage
VB	valence energy band
XRC	X-ray rocking curve
XRD	X-ray diffraction
XRR	X-ray reflectivity
YAG:Nd ³⁺	neodymium-doped yttrium aluminium garnet
YL	yellow luminescence

References

- [1] H. J. Round, *Elect. World* 19 (1907) 309.
- [2] H. Amano, M. Kito, K. Hiramatsu, I. Akasaki, *Jpn. J. Appl. Phys.* 28 (1989) L2112.
- [3] S. Nakamura, T. Mukai, M. Senoh, *Jpn. J. Appl. Phys.* 30 (1991) L1998.
- [4] S. Nakamura, *Science* 281 (1998) 956.
- [5] S. D. Lester, F. A. Ponce, M. G. Craford, D. A. Steigerwald, *Appl. Phys. Lett.* 66 (1995) 1249.
- [6] J. S. Speck, S. J. Rosner, *Physica B* 273-274 (1999) 24.
- [7] website: http://www.cree.com/press/press_detail.asp?i=1304945651119
- [8] A. Avramescu, T. Lerner, J. Iler, C. Eichler, G. Bruederl, M. Sabathil, S. Lutgen, U. Strauss, *Appl. Phys. Express* 3 (2010) 061003.
- [9] A. D. Bykhovski, V. V. Kaminski, M. S. Shur, Q. C. Chen, M. A. Khan, *Appl. Phys. Lett.* 68 (1995) 818.
- [10] A. D. Bykhovski, V. V. Kaminski, M. S. Shur, C. Chen, M. A. Khan, *Appl. Phys. Lett.* 69 (1996) 3254.
- [11] T. Takeuchi, S. Sota, M. Katsuragawa, M. Komori, H. Takeuchi, H. Amano, I. Akasaki, *Jpn. J. Appl. Phys.* 36 (1997) L382.
- [12] Y. Yamane, K. Fujiwara, J. K. Sheu, *Appl. Phys. Lett.* 91 (2007) 073501.
- [13] M.-H. Kim, M. F. Schubert, Q. Dai, J. K. Kim, E. F. Schubert, J. Piprek, Y. Park, *Appl. Phys. Lett.* 91 (2007) 183507.
- [14] P. Waltereit, O. Brandt, A. Trampert, H. T. Grahn, J. Menninger, M. Ramsteiner, M. Reiche, K. H. Ploog, *Nature* 406 (2000) 865.
- [15] M. Marezio, *Acta Crystallographica* 19 (1965) 396.
- [16] M. M. C. Chou, P. C. Tsao, H. C. Huang, *J. Cryst. Growth* 292 (2006) 542.
- [17] Y. J. Sun, O. Brandt, U. Jahn, T. Y. Liu, A. Trampert, S. Cronenberg, S. Dhar, K. H. Ploog, *J. Appl. Phys.* 92 (2002) 5714.
- [18] Y. Dikme, P. van Gemmern, B. Chai, D. Hill, A. Szymakowski, H. Kalisch, M. Heuken, R. H. Jansen, *Phys. Status Solidi (c)* 2 (2005) 2161.
- [19] Y. J. Sun, O. Brandt, B. Jenichen, K. H. Ploog, *Appl. Phys. Lett.* 83 (2003) 5178.
- [20] H. Behmenburg, T. C. Wen, Y. Dikme, C. Mauder, L. R. Khoshroo, M. M. C. Chou, M. V. Rzheutskii, E. V. Lutsenko, G. P. Yablonskii, J. Woitok, H. Kalisch, R. H. Jansen, M. Heuken, *Phys. Status Solidi (b)* 245 (2008) 893.
- [21] I. Vurgaftman, J. R. Meyer, L. R. Ram-Mohan, *J. Appl. Phys.* 89 (2001) 5815.

- [22] O. Ambacher, J. Phys. D: Appl. Phys. 31 (1998) 2653.
- [23] H. Iwanaga, A. Kunishige, S. Takeuchi, Journal of Materials Science 35 (2000) 2451.
- [24] K. Wang, R. R. Reeber, Appl. Phys. Lett. 79 (2001) 1602.
- [25] F. Bernardini, V. Fiorentini, D. Vanderbilt, Phys. Review B 63 (2001) 193201.
- [26] J. F. Nye, Physical Properties of Crystals, Oxford University Press, New York, 1964.
- [27] V. Fiorentini, F. Bernardini, O. Ambacher, Appl. Phys. Lett. 80 (2002) 1204.
- [28] website: <http://my.ece.ucsb.edu/mgrundmann/bandeng.htm>
- [29] K. H. Ploog, J. Cryst. Growth 237 (2002) 2028.
- [30] I. L. Lu, Y.-R. Wu, J. Singh, J. Appl. Phys. 108 (2010) 124508.
- [31] H. M. Ng, Appl. Phys. Lett. 80 (2002) 4369.
- [32] K.-C. Kim, M. C. Schmidt, H. Sato, F. Wu, N. Fellows, M. Saito, K. Fujito, J. S. Speck, S. Nakamura, S. P. DenBaars, Phys. Status Solidi (RRL) 1 (2007) 125.
- [33] K. Okamoto, J. Kashiwagi, T. Tanaka, M. Kubota, Appl. Phys. Lett. 94 (2009) 071105.
- [34] B. A. Haskell, F. Wu, S. Matsuda, M. D. Craven, P. T. Fini, S. P. DenBaars, J. S. Speck, S. Nakamura, Appl. Phys. Lett. 83 (2003) 1554.
- [35] B. A. Haskell, A. Chakraborty, F. Wu, H. Sasano, P. T. Fini, S. P. DenBaars, J. S. Speck, S. Nakamura, J. Elect. Mat. 34 (2005) 357.
- [36] Y. G. Seo, K. H. Baik, K.-M. Song, S. Lee, H. Yoon, J.-H. Park, K. Oh, S.-M. Hwang, Current Applied Physics 10 (2010) 1407.
- [37] X. J. Ning, F. R. Chien, P. Pirouz, J. W. Yang, M. A. Khan, J. Mater. Res. 11 (1996) 580.
- [38] J. P. Hirth, J. Lothe, Theory of Dislocations, 2nd ed., Wiley, New York, 1982.
- [39] T. Y. Liu, Ph.D dissertation, Humboldt-Universität zu Berlin, (2004).
- [40] W. Neumann, A. Mogilatenko, T. Wernicke, E. Richter, M. Weyers, M. Kneissl, Journal of Microscopy 237 (2010) 308.
- [41] C. Stampfl, C. G. Van de Walle, Phys. Review B 57 (1998) R15052.
- [42] T. Y. Liu, A. Trampert, J. Sun, O. Brandt, K. H. Ploog, Philos. Mag. Lett. 84 (2004) 435.
- [43] Y. T. Rebane, Y. G. Shreter, M. Albrecht, Phys. Status Solidi (a) 164 (1997) 141.
- [44] G. Salviati, M. Albrecht, C. Zanotti-Fregonara, N. Armani, M. Mayer, Y. Shreter, M. Guzzi, Y. V. Melnik, K. Vassilevski, V. A. Dmitriev, H. P. Strunk, Phys. Status Solidi (a) 171 (1999) 325.
- [45] X. Ni, Ü. Özgür, S. Chevtchenko, J. Nie, H. Morkoc, R. P. Devaty, W. J. Choyke, Proceedings of SPIE 6894 (2008) 689420.

- [46] R. Liu, A. Bell, F. A. Ponce, C. Q. Chen, J. W. Yang, M. A. Khan, Appl. Phys. Lett. 86 (2005) 021908.
- [47] P. P. Paskov, R. Schifano, T. Paskova, T. Malinauskas, J. P. Bergman, B. Monemar, S. Figge, D. Hommel, Physica B 376-377 (2006) 473.
- [48] P. Corfdir, P. Lefebvre, J. Levrat, A. Dussaigne, J.-D. Ganière, D. Martin, J. Ristic, T. Zhu, N. Grandjean, B. Deveaud-Plédran, J. Appl. Phys. 105 (2009) 043102-1.
- [49] T. Gühne, Z. Bougrioua, P. Vennéguès, M. Leroux, M. Albrecht, J. Appl. Phys. 101 (2007) 113101.
- [50] Z. H. Wu, A. M. Fischer, F. A. Ponce, B. Bastek, J. Christen, T. Wernicke, M. Weyers, M. Kneissl, Appl. Phys. Lett. 92 (2008) 171904.
- [51] J. E. Northrup, J. Neugebauer, L. T. Romano, Physical Review Letters 77 (1996) 103.
- [52] C. M. Drum, Philosophical Magazine 11 (1965) 313.
- [53] Z. Liliental-Weber, J. Cryst. Growth 310 (2008) 4011.
- [54] D. N. Zakharov, Z. Liliental-Weber, B. Wagner, Z. J. Reitmeier, E. A. Preble, R. F. Davis, Phys. Review B 71 (2005) 235334.
- [55] J. E. Northrup, Appl. Phys. Lett. 72 (1998) 2316.
- [56] L. Lymperakis, J. Neugebauer, Phys. Review B 79 (2009) 241308.
- [57] M. Suzuki, T. Uenoyama, A. Yanase, Phys. Review B 52 (1995) 8132.
- [58] website: <http://www.ioffe.ru/SVA/NSM/Semicond/GaN/index.html>
- [59] S. Ghosh, P. Waltereit, O. Brandt, H. T. Grahn, K. H. Ploog, Phys. Review B 65 (2002) 075202.
- [60] K. Domen, K. Horino, A. Kuramata, T. Tanahashi, Appl. Phys. Lett. 70 (1996) 987.
- [61] S. Ghosh, O. Brandt, H. T. Grahn, K. H. Ploog, Appl. Phys. Lett. 81 (2002) 3380.
- [62] J. Bhattacharyya, S. Ghosh, B. M. Arora, O. Brandt, H. T. Grahn, Appl. Phys. Lett. 91 (2007) 251913.
- [63] P. Misra, U. Behn, O. Brandt, H. T. Grahn, B. Imer, S. Nakamura, S. P. DenBaars, J. S. Speck, Appl. Phys. Lett. 88 (2006) 161920.
- [64] A. Sommerfeld, H. Bethe, Elektronentheorie der Metalle, Springer Verlag, Heidelberg, 1933.
- [65] Y. C. Yeo, T. C. Chong, M. F. Li, J. Appl. Phys. 83 (1997) 1429.
- [66] D. Fu, R. Zhang, B. Wang, Z. Zhang, B. Liu, Z. Xie, X. Xiu, H. Lu, Y. Zheng, G. Edwards, J. Appl. Phys. 106 (2009) 023714.
- [67] T. Hino, S. Tomiya, T. Miyajima, K. Yanashima, S. Hashimoto, M. Ikeda, Appl. Phys. Lett. 76 (2000) 3421.
- [68] D. Cherns, S. J. Henley, F. A. Ponce, Appl. Phys. Lett. 78 (2001) 2691.
- [69] I. Grzegory, J. Phys.: Condens. Matter 13 (2001) 6875.

- [70] D. Hanser, L. Liu, E. Preble, D. Thomas, M. Williams, *Mater. Res. Soc. Sym. Proc.* 798 (2004) Y2.1.1.
- [71] T. Hashimoto, F. Wu, J. S. Speck, S. Nakamura, *J. Cryst. Growth* 310 (2008) 3907.
- [72] T. Yamada, H. Yamane, H. Iwata, S. Sarayama, *J. Cryst. Growth* 286 (2006) 494.
- [73] R. Dwilinski, R. Doradzinski, J. Garczynski, L. Sierzputowski, R. Kucharski, M. Zajac, M. Rudzinski, R. Kudrawiec, J. Serafinczuk, W. Strupinski, *J. Cryst. Growth* 312 (2010).
- [74] K. Fujito, S. Kubo, H. Nagaoka, T. Mochizuki, H. Namita, S. Nagao, *J. Cryst. Growth* 311 (2009) 3011.
- [75] T. Onuma, T. Yamada, H. Yamane, S. F. Chichibu, *Appl. Phys. Express* 2 (2009) 091004.
- [76] M. Saito, H. Yamada, K. Iso, H. Sato, H. Hirasawa, D. S. Kamber, T. Hashimoto, S. P. DenBaars, J. S. Speck, S. Nakamura, *Appl. Phys. Lett.* 94 (2009) 052109.
- [77] H. P. Maruska, D. Hill, M. M. C. Chou, J. J. Challaigher, B. Chai, *Opto-Electron. Rev.* 11 (2003) 7.
- [78] H. Sasaki, H. Sunakawa, N. Sumi, K. Yamamoto, A. Usui, *J. Cryst. Growth* 311 (2009).
- [79] X. H. Wu, L. M. Brown, D. Kapolnek, S. Keller, B. Keller, S. P. DenBaars, J. S. Speck, *J. Appl. Phys.* 80 (1996) 3228.
- [80] A. G. Stern, D. C. Cole, *Proceedings of SPIE* 7153 (2008) 71530Z.
- [81] V. Cimalla, J. Pezoldt, O. Ambacher, *J. Phys. D: Appl. Phys.* 40 (2007) 6386.
- [82] M. M. C. Chou, H. C. Huang, D.-S. Gan, C. W. C. Hsu, *J. Cryst. Growth* 291 (2006) 485.
- [83] R. Armitage, H. Hirayama, 92 (2008) 092121.
- [84] J. F. Yan, L. W. Guo, J. Zhang, X. L. Zhu, G. J. Ding, Z. G. Xing, Z. T. Zhou, X. J. Pei, Y. Wang, H. Q. Jia, H. Chen, J. M. Zhou, *J. Cryst. Growth* 307 (2007) 35.
- [85] J. L. Hollander, M. J. Kappers, C. McAleese, C. J. Humphreys, *Appl. Phys. Lett.* 92 (2008) 101104.
- [86] T. S. Ko, T. C. Wang, R. C. Gao, H. G. Chen, G. S. Huang, T. C. Lu, H. C. Kuo, S. C. Wang, *J. Cryst. Growth* 300 (2007) 308.
- [87] Q. Sun, T.-S. Ko, C. D. Yerino, Y. Zhang, I.-H. Lee, J. Han, T.-C. Lu, H.-C. Kuo, S.-C. Wang, *Jpn. J. Appl. Phys.* 48 (2009) 071002.
- [88] B. Imer, F. Wu, J. S. Speck, S. P. DenBaars, *J. Cryst. Growth* 306 (2007) 330.
- [89] D. Iida, M. Iwaya, S. Kamiyama, H. Amano, I. Akasaki, *J. Cryst. Growth* 311 (2009) 2887.
- [90] M. McLaurin, T. E. Mates, F. Wu, J. S. Speck, *J. Appl. Phys.* 100 (2006) 063707.

- [91] Y. S. Cho, Q. Sun, I.-H. Lee, T.-S. Ko, C. D. Yerino, J. Han, B. H. Kong, H. K. Cho, S. Wang, *Appl. Phys. Lett.* 93 (2008) 111904.
- [92] A. Hirai, B. A. Haskell, M. McLaurin, F. Wu, M. C. Schmidt, K.-C. Kim, T. J. Baker, S. P. DenBaars, S. Nakamura, J. S. Speck, *Appl. Phys. Lett.* 90 (2007) 121119.
- [93] K.-C. Kim, M. C. Schmidt, F. Wu, M. McLaurin, A. Hirai, S. Nakamura, S. P. DenBaars, J. S. Speck, *Appl. Phys. Lett.* 93 (2008) 143108.
- [94] K. Kinoshita, J. W. Sim, J. P. Ackerman, *Materials Research Bulletin* 13 (1978) 445.
- [95] W. Gessner, D. Müller, *Z. anorg. allg. Chem.* 505 (1983) 195.
- [96] E. S. Hellman, Z. Liliental-Weber, D. N. E. Buchanan, *MRS Internet Journal of Nitride Semiconductor Research* 2 (1997) 30.
- [97] M. D. Reed, O. M. Kryliouk, M. A. Mastro, T. J. Anderson, *J. Cryst. Growth* 274 (2005) 14.
- [98] E. Richter, C. Hennig, U. Zeimer, M. Weyers, G. Tränkle, P. Reiche, S. Ganschow, R. Uecker, K. Peters, *Phys. Status Solidi (c)* 3 (2006).
- [99] C. Liu, Z. Xie, P. Han, B. Liu, L. Li, J. Zou, S. Zhou, L. H. Bai, Z. H. Chen, R. Zhang, Y. Zheng, *J. Cryst. Growth* 298 (2007) 228.
- [100] Y. J. Sun, O. Brandt, K. H. Ploog, *J. Vac. Sci. Technol.* 21 (2003) 1350.
- [101] C.-H. Hsieh, I. Lo, M.-H. Gau, Y.-L. Chen, M.-C. Chou, W.-Y. Pang, Y.-I. Chang, Y.-C. Hsu, M.-W. Sham, J.-C. Chiang, J.-K. Tsai, *Japan. J. Appl. Phys.* 47 (2008) 891.
- [102] A. Trampert, T. Y. Liu, O. Brandt, K. H. Ploog, *J. Phys. IV* 132 (2006) 221.
- [103] S. J. Beckerman, R. B. Ford, M. T. Nemeth, *Powder Diffr.* 11 (1996) 312.
- [104] J. Zou, Y. Dong, S. Zhou, Y. Sun, W. Jun, J. Zhou, T. Huang, S. Yang, H. Zhou, *J. Cryst. Growth* 294 (2006) 339.
- [105] J. Lin, Z. Wen, X. Xu, N. Li, S. Song, *Fusion Engineering and Design* 85 (2010) 1162.
- [106] M. M. C. Chou, S. J. Huang, C. W. C. Hsu, *J. Cryst. Growth* 303 (2007) 585.
- [107] B. Cockayne, B. Lent, *J. Cryst. Growth* 54 (1981).
- [108] A. Novoselov, A. Pajaczowska, *Crystal Research and Technology* 33 (1998) 949.
- [109] K. Xu, J. Xu, P. Deng, Y. Zhou, G. Zhou, R. Qiu, Z. Fang, *J. Cryst. Growth* 193 (1998) 127.
- [110] R. G. Wilson, B. L. H. Chai, S. J. Pearton, C. R. Abernathy, F. Ren, J. M. Zavada, *Appl. Phys. Lett.* 69 (1996) 3848.
- [111] B. Velickov, A. Mogilatenko, R. Bertram, D. Klimm, R. Uecker, W. Neumann, R. Fornari, *J. Cryst. Growth* 310 (2008) 214.
- [112] G. K. Williamson, W. H. Hall, *Acta Metallurgica* 1 (1953) 22.

- [113] T. Metzger, R. Höpler, E. Born, O. Ambacher, M. Stutzmann, R. Stömmer, M. Schuster, H. Göbel, S. Christiansen, M. Albrecht, H. P. Strunk, *Philosophical Magazine A* 77 (1998) 1013.
- [114] D. B. Williams, C. B. Carter, *Transmission Electron Microscopy*, 2nd ed., Springer, New York, 2009.
- [115] C. Trager-Cowan, F. Sweeney, P. W. Trimby, A. P. Day, A. Gholinia, N. H. Schmidt, P. J. Parbrook, A. J. Wilkinson, I. M. Watson, *Phys. Review B* 75 (2007) 085301.
- [116] R. Aleksiejunas, M. Sudzius, T. Malinauskas, J. Vaitkus, K. Jarasiunas, S. Sakai, *Appl. Phys. Lett.* 83 (2003) 1157.
- [117] A. Mogilatenko, W. Neumann, E. Richter, M. Weyers, B. Velickov, R. Uecker, *J. Appl. Phys.* 102 (2007) 023519.
- [118] K. Xu, J. Xu, P. Deng, R. Qiu, Z. Fang, *Phys. Status Solidi (a)* 176 (1999) 589.
- [119] Y. Goldberg, Aluminum Nitride (AlN), in: M.E. Levinshtein, S.L. Rumyantsev, M.S. Shur (Eds.) *Properties of Advanced Semiconductor Materials GaN, AlN, InN, BN, SiC, SiGe*, John Wiley & Sons, Inc., New York, 2001, pp. 31-47.
- [120] E. Schönherr, E. Schedler, *J. Cryst. Growth* 42 (1977) 289.
- [121] J. Jokinen, P. Haussalo, J. Keinonen, M. Ritala, D. Riihelä, M. Leskelä, *Thin Solid Films* 289 (1996).
- [122] S. Zollner, A. Konkar, G. R. B., S. R. Wilson, S. A. Nikishin, H. Temkin, *Mater. Res. Soc. Sym. Proc.* 572 (1999) Y5.21.
- [123] M. Bosund, T. Sajavaara, M. Laitinen, T. Huhtio, M. Putkonen, V.-M. Airaksinen, H. Lipsanen, *Applied Surface Science* 257 (2011) 7827.
- [124] K. Uchida, A. Watanabe, F. Yano, M. Kouguchi, T. Tanaka, S. Minagawa, *J. Appl. Phys.* 79 (1995) 3487.
- [125] J. W. Gerlach, A. Hofmann, T. Höche, F. Frost, B. Rauschenbach, G. Benndorf, *Appl. Phys. Lett.* 88 (2006) 011902.
- [126] E. Calleja, F. J. Sánchez, D. Basak, M. A. Sánchez-García, E. Munoz, I. Izpura, F. Calle, J. M. G. Tijero, J. L. Sánchez-Rojas, P. Beaumont, P. Lorenzini, P. Gibart, *Phys. Review B* 55 (1997) 4689.
- [127] C. Mauder, L. Rahimzadeh Khoshroo, H. Behmenburg, T. C. Wen, Y. Dikme, M. V. Rzheutskii, G. P. Yablonskii, J. Woitok, M. M. C. Chou, M. Heuken, H. Kalisch, R. H. Jansen, *J. Cryst. Growth* 310 (2008) 4976.
- [128] Y. S. Cho, H. Hardtdegen, N. Kaluza, R. Steins, G. Heidelberger, H. Lüth, *J. Cryst. Growth* 307 (2007) 6.
- [129] A. Hirai, Z. Jia, M. C. Schmidt, R. M. Farrell, S. P. DenBaars, S. Nakamura, J. S. Speck, *Appl. Phys. Lett.* 91 (2007) 191906.
- [130] R. M. Farrell, D. A. Haeger, X. Chen, C. S. Gallinat, R. W. Davis, M. Cornish, K. Fujito, S. Keller, S. P. DenBaars, S. Nakamura, J. S. Speck, *Appl. Phys. Lett.* 96 (2010) 231907.

- [131] P. Waltereit, O. Brandt, M. Ramsteiner, R. Uecker, P. Reiche, K. H. Ploog, *J. Cryst. Growth* 218 (2000) 143.
- [132] R. R. Vanfleet, J. A. Simmons, H. P. Maruska, D. W. Hill, M. M. C. Chou, B. Chai, *Appl. Phys. Lett.* 83 (2003) 1139.
- [133] B. Imer, F. Wu, M. D. Craven, J. S. Speck, S. P. DenBaars, *Jpn. J. Appl. Phys.* 45 (2006) 8644.
- [134] K. R. Wang, M. Ramsteiner, C. Mauder, Q. Wan, T. Hentschel, H. T. Grahn, H. Kalisch, M. Heuken, R. H. Jansen, A. Trampert, *Appl. Phys. Lett.* 96 (2010) 231914.
- [135] V. Jindal, F. Shahedipour-Sandvik, *J. Appl. Phys.* 107 (2010) 054907.
- [136] G.-S. Kim, J. S. Tse, D. D. Klug, *Chemical Physics Letters* 400 (2004) 74.
- [137] E. Penev, P. Kratzer, M. Scheffler, *Phys. Review B* 64 (2001) 085401.
- [138] T. Hoshi, K. Hazu, K. Ohshita, M. Kagaya, T. Onuma, K. Fujito, H. Namita, S. F. Chichibu, *Appl. Phys. Lett.* 94 (2009) 071910.
- [139] S. F. Chichibu, H. Yamaguchi, L. Zhao, M. Kubota, K. Okamoto, H. Ohta, *Appl. Phys. Lett.* 92 (2008) 091912.
- [140] T. Paskova, R. Kroeger, S. Figge, D. Hommel, V. Darakchieva, B. Monemar, E. Preble, A. Hanser, N. M. Williams, M. Tutor, *Appl. Phys. Lett.* 89 (2006) 051914-1.
- [141] M. McLaurin, A. Hirai, E. Young, F. Wu, J. S. Speck, *Jpn. J. Appl. Phys.* 47 (2008) 5429.
- [142] M. A. Moram, C. F. Johnston, J. L. Hollander, M. J. Kappers, C. J. Humphreys, *J. Appl. Phys.* 105 (2009) 113501.
- [143] M. A. Moram, J. C. Johnson, M. J. Kappers, C. J. Humphreys, *Physica B* 404 (2009) 2189.
- [144] I. Lo, C.-H. Hsieh, Y.-L. Chen, W.-Y. Pang, Y.-C. Hsu, J.-C. Chiang, M.-C. Chou, J.-K. Tsai, D. M. Schaadt, *Appl. Phys. Lett.* 92 (2008) 202106.
- [145] J. Neugebauer, C. G. Van de Walle, *Appl. Phys. Lett.* 69 (1996) 503.
- [146] G. A. Slack, L. J. Schowalter, D. Morelli, J. A. Freitas, *J. Cryst. Growth* 246 (2002) 287.
- [147] J. L. Lyons, A. Janotti, C. G. Van de Walle, *Appl. Phys. Lett.* 97 (2010) 152108.
- [148] R. Dingle, M. Ilegems, *Solid State Communications* 9 (1971) 175.
- [149] V. Y. Davydov, Y. E. Kitaev, I. N. Goncharuk, A. N. Smirnov, J. Graul, O. Semchinova, D. Uffmann, M. B. Smirnov, A. P. Mirgorodsky, R. A. Evarestov, *Phys. Review B* 58 (1998) 12899.
- [150] J. Bai, M. Dudley, L. Chen, B. J. Skromme, P. J. Hartlieb, E. Michaels, J. W. Kolis, B. Wagner, R. F. Davis, U. Chowdhury, R. D. Dupuis, *Mater. Res. Soc. Sym. Proc.* 831 (2005) E11.37.1.

- [151] S. Miasojedovas, C. Mauder, S. Krotkus, A. Kadys, T. Malinauskas, K. Jarasiunas, M. Heuken, H. Kalisch, A. Vescan, *J. Cryst. Growth* 329 (2011) 33.
- [152] I. Booker, L. Rahimzadeh Khoshroo, J. F. Woitok, V. Kaganer, C. Mauder, H. Behmenburg, J. Gruis, M. Heuken, H. Kalisch, R. H. Jansen, *Phys. Status Solidi (c)* 7 (2010) 1787.
- [153] S. Jursenas, E. Kuokstis, S. Miasojedovas, G. Kurilcik, A. Zukauskas, C. Q. Chen, J. W. Yang, V. Adivarahan, M. A. Khan, *Appl. Phys. Lett.* 85 (2004) 771.
- [154] M. Albrecht, H. P. Strunk, J. L. Weyher, I. Grzegory, S. Porowski, T. Wosinski, *J. Appl. Phys.* 92 (2002) 2000.
- [155] D. Cai, J. Kang, P. Gibart, B. Beaumont, T. Sekiguchi, S. Ito, *Appl. Phys. Lett.* 93 (2008) 081908.
- [156] S. F. Chichibu, A. Uedono, T. Onuma, T. Sota, B. A. Haskell, S. P. DenBaars, J. S. Speck, S. Nakamura, *Appl. Phys. Lett.* 86 (2005) 021914.
- [157] T. Malinauskas, R. Aleksiejunas, K. Jarasiunas, B. Beaumont, P. Gibart, A. Kakanakova-Georgieva, E. Janzen, D. Gogova, B. Monemar, M. Heuken, *J. Cryst. Growth* 300 (2007) 223.
- [158] K. Jarašiūnas, T. Malinauskas, S. Nargelas, V. Gudelis, J. V. Vaitkus, V. Soukhoveev, A. Usikov, *Phys. Status Solidi (b)* 247 (2010) 1703.
- [159] C. Rivera, P. Misra, J. L. Pau, E. Munoz, O. Brandt, H. T. Grahm, K. H. Ploog, *Phys. Status Solidi (c)* 4 (2007) 2548.
- [160] C. Q. Chen, M. E. Gaevski, W. H. Sun, E. Kuokstis, J. P. Zhang, R. S. Q. Fareed, H. M. Wang, J. W. Yang, G. Simin, M. A. Khan, *Appl. Phys. Lett.* 81 (2002) 3194.
- [161] T. Mattila, R. M. Nieminen, *Phys. Review B* 54 (1996) 16676.
- [162] S. C. Cruz, S. Keller, T. E. Mates, U. K. Mishra, S. P. DenBaars, *J. Cryst. Growth* 311 (2009).
- [163] G. B. Stringfellow, *Organometallic Vapor-Phase Epitaxy*, 2 ed., Academic Press, San Diego, 1989.
- [164] S. J. Pearton, H. Cho, J. R. LaRoche, F. Ren, R. G. Wilson, J. W. Lee, *Appl. Phys. Lett.* 75 (1999) 2939.
- [165] J. C. Zolper, R. G. Wilson, S. J. Pearton, R. A. Stall, *Appl. Phys. Lett.* 68 (1996) 1945.
- [166] C. Mauder, B. Reuters, K. R. Wang, D. Fahle, A. Trampert, M. V. Rzheutskii, E. V. Lutsenko, G. P. Yablonskii, J. F. Woitok, M. M. C. Chou, M. Heuken, H. Kalisch, R. H. Jansen, *J. Cryst. Growth* 315 (2011) 246.
- [167] R. Armitage, W. Hong, Q. Yang, H. Feick, J. Gebauer, E. R. Weber, S. Hautakangas, K. Saarinen, *Appl. Phys. Lett.* 82 (2003) 3457.
- [168] G. Popovici, W. Kim, A. Botchkarev, H. Tang, H. Morkoc, J. Solomon, *Appl. Phys. Lett.* 71 (1997) 3385.

- [169] K. Iso, H. Yamada, H. Hirasawa, N. Fellows, M. Saito, K. Fujito, S. P. DenBaars, J. S. Speck, S. Nakamura, *Jpn. J. Appl. Phys.* 46 (2007) 960.
- [170] M. Bosi, R. Fornari, *J. Cryst. Growth* 265 (2004) 434.
- [171] J. E. Northrup, *Appl. Phys. Lett.* 95 (2009) 133107.
- [172] F. Wu, Y.-D. Lin, A. Chakraborty, H. Ohta, S. P. DenBaars, S. Nakamura, J. S. Speck, *Appl. Phys. Lett.* 96 (2010) 231912.
- [173] S. F. Chichibu, T. Sota, K. Wada, S. Nakamura, *J. Vac. Sci. Technol.* 16 (1998) 2204.
- [174] F. Chen, A. N. Cartwright, P. M. Sweeney, M. C. Cheung, *Mater. Res. Soc. Sym. Proc.* 693 (2002) I6.27.
- [175] C. A. Tran, R. F. Karlicek, M. Schurman, A. Osinsky, V. Merai, Y. Li, I. Eliashevich, M. G. Brown, J. Nering, I. Ferguson, R. Stall, *J. Cryst. Growth* 195 (1998) 397.
- [176] G. B. Stringfellow, *J. Cryst. Growth* 312 (2010) 735.
- [177] A. Chakraborty, S. Keller, C. Meier, B. A. Haskell, S. Keller, P. Waltereit, S. P. DenBaars, S. Nakamura, J. S. Speck, U. K. Mishra, *Appl. Phys. Lett.* 86 (2005) 031901.
- [178] T. J. Badcock, P. Dawson, M. J. Kappers, C. McAleese, J. L. Hollander, C. F. Johnston, D. V. Sridhara Rao, A. M. Sanchez, C. J. Humphreys, *Appl. Phys. Lett.* 93 (2008) 101901-1.
- [179] Y. J. Sun, O. Brandt, S. Cronenberg, S. Dhar, H. T. Grahn, K. H. Ploog, *Phys. Review B* 67 (2003) 041306.
- [180] T. Onuma, H. Amaike, M. Kubota, K. Okamoto, H. Ohta, J. Ichihara, H. Takasu, S. F. Chichibu, *Appl. Phys. Lett.* 91 (2007) 181903.
- [181] H. Sato, R. B. Chung, H. Hirasawa, N. Fellows, H. Masui, F. Wu, M. Saito, K. Fujito, J. S. Speck, S. P. DenBaars, S. Nakamura, *Appl. Phys. Lett.* 92 (2008) 221110.
- [182] Y.-D. Lin, A. Chakraborty, S. Brinkley, H. C. Kuo, T. Melo, K. Fujito, J. S. Speck, S. P. DenBaars, S. Nakamura, *Appl. Phys. Lett.* 94 (2009) 261108.
- [183] J. Wu, W. Walukiewicz, *Superlattices and Microstructures* 34 (2003) 63.
- [184] R. Pecharromás-Gallego, R. W. Martin, I. M. Watson, *J. Phys. D: Appl. Phys.* 37 (2004) 2954.
- [185] D. I. Florescu, J. C. Ramer, V. N. Merai, A. Parekh, D. Lu, D. S. Lee, E. A. Armour, *J. Cryst. Growth* 272 (2004) 449.
- [186] A. K. Viswanath, J. I. Lee, D. Kim, C. R. Lee, J. Y. Leem, *Phys. Review B* 58 (1998) 16333.
- [187] K. Kazlauskas, G. Tamulaitis, A. Zukauskas, M. A. Khan, J. W. Yang, J. Zhang, G. Simin, M. S. Shur, R. Gaska, *Appl. Phys. Lett.* 83 (2003) 3722.

- [188] N. F. Gardner, J. C. Kim, J. J. Wierer, Y. C. Shen, M. R. Krames, *Appl. Phys. Lett.* 86 (2005) 111101.
- [189] H. Masui, A. Chakraborty, B. A. Haskell, U. K. Mishra, J. S. Speck, S. Nakamura, S. P. DenBaars, *Jpn. J. Appl. Phys.* 44 (2005) 1329.
- [190] S. Nakagawa, H. Tsujimura, K. Okamoto, M. Kubota, H. Ohta, *Appl. Phys. Lett.* 91 (2007) 171110.
- [191] N. Fellows, H. Sato, H. Masui, S. P. DenBaars, S. Nakamura, *Jpn. J. Appl. Phys.* 47 (2008) 7854.
- [192] H. Tsujimura, S. Nakagawa, K. Okamoto, H. Ohta, *Jpn. J. Appl. Phys.* 46 (2007) 1010.
- [193] M. Kubota, K. Okamoto, T. Tanaka, H. Ohta, *Appl. Phys. Lett.* 92 (2008) 011920.
- [194] H. Masui, H. Yamada, K. Iso, S. Nakamura, S. P. DenBaars, *J. Phys. D: Appl. Phys.* 41 (2008) 225104.
- [195] A. Niwa, O. Tsukuru, T. Kuroda, *Appl. Phys. Lett.* 70 (1997) 2159.
- [196] J. Tauc, R. Grigorovici, A. Vancu, *Phys. Status Solidi (b)* 15 (1966) 627.
- [197] R. Zhang, L. Xie, B. Liu, X. Q. Xiu, D. Y. Fu, Z. Zhang, P. Han, Y. D. Zheng, S. M. Zhou, *Proceedings of SPIE* 7602 (2010) D-1.
- [198] D.-F. Wang, F. Shiwei, C. Lu, A. Motayed, M. Jah, S. N. Mohammad, K. A. Jones, L. Salamanca-Riba, *J. Appl. Phys.* 89 (2001) 6214.
- [199] Y. Dikme, Ph.D dissertation, RWTH Aachen University, (2006).
- [200] B. Liu, R. Zhang, Z. L. Xie, C. X. Liu, J. Y. Kong, J. Yao, Q. J. Liu, Z. Zhang, D. Y. Fu, X. Q. Xiu, H. Lu, P. Chen, P. Han, S. L. Gu, Y. Shi, Y. D. Zheng, *Appl. Phys. Lett.* 91 (2007) 253506.
- [201] B. S. Simpkins, E. T. Yu, P. Waltereit, J. S. Speck, *J. Appl. Phys.* 94 (2003) 1448.
- [202] X. A. Cao, J. A. Teetsov, F. Shahedipour-Sandvik, S. D. Arthur, *J. Cryst. Growth* 264 (2004) 172.
- [203] V. K. Malyutenko, S. S. Bolgov, A. D. Podoltsev, *Appl. Phys. Lett.* 97 (2010) 251110.

Acknowledgements

The making of this thesis was supported by many people. I would like to acknowledge their support in brief by saying thank you to:

Prof. Dr. A. Vescan and Prof. Dr. R. H. Jansen for giving me the opportunity to work and study at RWTH Aachen University in the GaN device technology group and the Chair of electromagnetic theory, respectively.

Prof. Dr. M. Heuken in his role as scientific advisor, for his encouragement and trust, which allowed me to conduct the experiments according to my own ideas.

Prof. Dr. W. Mokwa from the Institute of Materials in Electrical Engineering for his willingness to referee this work.

Dr. H. Kalisch for numerous discussions and his great help with both technology and the correction of scientific manuscripts as well as this thesis.

The lab team of GaN device technology group for so many helping hands and a splendid working atmosphere.

Dr. K. R. Wang and Dr. A. Trampert from the Paul-Drude-Institut in Berlin for TEM investigations and the fruitful collaboration within the collaborated research project.

The group of Prof. Dr. G. P. Yablonskii at the National Science Academy of Belarus in Minsk for their persistent help with optical characterization and its interpretation.

Dr. J. F. Voitok from PANalytical B.V., Almelo, for XRR characterization and support with XRD interpretation.

The group of Prof. Dr. K. Jarašiūnas from the Institute of Materials Science and Applied Research in Vilnius for their optical measurements using free-carrier gratings.

Prof. Dr. Trager-Cowan and G. N. Kumar from Strathclyde University, Glasgow, for their measurements using the ECCI technique.

Dr. R. A. De Souza from the Institute of Physical Chemistry at RWTH Aachen University for SIMS measurements.

Last not least many thanks to my family and friends for their continuous support!

List of publications

- (1) C. Mauder, L. Rahimzadeh Khoshroo, M. V. Rzheutskii, E. V. Lutsenko, G. Yablonskii, V. I. Kozlovsky, J. Woitok, Y. Dikme, M. Heuken, H. Kalisch and R. H. Jansen „*MOVPE growth and investigation of AlInN/AlN multiple quantum wells*”, Phys. Status Solidi (c) **5** (2008) 1553-1555.
- (2) M. Fieger, M. Eickelkamp, W. Zhang, L. Rahimzadeh Khoshroo, C. Mauder, Y. Dikme, M. Heuken, A. Noculak, H. Kalisch, R. H. Jansen, and A. Vescan „*AlInN/GaN HEMTs on sapphire: dc and pulsed characterisation*”, Phys. Status Solidi (c) **5** (2008) 1926-1928.
- (3) L. Rahimzadeh Khoshroo, C. Mauder, W. Zhang, M. Fieger, M. Eickelkamp, Y. Dikme, J. Woitok, P. Niyamakom, A. Vescan, H. Kalisch, M. Heuken, and R. H. Jansen „*Optimisation of AlInN/GaN HEMT structures*”, Phys. Status Solidi (c) **5** (2008) 2041-2043.
- (4) C. Mauder, L. Rahimzadeh Khoshroo, H. Behmenburg, T.C. Wen, Y. Dikme, M. V. Rzheutskii, G.P. Yablonskii, J. Woitok, M.M.C. Chou, M. Heuken, H. Kalisch, R.H. Jansen „*Growth and investigation of m-plane (In)GaN buffer layers on LiAlO₂ substrates*“, J. Cryst. Growth **310** (2008) 4976-4978.
- (5) H. Behmenburg, T. C. Wen, Y. Dikme, C. Mauder, L. Rahimzadeh Khoshroo, M. M. C. Chou, M. V. Rzheutskii, E. V. Lutsenko, G. P. Yablonskii, J. Woitok, H. Kalisch, R. H. Jansen and M. Heuken „*m-plane GaN/InGaN/AlInN on LiAlO₂ grown by MOVPE*“, Phys. Status Solidi (b) **245** (2008) 893-895.
- (6) C. Mauder, L. Rahimzadeh Khoshroo, H. Behmenburg, B. Reuters, M. Bösing, M. V. Rzheutskii, E. V. Lutsenko, G. P. Yablonskii, J. F. Woitok, M. M. C. Chou, M. Heuken, H. Kalisch and R. H. Jansen „*Impact of nitridation on structural and optical properties of MOVPE-grown m-plane GaN layers on LiAlO₂*“, Phys. Status Solidi (c) **6** (2009) S482-S485.
- (7) H. Behmenburg, L. Rahimzadeh Khoshroo, M. Eickelkamp, C. Mauder, M. Fieger, N. Ketteniss, J. Woitok, D. Wamwangi, M. Wuttig, S. Estevez Hernandez, T. Schäpers, M. Heuken, A. Vescan, H. Kalisch, and R. H. Jansen „*Influence of barrier thickness on AlInN/AlN/GaN heterostructures and device properties*”, Phys. Status Solidi (c) **6** (2009) S1041-S1044.

-
- (8) L. Rahimzadeh Khoshroo, C. Mauder, H. Behmenburg, J. Woitok, W. Zander, J. Gruis, B. Reuters, J. Schubert, A. Vescan, M. Heuken, H. Kalisch, and R. H. Jansen „*Epitaxy and characterisation of AlInGaN heterostructures for HEMT application*”, Phys. Status Solidi (c) **6** (2009) S470-S473.
- (9) I. Booker, L. Rahimzadeh Khoshroo, J. F. Woitok, V. Kaganer, C. Mauder, H. Behmenburg, J. Gruis, M. Heuken, H. Kalisch, and R. H. Jansen „*Dislocation assessment via X-ray GaN rocking curve scans*”, Phys. Status Solidi (c) **7** (2010) 1787-1789.
- (10) L. Rahimzadeh Khoshroo, N. Ketteniss, C. Mauder, H. Behmenburg, J. F. Woitok, I. Booker, J. Gruis, M. Heuken, A. Vescan, H. Kalisch and R. H. Jansen „*Quaternary nitride heterostructure field effect transistors*“, Phys. Status Solidi (c) **7** (2010) 2001-2003.
- (11) C. Mauder, K. R. Wang, B. Reuters, H. Behmenburg, L. Rahimzadeh Khoshroo, Q. Wan, A. Trampert, M. V. Rzheutskii, E. V. Lutsenko, G. P. Yablonskii, J. F. Woitok, M. Heuken, H. Kalisch and R. H. Jansen „*Anisotropic properties of MOVPE-grown m-plane GaN layers on LiAlO₂ substrates*“, Phys. Status Solidi (b) **247** (2010) 1750-1752.
- (12) H. Behmenburg, L. Rahimzadeh Khoshroo, C. Mauder, N. Ketteniss, K. H. Lee, M. Eickelkamp, M. Brast, D. Fahle, J. F. Woitok, A. Vescan, H. Kalisch, M. Heuken and R. H. Jansen „*In situ SiN passivation of AlInN/GaN heterostructures by MOVPE*“, Phys. Status Solidi (c) **7** (2010) 2104-2106.
- (13) C. Mauder, B. Reuters, L. Rahimzadeh Khoshroo, M. V. Rzheutskii, E. V. Lutsenko, G. P. Yablonskii, J. F. Woitok, M. Heuken, H. Kalisch, R. H. Jansen „*Development of m-plane GaN anisotropic film properties during MOVPE growth on LiAlO₂ substrates*“, J. Cryst. Growth **312** (2010) 1823-1827.
- (14) K. R. Wang, M. Ramsteiner, C. Mauder, Q. Wan, T. Hentschel, H. T. Grahn, H. Kalisch, M. Heuken, R. H. Jansen, and A. Trampert „*Striated surface morphology and crystal orientation of m-plane GaN films grown on γ -LiAlO₂(100)*“, Appl. Phys. Lett. **96** (2010) 231914.
- (15) D.R. Hang, M. M. C. Chou, C. Mauder, M. Heuken „*MOVPE growth and properties of non-polar InGaN/GaN multiple quantum wells on γ -LiAlO₂ substrates*“, J. Cryst. Growth **312** (2010) 1329-1333.

- (16) C. Mauder, B. Reuters, K. R. Wang, D. Fahle, A. Trampert, M. V. Rzheutskii, E. V. Lutsenko, G. P. Yablonskii, J. F. Woitok, M. M. C. Chou, M. Heuken, H. Kalisch, R. H. Jansen „*Effect of indium incorporation on optical and structural properties of m-plane InGaN/GaN MQW on LiAlO₂ substrates*“, J. Cryst. Growth **315** (2011) 246-249.
- (17) C. Mauder, I. D. Booker, D. Fahle, H. Boukiour, H. Behmenburg, L. Rahimzadeh Khoshroo, J. F. Woitok, A. Vescan, M. Heuken, H. Kalisch, R. H. Jansen „*On the anisotropic wafer curvature of GaN-based heterostructures on Si(1 1 0) substrates grown by MOVPE*“, J. Cryst. Growth **315** (2011) 220-223.
- (18) S. Miasojedovas, C. Mauder, S. Krotkus, A. Kadys, T. Malinauskas, K. Jarašiūnas, M. Heuken, H. Kalisch, A. Vescan „*High-excitation luminescence properties of m-plane GaN grown on LiAlO₂ substrates*“, J. Cryst. Growth **329** (2011) 33-38.
- (19) D. Fahle, H. Behmenburg, C. Mauder, H. Kalisch, R. H. Jansen, H. Kitahata, D. Brien, G. Strauch, D. Schmitz, M. Heuken, and A. Vescan, „*Growth of GaN in a planetary MOCVD hotwall system*“, Phys. Status Solidi (c) **8** (2011) 2041-2043.
- (20) C. Mauder, B. Reuters, H. Behmenburg, R. A. De Souza, J. F. Woitok, M. M. C. Chou, M. Heuken, H. Kalisch and R. H. Jansen „*Mechanisms of impurity incorporation during MOVPE growth of m-plane GaN layers on LiAlO₂*“, Phys. Status Solidi (c) **8** (2011) 2050-2052.
- (21) C. Mauder, E. V. Lutsenko, M. V. Rzheutski, B. Reuters, V. Z. Zubialeovich, V. N. Pavlovskii, G. P. Yablonskii, M. Heuken, H. Kalisch, and A. Vescan „*Irregular spectral position of E || c component of polarized photoluminescence from m-plane InGaN/GaN multiple quantum wells grown on LiAlO₂*“, Appl. Phys. Lett. **99** (2011) 232114.

Curriculum vitae

Personal

Date of birth:	26.06.1981
Place of birth:	Würzburg, Germany
Citizenship:	German

School

09/1987 – 07/1991	Grundschule Schwebenried, Germany
09/1991 – 07/2000	Walther-Rathenau-Gymnasium Schweinfurt, Germany

Military service

10/2000 – 07/2001	Basic military service, Veitshöchheim, Germany
-------------------	--

University

10/2001 – 10/2006	Study of Electrical Engineering at Technical University Ilmenau, Germany Diploma thesis: „Entwicklung eines Stehende-Welle-Interferometers“
11/2006 – 12/2010	Scientific assistant at “Institut für Theoretische Elektrotechnik”, RWTH Aachen University
01/2011 – 12/2011	Scientific assistant at research group “GaN device technology”, RWTH Aachen University